The Meteoritical Society

Meteoritics & Planetary Science 41, Nr 11, 1797–1831 (2006)
Abstract available online at http://meteoritics.org

Petrology of silicate inclusions in the Sombrerete ungrouped iron meteorite: Implications for the origins of IIE-type silicate-bearing irons

Alex RUZICKA[1*], Melinda HUTSON[1], and Christine FLOSS[2]

[1]Cascadia Meteorite Laboratory, Department of Geology, Portland State University,
1721 Southwest Broadway, P.O. Box 751, Portland, Oregon 97207–0751, USA
[2]Washington University, Laboratory for Space Sciences, Campus Box 1105, Saint Louis, Missouri 63130, USA
*Corresponding author. E-mail: ruzickaa@pdx.edu

(Received 26 January 2006; revision accepted 26 July 2006)

Dedicated to the late Martin Prinz

All appendix tables for this article are available online at http://meteoritics.org.

Abstract–The petrography and mineral and bulk chemistries of silicate inclusions in Sombrerete, an ungrouped iron that is one of the most phosphate-rich meteorites known, was studied using optical, scanning electron microscopy (SEM), electron microprobe analysis (EMPA), and secondary ion mass spectrometry (SIMS) techniques. Inclusions contain variable proportions of alkalic siliceous glass (~69 vol% of inclusions on average), aluminous orthopyroxene (~9%, $Wo_{1–4}Fs_{25–35}$, up to ~3 wt% Al), plagioclase (~8%, mainly $An_{70–92}$), Cl-apatite (~7%), chromite (~4%), yagiite (~1%), phosphate-rich segregations (~1%), ilmenite, and merrillite. Ytterbium and Sm anomalies are sometimes present in various phases (positive anomalies for phosphates, negative for glass and orthopyroxene), which possibly reflect phosphate-melt-gas partitioning under transient, reducing conditions at high temperatures. Phosphate-rich segregations and different alkalic glasses (K-rich and Na-rich) formed by two types of liquid immiscibility. Yagiite, a K-Mg silicate previously found in the Colomera (IIE) iron, appears to have formed as a late-stage crystallization product, possibly aided by Na-K liquid unmixing. Trace-element phase compositions reflect fractional crystallization of a single liquid composition that originated by low-degree (~4–8%) equilibrium partial melting of a chondritic precursor. Compositional differences between inclusions appear to have originated as a result of a "filter-press differentiation" process, in which liquidus crystals of Cl-apatite and orthopyroxene were less able than silicate melt to flow through the metallic host between inclusions. This process enabled a phosphoran basaltic andesite precursor liquid to differentiate within the metallic host, yielding a dacite composition for some inclusions. Solidification was relatively rapid, but not so fast as to prevent flow and immiscibility phenomena. Sombrerete originated near a cooling surface in the parent body during rapid, probably impact-induced, mixing of metallic and silicate liquids. We suggest that Sombrerete formed when a planetesimal undergoing endogenic differentiation was collisionally disrupted, possibly in a breakup and reassembly event. Simultaneous endogenic heating and impact processes may have widely affected silicate-bearing irons and other solar system matter.

INTRODUCTION

It is generally accepted that iron meteorites are the products of igneous differentiation in asteroid-sized parent bodies (e.g., Wasson 1985; Hutchison 2004). Some iron meteorites (notably some members of the IAB, IIE, and IVA chemical groups) contain silicate inclusions. These meteorites, together with pallasites, provide evidence for incomplete separation of high- and low-density materials (metal and silicate, respectively). Either differentiation was arrested, or silicates and metal were mixed together following differentiation and not allowed to separate.

Some silicate-bearing irons, including the IIE irons Weekeroo Station, Miles, Colomera, Kodaikanal, and the ungrouped Guin and Sombrerete irons, contain silicate inclusions whose mineral assemblages (often lacking olivine and rich in plagioclase, alkali feldspar, Si-rich glass, pyroxene, phosphate, and ilmenite) imply an evolved stage of

differentiation (e.g., Prinz et al. 1982, 1983; Rubin et al. 1986; Ruzicka et al. 1999; Bogard et al. 2000; Takeda et al. 2003). It is not obvious how such evolved silicate could have formed within meteorites that are products of an incomplete or arrested metal-silicate fractionation.

Sombrerete is one of the most phosphate-rich meteorites known (Prinz et al. 1982, 1983; Garrison et al. 2000). Relatively little work has been performed on the meteorite since the first studies by Prinz et al. (1982, 1983), who suggested that inclusions in Sombrerete could represent "minimum melt" or eutectic compositions, which possibly formed by impact processes. Bogard et al. (2000) obtained a well-defined ^{39}Ar-^{40}Ar plateau age of 4.541 ± 0.001 Ga for Sombrerete and suggested that it formed by partial melting and differentiation within the parent body, followed by mixing of silicate and metal while both were still hot.

In this study, we investigated the petrology of silicate inclusions in Sombrerete using optical petrography, scanning electron microscopy (SEM), electron microprobe analysis (EMPA), and secondary ion mass spectrometry (SIMS) techniques in order to constrain the origin of this meteorite. Our observations also add to the understanding of the mineralogically similar silicate-bearing IIE and Guin irons, even though it is clear based on oxygen-isotope compositions of the silicates and the trace-element compositions of the metal hosts (Mayeda and Clayton 1980; Malvin et al. 1984; Rubin et al. 1986; Wasson and Wang 1986) that separate bodies are required for Sombrerete, Guin, and the IIEs (Bogard et al. 2000).

ANALYTICAL METHODS AND SAMPLES

Samples included two thin sections from the American Museum of Natural History (AMNH 4493-1 and 4493-2), and a 3.6 g piece of Sombrerete obtained from the late Martin Prinz. The latter sample was used to prepare two new thick sections. Altogether, 27 silicate inclusions were studied in the four sections with optical microscopy, SEM, and EMPA, and four were analyzed with SIMS. In addition, a 240 mg sample of the host was cut from the 3.6 g piece and used for instrumental neutron activation analysis (INAA); this sample was visually estimated to be ~99% metal.

SEM work was performed at Portland State University using a JEOL JSM-35C with a Kevex energy dispersive detector and 4pi digital image/spectrum acquisition system. Each inclusion was characterized using digital backscattered electron (BSE) imagery and X-ray maps. X-ray maps were obtained for Na, Mg, Al, Si, P, S, Cl, K, Ca, Ti, Cr, Fe, and Ni, mostly as 320 × 240 pixel maps with 20–25 ms dwell time on each pixel, resulting in a data collection time per mapped area of ~90 min with the optimum deadtime. Modal data were obtained for some inclusions by manual point counting of BSE images, using Photoshop to create mosaics and to overlay grids on the mosaics. Uncertainties for modes (1σ) were determined from the combined theoretical variance for operator and counting error for point counts using the procedure of Solomon (1963). The theoretical variance (σ^2) is given by Best (1982): $\sigma^2 = 44ps^3/RA * [1 + 5.8 * (R/s)^3]$, where p = modal percentage of the mineral, s = the grid spacing, R = mean grain diameter, and A = the area over which the grid extends. BSE images were used to estimate a "representative" grain size which was equated to the mean grain diameter. The modal data were combined with phase compositions determined by the electron microprobe and phase densities based on Gaines et al. (1997) to calculate a bulk inclusion composition using modal reconstruction. For inclusions containing polyphase areas too fine-grained to point count the separate phases within them, an analogous technique was used, except that the polyphase areas were treated as a single entity and defocused microprobe beam analyses (see below) were used to estimate the compositions of these areas. Errors for bulk compositions (1σ) were determined by propagating errors in modes with errors in phase or polyphase area compositions

EMPA analyses were obtained at Oregon State University (OSU) using a Cameca SX-50 electron microprobe equipped with four wavelength-dispersive spectrometers. An accelerating voltage of 15 kV was used for all analyses. Well-characterized mineral and glass standards were used. Various routines, beam sizes, and sample currents were employed depending on the phase being analyzed. Analyses of pyroxene, ilmenite, and some of chromite were obtained with a 50 nA sample current and the beam focused to ~1 μm diameter. Analyses of glass, plagioclase, and some of phosphate were obtained with a 30 nA sample current and the beam focused to 4 μm. Some analyses using specialized routines for chromite (including analysis of V and Zn) or phosphate (including analysis of F) were also made using a ~1 μm beam size and 50 nA sample current. Bulk major-element compositional data using a defocused beam analysis (DBA) technique were obtained by expanding the microprobe beam to 20 or 40 μm diameter. This technique was applied both to fine-grained inclusions and to fine-grained polyphase areas in inclusions, such as glass containing microlites, fine-grained P-rich segregations, and plagioclase glass intergrowths. Uncertainties for bulk compositions using the DBA technique were equated to the standard deviation of the mean for multiple analyses, which can yield high apparent errors when some coarser grains are included in the analyses. Tests were made to evaluate how values for the bulk composition of inclusions using the DBA technique compared with those determined by modal reconstruction (see above). The comparisons indicated substantial agreement between the two techniques, mainly to within the errors estimated for the techniques. This suggests that both techniques give accurate results and that they can be used interchangeably in comparisons of inclusion compositions. Only the results based on modal reconstruction are reported when both techniques were used, as this technique has greater precision.

SIMS analyses for concentrations of the rare earth elements (REE) and other trace elements were determined using the modified Cameca ims 3f ion microprobe at Washington University, according to techniques described by Zinner and Crozaz (1986a). The typical analysis size was ~25 μm in diameter. All analyses were made using an O-primary beam and energy filtering at low mass resolution to remove complex molecular interferences. The resulting mass spectrum is deconvolved in the mass ranges K-Ca-Sc-Ti, Rb-Sr-Y-Zr, and Ba-REE to remove simple molecular interferences that are not eliminated with energy filtering (Alexander 1994; Hsu 1995). Sensitivity factors for the REE in silicates and Ca-phosphate are from Zinner and Crozaz (1986b) and for plagioclase are from Floss and Jolliff (1998). Sensitivity factors for other elements in silicates are from Hsu (1995) and are listed in Table 1 of Floss et al. (1998). Absolute concentrations were determined using sensitivity factors relative to Si for the silicates and Ca for the phosphates; Si and Ca concentrations were determined by electron microprobe analyses of the specific grains chosen for ion probe analysis. SIMS analyses of fine-grained P-rich segregations (using spot diameters somewhat larger than typical) were normalized to average major-element total concentrations determined by the electron microprobe DBA technique (40 μm spots). Reported precision errors for SIMS data are 1σ and are due to counting statistics only.

INAA was used to analyze siderophile elements in the 240 mg metal fragment at the OSU Radiation Center after 1-hour thermal and 6-hour epithermal irradiations, in the same INAA run that was used to analyze Portales Valley samples (Ruzicka et al. 2005). A well-characterized sample of Allende was used as a standard. Analytical uncertainties (±1σ) for various siderophile elements were estimated based on counting rate statistics or the standard deviation of multiple analyses of the standard, whichever yielded the greater error. Uncertainties for Cr, W, Ir, and Au were based on counting statistics, while those for Co, Ga, and As were based on standard analyses. For nickel, both types of uncertainties are reported as repeat analyses of the standard resulted in unexpectedly large errors.

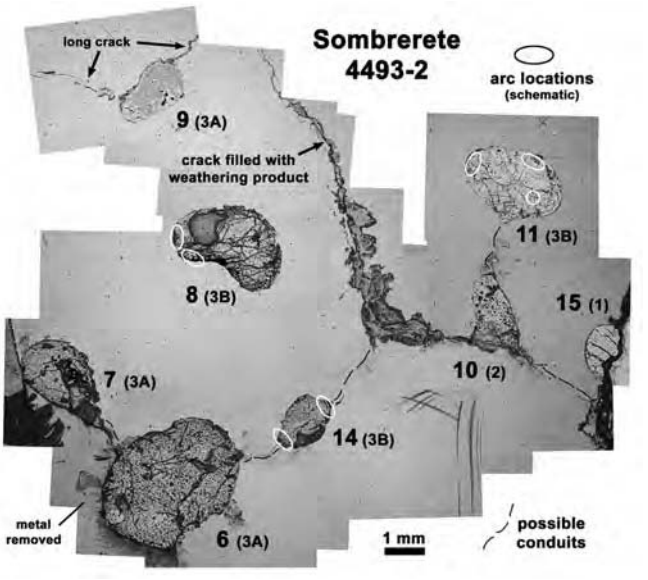

Fig. 1. A mosaic of reflected light images of a portion of Sombrerete 4493-2 showing the distribution and shapes of inclusions (numbers = inclusion designations, types given in parentheses), and the locations of P-rich segregations (arcs, together with an orb in Som-11). The sample has been C-coated and patches of thicker coat are visible in Som-9. Metal was removed from the lower left corner during sample preparation. Continuous or semi-continuous crack-like features connect most inclusions and may have once served as conduits between them.

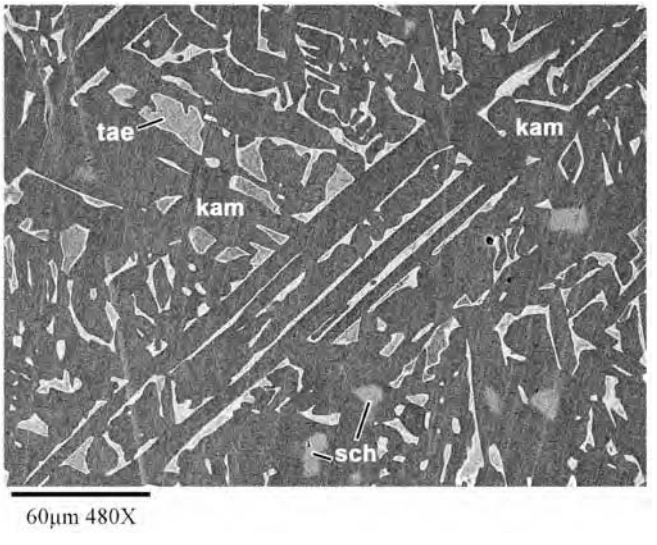

Fig. 2. A backscattered electron image of Sombrerete metal showing typical plessite texture composed of a fine-grained intergrowth of blocky-to-lamellar kamacite (kam, dark) and zoned taenite (tae). Brightness correlates with Ni content. Schreibersite (sch) occurs within kamacite.

RESULTS

Mineralogy, Petrography, Modal Composition

Sombrerete contains ~7.3 vol% rounded or globular silicate inclusions located mainly at grain boundaries of the Fe,Ni metal host (Prinz et al. 1982) (Fig. 1). In cut surfaces, inclusions are ~1–10 mm in diameter (mainly ~2 mm), and have spacings from each other of >2 mm (Fig. 1). Tiny crack-like features, possibly healed metal grain boundaries, extend between inclusions and may have once connected them (Fig. 1). Schreibersite, rare troilite, and swathing kamacite rims ~50–250 μm wide often surround silicate inclusions. Away from inclusions, Sombrerete metal consists of a fine-grained intergrowth of kamacite and taenite (plessite) consisting of blocky, elongate, or lamellar kamacite typically ~5–20 μm (up to ~60 μm) wide and ~45 μm (up to ~600 μm) long, with intervening zoned taenite regions ~5–20 μm across (Fig. 2). The latter have Ni-rich borders only ~0.5–1 μm wide.

In places, elongate or lamellar kamacite has preferred orientations (Fig. 2) reminiscent of a micro-Widmanstätten texture. Small (<20 μm wide) schreibersite grains occur within kamacite (Fig. 2) and appear to have acted as nucleation sites for kamacite. The silicate inclusions are glassy and fine-grained (typical grain diameter is <100 μm), and contain various proportions of phosphate (both Cl-apatite and merrillite), orthopyroxene, plagioclase, chromite, ilmenite, yagiite, rare silica polymorph, and other phases (Table 1). Inclusions can be subdivided into three basic mineralogical-textural types. These include type 1 (glass-rich), type 2 (yagiite-rich), and type 3 (containing microphenocrysts of both orthopyroxene and plagioclase). Type 3 inclusions can be further subdivided into inclusions that lack distinctive fine-grained P-rich segregations (3A) and those that contain these features (3B). Inclusions of different types are located adjacent to one another (Fig. 1). The petrographic features of various inclusion types are described below and illustrated in Figs. 3–5.

Type 1 Inclusions

Five inclusions (Som-4, 13, 15, 17, and 18) have a simple mineralogy dominated by glass, with or without microphenocrysts of Cl-apatite and chromite (Figs. 3a and 3b; Table 1). Type 1 inclusions vary greatly in their abundance of Cl-apatite (~2–17 vol%) and chromite (~0–15%). These inclusions also vary greatly in their extent of mesostasis crystallization (from nil to substantial).

Figures 3a and 3b illustrate the range of textures and mineralogies in type 1 inclusions. Som-17 exemplifies inclusions that contain abundant nondevitrified Na-K-glass (Fig. 3a), whereas Som-13 is typical of other type 1 inclusions that contain abundant microlites (<few μm wide) of feathery orthopyroxene set in glass (Fig. 3b). In type 1 inclusions, Cl-apatite forms euhedral and sometimes skeletal grains of various sizes, being most abundant in Som-17 (Fig. 3a) and least abundant in Som-13 (Fig. 3b). In Som-17, Cl-apatite is present both as larger grains in contact with metal, and as numerous smaller grains which are aligned in a concentric fashion in the inclusion (Fig. 3a). This inclusion also contains a small amount of merrillite intergrown with metal at the inclusion margin, typical of merrillite in Sombrerete.

Type 2 Inclusions

Four inclusions in Sombrerete (Som-2, 10, 21, and 22) are relatively rich in the mineral yagiite (Table 1). Sombrerete provides only the second reported natural occurrence of this mineral, which was previously found in the Colomera (IIE) iron (Bunch and Fuchs 1969; Bogard et al. 2000; Takeda et al. 2003).

Type 2 inclusions are somewhat more complex mineralogically than type 1 inclusions, containing Na-rich glass, yagiite, variable amounts of Cl-apatite, and small amounts of merrillite (at inclusion contacts only), ilmenite, orthopyroxene, and plagioclase. Cl-apatite is present mainly as euhedral microphenocrysts in Som-2 and Som-10, and as numerous elongate microlites ~1–2 μm long in Som-21 and Som-22.

Yagiite in type 2 inclusions forms grains that occur in close proximity to one another, resulting in clusters (Figs. 3c and 3d). The yagiite encloses smaller grains of orthopyroxene and Cl-apatite, but the reverse is never true. Small grains of plagioclase are present in type 2 inclusions, mainly outside of yagiite grain clusters. This plagioclase is present both as fine-grained intergrowths with glass near inclusion rims (spongy plagioclase, see below) and as subhedral grains that surround orthopyroxene grains.

Type 3 Inclusions

Type 3 inclusions are more complex mineralogically and texturally than type 1 and type 2 inclusions. They contain various glasses, orthopyroxene, plagioclase, Cl-apatite, merrillite, ilmenite, chromite, intergrowths of plagioclase and glass that we term "spongy feldspar," small quantities of an SiO_2 polymorph, and a "mixed phase" that appears to be an intergrowth of two or more minerals (Table 1). Nine type 3 inclusions, designated type 3A (Som-6, 7, 9, 12, 16, 19, 20, 23, and 25), contain most of their Cl-apatite in the form of euhedral equant or acicular microphenocrysts. Seven inclusions, designated type 3B (Som-1, 3, 8, 11, 14, 24, and 27), contain most of their phosphate in the form of ~1–2 μm long microlites and in fine-grained P-rich segregations that have arc-shaped or orbicular morphologies.

Textures of type 3A and type 3B inclusions are illustrated in Figs. 4 and 5, respectively. In both types of inclusions, euhedral orthopyroxene grains and subhedral plagioclase grains are typically ~25–100 μm across, with the exception of one inclusion (Som-6) that contains a few coarse orthopyroxene grains up to 700 μm across. Elongate orthopyroxene is often aligned locally within inclusions (Fig. 5a). The spatial abundance of orthopyroxene and plagioclase varies inside inclusions. Both phases are often concentrated near inclusion margins, sometimes forming shells that parallel and occur next to the margins (Fig. 4a). Within inclusions, plagioclase tends to occur in areas that have a higher concentration of larger orthopyroxene grains, always surrounding orthopyroxene and never the reverse (Figs. 5a, 5c, and 5d).

Some plagioclase grains show highly skeletal morphologies with a sieved or porous texture (Fig. 4a). Such "spongy" plagioclase consists of a fine-scale intergrowth of plagioclase and glass. Often spongy feldspar grains (~25–80 μm across) consist of a glass-rich core and a more continuous plagioclase rim. As with other plagioclase, the spongy variant is found between orthopyroxene grains, and is concentrated at inclusion margins, sometimes forming shells ~40–100 μm thick. When immediately adjacent to the host, the plagioclase and glass tend to form parallel stringers

Table 1. Modal compositions of Sombrerete inclusions, determined by point-counting. Data were renormalized to exclude voids created by sample preparation and small amounts of troilite, Fe-Ni metal, and terrestrial weathering products. Numbers in parentheses refer to estimated uncertainties based on sectioning effects (see text). *N* = number of points; *s* = grid spacing; *A* = approximate area mapped (estimated as $A \sim N \cdot s^2$); *R* = "representative" grain size.

Som inclusion	4	17	18	2[a]	10[a]	6	9	16	19	20	1	8[b]	11	14	24	Ave.[c]
Inclusion type	1	1	1	2	2	3A	3A	3A	3A	3A	3B	3B	3B	3B	3B	
Glass (vol%)[d]	77.5 (3.0)	83.8 (3.1)	84.3 (3.4)	68.0 (3.5)	63.1 (4.2)	63.4 (2.8)	51.3 (2.7)	60.4 (2.6)	45.5 (3.2)	55.3 (2.1)	61.4 (2.5)	89.0 (2.1)	60.7 (1.8)	58.0 (2.9)	62.0 (2.7)	67.4
K-glass	0 (–)	0 (–)	0 (–)	0 (–)	0 (–)	0 (–)	2.1 (0.5)	0 (–)	0.4 (0.3)	4.4 (0.6)	2.9 (0.5)	2.2 (0.3)	0 (–)	0 (–)	0 (–)	1.1
Cl-apatite	7.1 (0.9)	16.1 (1.4)	8.6 (1.1)	4.8 (0.9)	10.8 (1.7)	10.4 (1.1)	3.1 (0.7)	5.8 (0.8)	12.0 (1.6)	10.4 (0.9)	1.3 (0.4)	0 (–)	0 (–)	1.0 (0.4)	0.6 (0.3)	7.1
Merrillite	0 (–)	0.1 (0.1)	0 (–)	0.5 (0.3)	0 (–)	0 (–)	0 (–)	0 (–)	0 (–)	0 (–)	0 (–)	0 (–)	0 (–)	0 (–)	0 (–)	<0.1
Yagiite	0 (–)	0 (–)	0 (–)	26.7 (2.2)	26.1 (2.7)	0 (–)	0 (–)	0 (–)	0 (–)	0 (–)	0 (–)	0 (–)	0 (–)	0 (–)	0 (–)	1.2
Orthopyroxene	0 (–)	0 (–)	0 (–)	0 (–)	0 (–)	16.7 (1.4)	15.7 (1.5)	15.0 (1.3)	19.3 (2.1)	16.5 (1.1)	14.5 (1.2)	0.8 (0.2)	12.0 (0.7)	16.3 (1.5)	16.6 (1.4)	9.4
Plagioclase	0 (–)	0 (–)	0 (–)	0 (–)	0 (–)	8.5 (1.0)	5.2 (0.9)	18.3 (1.4)	6.7 (1.2)	12.5 (1.0)	11.5 (1.1)	5.2 (0.5)	8.3 (0.7)	20.5 (1.7)	17.2 (1.4)	7.2
Spongy plag[e]	0 (–)	0 (–)	0 (–)	0 (–)	0 (–)	0 (–)	21.9 (1.7)	0 (–)	14.6 (1.8)	0 (–)	0 (–)	1.2 (0.2)	8.2 (0.7)	0 (–)	0 (–)	1.1
P segregations[f]	0 (–)	0 (–)	0 (–)	0 (–)	0 (–)	0 (–)	0 (–)	0 (–)	0 (–)	0 (–)	8.2 (1.2)	1.2 (0.2)	10.5 (1.1)	4.1 (0.8)	3.4 (0.6)	0.8
Chromite	15.4 (1.4)	0 (–)	7.1 (1.0)	0 (–)	0 (–)	0.5 (0.2)	0 (–)	0 (–)	0 (–)	0.1 (0.1)	0 (–)	0 (–)	0 (–)	0 (–)	0 (–)	4.3
Ilmenite	0 (–)	0 (–)	0 (–)	0 (–)	0 (–)	0.6 (0.3)	0.7 (0.3)	0.6 (0.2)	1.0 (0.5)	0.3 (0.1)	0.3 (0.2)	0.3 (0.1)	0.4 (0.1)	0.1 (0.1)	0.3 (0.2)	0.3
Mixed phase[g]	0 (–)	0 (–)	0 (–)	0 (–)	0 (–)	0 (–)	0 (–)	0 (–)	0.6 (0.4)	0.5 (0.2)	0 (–)	0 (–)	0 (–)	0 (–)	0 (–)	0.1
N	2517	2138	1509	812	1143	1321	1316	1316	1497	2035	8516	3029	3945	1491	1340	
A (mm^2)	16.2	1.77	1.07	1.89	0.94	10.2	1.78	3.22	1.60	10.4	3.14	4.53	3.95	1.48	3.10	
s (μm)	80.1	28.8	26.7	48.2	28.7	87.7	36.8	48.4	32.7	71.4	19.2	38.7	31.7	31.5	48.1	
R (μm)	80	25	20	20	30	50	35	20	35	40	35	15	25	25	25	

[a]"Na-glass" count includes glass-rich mesostasis that contains crystallites of orthopyroxene, ilmenite, and rare plagioclase; "yagiite" count includes yagiite-rich mesostasis that contains crystallites of orthopyroxene.

[b]"Na-glass" and "K-glass" counts include glass-rich mesostases that contain orthopyroxene crystallites and minor phosphate and plagioclase.

[c]Average weighted by count area.

[d]Includes Na-K-glass (Som-4, 17, 18, 6, 14) and Na-glass (other objects).

[e]Plagioclase-glass intergrowths (spongy plagioclase).

[f]P-rich segregations (phosphate-rich arcs and orb).

[g]Mixed phase composed of an intergrowth of at least two phases, possibly Ti-oxide + pyroxene.

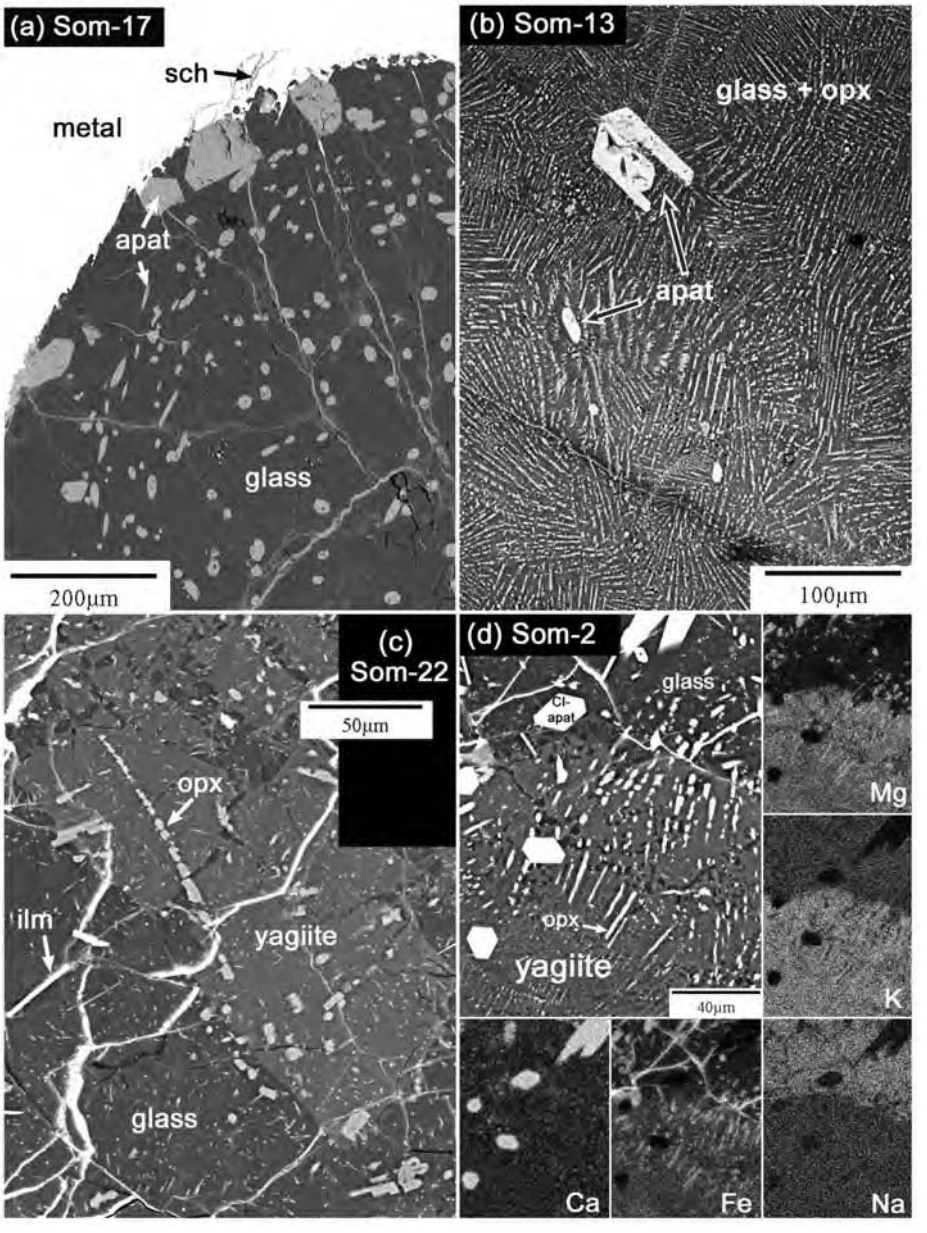

Fig. 3. BSE and X-ray map images of type 1 and type 2 inclusions. Abbreviations: apat = Cl-apatite, ilm = ilmenite, opx = orthopyroxene. Brightness correlates with Ni content. Schreibersite (sch) occurs within kamacite. a) Som-17 contains Cl-apatite microphenocrysts set in glass. Elongate Cl-apatite grains are concentrically arranged in the inclusion. Schreibersite is located adjacent to the silicate inclusion. b) Som-13 contains a few Cl-apatite microphenocrysts set in glassy groundmass rich in orthopyroxene crystallites. The diffuse, dark diagonal line is a crack undergoing charging. c) Som-22 contains yagiite grains set in a glassy groundmass. Cl-apatite microlites occur throughout the glass and yagiite; orthopyroxene and ilmenite needles are present. d) Som-2 contains Cl-apatite microphenocrysts and orthopyroxene crystallites set in Na-rich glass and yagiite. Relative to glass, yagiite is enriched in Mg, K, and Fe, and depleted in Na.

radial to the contact with the host. The largest occurrence of spongy feldspar (in type 3B Som-8) forms a roughly circular object in thin section ~260 μm in diameter that may be spherical in three dimensions.

Type 3 inclusions contain glass of chemically distinct composition. Most inclusions contain Na-rich glass with pockets of K-rich glass; other inclusions contain Na-K-glass (Table 1). K-glass regions (~10–450 μm across) have sharply defined contacts with Na-glass. K-glass is sometimes clearly concentrated around grains of orthopyroxene and plagioclase (Fig. 4b). K-glass also tends to occur at the edges of P-rich segregations and spongy feldspar.

P-Rich Segregations

Type 3B inclusions contain phosphate-rich segregations with lensoid or "arc-like" shapes (Figs. 5a–c). These "arcs" occur near, but not in contact with, the metal host, forming bodies which are elongate parallel to the

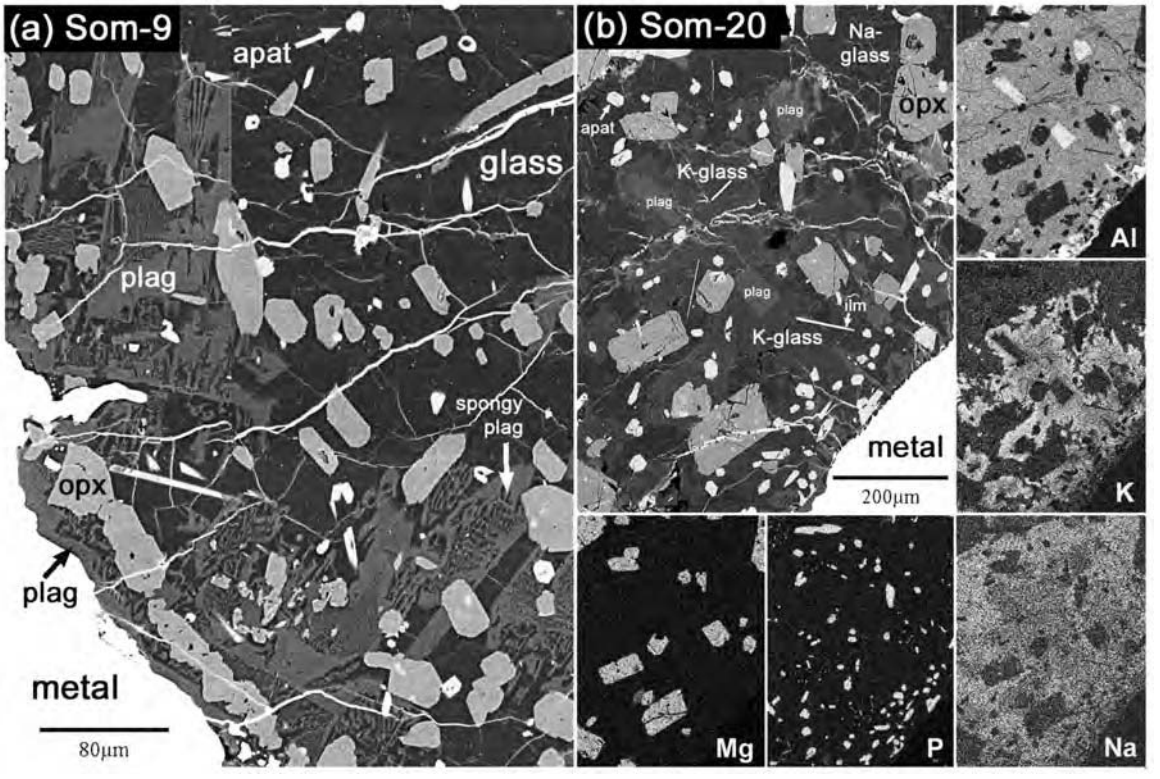

Fig. 4. BSE and X-ray map images of type 3A inclusions. Abbreviations as in Fig. 3; also plag = plagioclase. a) Som-9 has a typical type 3A texture consisting Cl-apatite, orthopyroxene, and plagioclase microphenocrysts enclosed in glass. Plagioclase and orthopyroxene are concentrated near the inclusion-host contact and appear to have preferentially nucleated there. Plagioclase often shows skeletal or "porous" morphologies ("spongy plagioclase"). b) Som-20 contains pockets of K-rich glass (bright in K map) in addition to the more dominant Na-rich glass. This K-glass is found preferentially around plagioclase (brightest grains in Al map) and orthopyroxene grains (Mg map). Plagioclase and Cl-apatite microphenocrysts are concentrated at the inclusion rim. Some acicular ilmenite is present.

inclusion margin. The arcs are ~60–300 μm wide by ~170–1900 μm long, and have aspect ratios (maximum/minimum perpendicular dimensions) of ~2–25. The segregations show sharply defined boundaries which are typically smoothly curving (Figs. 5a–d). Arc boundaries facing towards the metal host always mimic the shape of the inclusion at the arc location. Most of the arc boundaries facing the interior of the inclusion curve subparallel to the inclusion edge, although for one large segregation the margin is locally straight (Fig. 5c), and for another segregation the interior-facing margin is curved in an opposite sense to the inclusion margin. In addition to arcs, there is one small segregation (~80 μm in diameter) located further from the metal host that has a spherical or orbicular form (Fig. 5d). The segregations are polyphase in character, consisting of a fine-grained (less than a few microns) mixture enriched in Cl-apatite and ilmenite, also containing glass, orthopyroxene, and plagioclase (Figs. 5b and 5d). Although Cl-apatite is the main phosphate phase in the segregations, one of the largest arcs contains a merrillite-rich core and an outer zone rich in Cl-apatite (Fig. 5c). Most phases appear to terminate at arc boundaries, except for glass which is continuous across arc boundaries, and except for tiny (~10 μm long, 1 μm wide) acicular ilmenite, which sometimes cross arc boundaries at high angles lying half in and half out of the arcs (Fig. 5c).

Arc boundaries facing towards and away from the adjacent metal host differ in their mineralogical and chemical characteristics. Those facing towards the metal often show a thin (less than a few microns thick) rind of orthopyroxene (Fig. 5b). Such metal-facing arc boundaries appear to have served as a nucleation boundary for orthopyroxene growing into inclusions from the surface of the arc. In contrast, arc margins facing away from the metal lack such rinds, and the arc interiors adjacent to these edges are depleted in Mg and Fe and orthopyroxene (Figs. 5b and 5c). The spherical segregation contains a margin depleted in Mg and Fe (Fig. 5d), as if it corresponds to an arc boundary not adjacent to metal. Ilmenite grains that cross arc boundaries tend to be found at arc boundaries facing away from the metal.

Orthopyroxene grains within inclusions tend to be aligned towards arcs. In inclusions that contain two arcs, two regions of alignment occur which can extend most of the way across the inclusion (Fig. 5a). Within a given inclusion, these alignments can occur in perpendicular (Fig. 5a) or subparallel directions, depending on the locations of arcs. Orthopyroxene

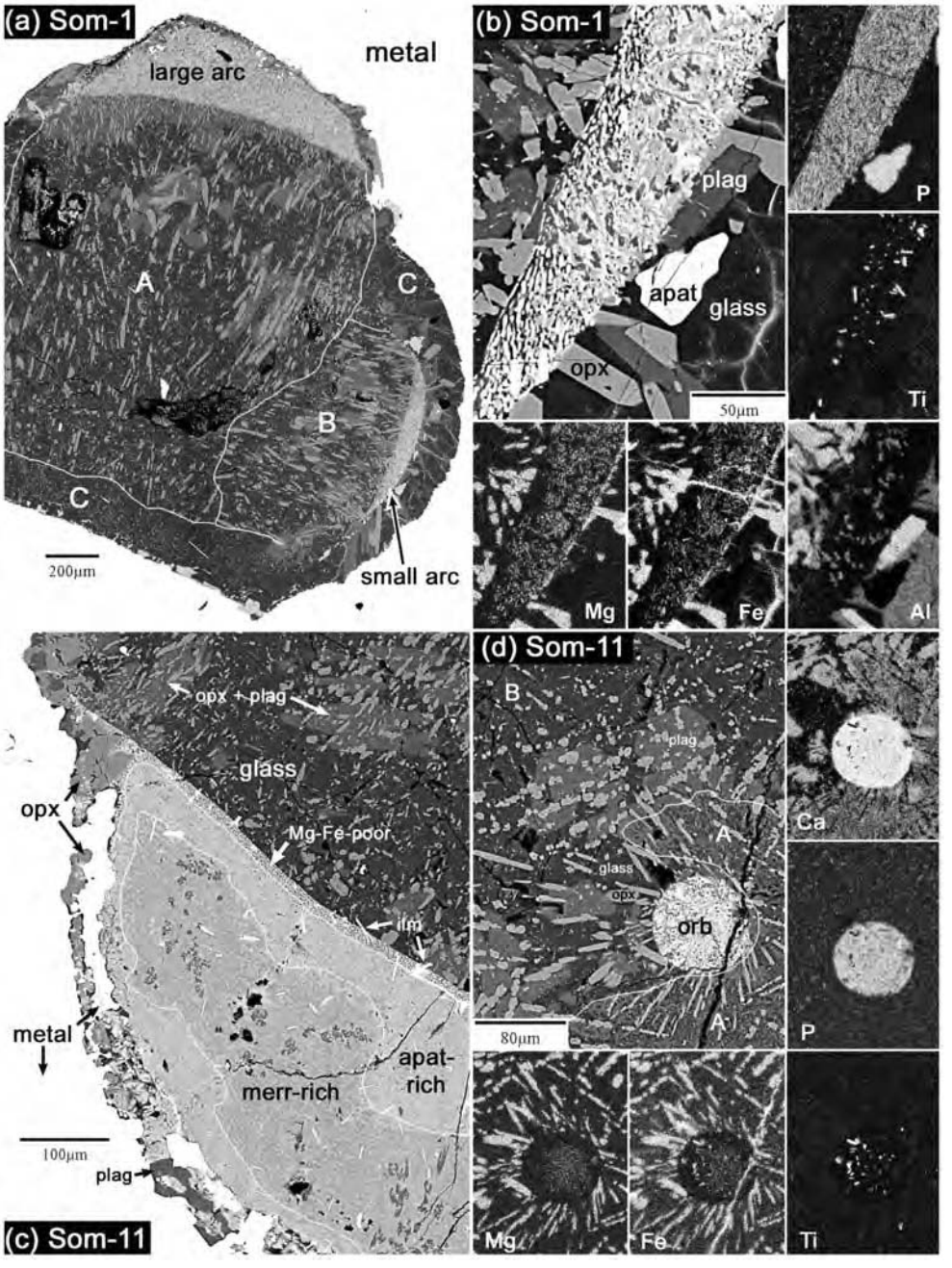

Fig. 5. BSE and X-ray map images of type 3B inclusions. Abbreviations as in Figs. 3 and 4; also merr = merrillite. a) Som-1 contains two phosphate-rich arcs in addition to abundant glass (dark gray) and some orthopyroxene (light gray) and plagioclase (medium gray). Elongate orthopyroxene grains are preferentially aligned towards the large arc in region A and towards the small arc in region B, interpreted as evidence for local flow in these directions. Plagioclase is concentrated around larger and denser accumulations of orthopyroxene grains (best seen in region A). Region C, along the inclusion margin, is crystal-poor. b) A closer view of the small arc in Som-1 showing its polyphase character, rich in Cl-apatite (P map), ilmenite (Ti map), and containing orthopyroxene (Mg and Fe maps), glass (Al map), and plagioclase. A thin layer of orthopyroxene coats and appears to have nucleated on the arc surface facing the metal host (right side, best seen in Mg map). In contrast, Mg and Fe are depleted within the arc on the opposite (left) side of the arc, especially where orthopyroxene grains in the inclusion come into contact with the arc. c) The large arc (light gray) in Som-11 contains a merrillite-rich core and Cl-apatite-rich outer zone. An Mg-Fe-poor border zone occurs on the edge of the arc facing away from the host metal. Ilmenite needles often cross the boundary between arc and the inclusion interior. A gap between the arc and host metal contains larger grains of Cl-apatite, orthopyroxene, plagioclase, and a partial rind of metal. d) A P-rich orb in Som-11 resembles arcs in all respects expect for its spherical form and location (not adjacent to the host metal). The orb occurs near the contact between regions rich in spongy plagioclase (A) and Na-glass (B). Note the arrangement of orthopyroxene crystals around the orb (best seen in the Mg map), suggestive of flow of the orb from left to right.

grains are also preferentially oriented towards the spherical segregation, pointing generally towards the orb but in an asymmetric fashion (Fig. 5d).

Phase Chemistry

Major Elements

Electron microprobe techniques were used to study the phase chemistry of inclusions. Representative phase compositions are given in Table 2.

Orthopyroxene. Low-Ca pyroxene ("orthopyroxene") ($Wo_{2.7\pm0.7}En_{69.0\pm1.5}Fs_{28.4\pm1.3}$) in Sombrerete shows little intragrain zoning of Mg and Fe and only weak zoning in Ca, with rims tending to be slightly depleted in Ca. Orthopyroxene is notably aluminous (0.8–5.8 wt% Al_2O_3, with a mean and standard deviation of 2.4 ± 1.0 wt%) (Table 2a). The compositions of orthopyroxene grains generally overlap in different inclusions, although Som-8 (type 3B) and Som-9 (type 3A) contain atypically ferrous pyroxene ($Fs_{30–35}$).

Plagioclase. Plagioclase compositions overlap between inclusions, and vary considerably in Na and Ca contents ($Ab_{18.1\pm8.1}Or_{0.41\pm0.52}An_{81.5\pm8.3}$) (Table 2a). Often, plagioclase within individual inclusions varies in An-Ab contents by ~15 mol%. Most grains are relatively calcic ($An_{70–96}$), although the few found in Som-18 (type 1) are sodic (~An_{20}). The latter plagioclase (of oligoclase composition) chemically resembles the glass in the inclusion and probably formed by devitrification, whereas the predominant plagioclase (bytownite-anorthite) found elsewhere clearly crystallized from a melt.

Grains located within ~100 µm of inclusion margins tend to be less sodic and more calcic ($An_{80–96}$) than those found elsewhere ($An_{70–96}$). Similarly, individual grains are often zoned radially in Ca-Na, with Ca enrichments towards inclusion margins. For grains located within ~200 µm from the inclusion rims, radial zoning changes of as much as ~15 mol% in An and Ab have been found for analyses in the same grain located ~70 µm apart. This variation in single grains is as large as found in a given inclusion.

Yagiite. The K-Mg silicate known as yagiite was found in six Sombrerete inclusions and constitutes a major phase in four (type 2) inclusions (Table 1). It has the ideal formula $(Na,K)_{1.5}Mg_2(Al,Mg)_3(Si,Al)_{12}O_{30}$ (Bunch and Fuchs 1969; Gaines et al. 1997). Table 2a shows the average composition of yagiite as determined for three type 2 inclusions in Sombrerete. This average composition has a near-ideal stoichiometry, except for being depleted in alkali elements (Table 2a). It is unclear whether this depletion is real, or whether it is an analytical artifact, as such elements might be mobile under the electron microprobe beam. The small amount of P_2O_5 (~0.37 wt%) and Cl (~0.03 wt%) apparent in the average analysis (Table 2a) is probably an artifact, reflecting the difficulty of excluding Cl-apatite microlites from the analyses. Excluding possible contamination effects, abundance variations for all elements except Fe and Mg are ±5% from one analysis to another, whereas for Fe and Mg, abundances vary by up to 40%. This variation is caused in part by core-rim zoning, with rims being slightly ferrous (Fig. 3d).

Other Minerals. Table 2a shows representative compositions of Cl-apatite, merrillite, chromite, and the "mixed phase" in Sombrerete. The composition of the latter phase can be explained as a mixture of Al-pyroxene with either Ti-hematite or ilmenite. Although we suspect that our mixed phase corresponds to the kaersutite of Prinz et al. (1982), it has far too little Ca (~0.02 Ca cations/O) to be consistent with it being kaersutite (~0.08 Ca cations/O). The compositions of the phosphate minerals are relatively uniform and similar in different inclusions. In contrast, chromite grains in the type 1 inclusion Som-4 show strong concentric zoning in Al and Cr, with grain cores enriched in Cr (~30–33 wt% Cr) and depleted in Al (~7–9 wt% Al) compared to rims which have less Cr (~22 wt%), somewhat lower Mg and Ti, and more Al (~15 wt%).

Glasses. Glasses vary significantly in composition, both between and sometimes within inclusions (Table 2b). Glass compositions overall can be described as quartzofeldspathic, with roughly equal proportions of normative plagioclase and quartz, variable (~0–35 mol%) normative orthoclase, and little (mainly <10 mol%) of any other component (Fig. 6). Different glass types include Na-K-rich glass (0.42–1.7 wt% K_2O and 6.1–8.5 wt% Na_2O), Na-rich glass (<0.36 wt% K_2O and 6.3–9.8 wt% Na_2O), K-rich glass (2.4–9.6 wt% K_2O and 1.6–7.8 wt% Na_2O), and an uncommon Si-rich glass that is found near inclusion margins (Table 2b). Na-K-glasses have Na and K contents intermediate to Na-rich and K-rich glasses, but otherwise chemically resemble these glass types (Table 2b). Bulk analyses of plagioclase-glass intergrowths (spongy feldspar) have compositions that can be described as two parts normative quartz and one part normative plagioclase, similar in bulk composition to Si-rich glass (Fig. 6).

Occurrences and compositions of glass types are related to mineral associations and inclusion type. K-glass is found only in some type 3A and 3B inclusions that lack Na-K-glass and which also contain Na-glass. Conversely, Na-K-glass occurs only in some type 1, 3A, and 3B inclusions that also lack Na-glass and K-glass. Finally, only Na-glass of an especially K-poor composition (<0.05 wt% K_2O) is present in type 2 inclusions.

Trace Elements

SIMS techniques were used to analyze various phases in Som-1, 2, 3, and 4, neighboring inclusions from a region

Table 2a. Representative mineral compositions determined by electron microprobe technique. Values in parentheses refer to the standard deviation. n.d. = not determined.

	Opx avg.[a]	Plag avg.[b]	Yagiite avg.[c]	Cl-apatite avg.[d]	Merrillite Som-3[e]	Chromite Som-4 avg.[f]	"Mixed" Som-19[g]
wt%							
SiO_2	51.8 (1.0)	47.2 (2.8)	61.4 (2.3)	n.d.	n.d.	0.06 (0.15)	38.5
TiO_2	0.64 (0.21)	0.05 (0.07)	0.26 (0.09)	n.d.	n.d.	2.68 (0.34)	15.8
Al_2O_3	2.37 (1.05)	32.4 (1.9)	20.3 (1.1)	n.d.	n.d.	19.4 (4.5)	11.9
Cr_2O_3	0.37 (0.17)	0.05 (0.06)	0.05 (0.04)	n.d.	n.d.	42.3 (4.9)	0.37
V_2O_3	n.d.	n.d.	n.d.	n.d.	n.d.	0.33 (0.02)	n.d.
FeO	17.5 (0.8)	0.62 (0.77)	3.70 (0.67)	0.78 (0.22)	n.d.	28.6 (1.42)	17.4
MnO	0.85 (0.13)	0.03 (0.03)	0.24 (0.06)	n.d.	n.d.	0.71 (0.08)	0.61
MgO	23.9 (0.8)	0.08 (0.42)	8.81 (0.54)	0.18 (0.02)	3.33	5.35 (0.74)	9.32
ZnO	n.d.	n.d.	n.d.	n.d.	n.d.	0.03 (0.03)	n.d.
CaO	1.31 (0.33)	17.0 (2.0)	0.66 (0.86)	51.6 (0.44)	47.1	0.03 (0.02)	2.94
Na_2O	0.02 (0.03)	2.09 (0.91)	2.71 (0.41)	0.36 (0.04)	2.39	0.03 (0.03)	2.28
K_2O	0.01 (0.01)	0.07 (0.09)	1.82 (0.37)	n.d.	n.d.	0.02 (0.01)	0.05
P_2O_5	n.d.	0.15 (0.27)	0.37 (0.40)	40.2 (0.5)	45.7	0.02 (0.03)	n.d.
Cl	n.d.	0.03 (0.04)	0.03 (0.03)	6.00 (0.39)	<0.01	<0.01	n.d.
F	n.d.	n.d.	<0.01	<0.01	n.d.	n.d.	n.d.
Total	98.77	99.77	100.35	99.12	98.52	99.56	99.17

[a]Average of 197 analyses of orthopyroxene ($Wo_{2.7\pm0.7}En_{69.0\pm1.5}Fs_{28.4\pm1.3}$) in 13 inclusions. [b]Average of 118 analyses of plagioclase ($Ab_{18.1\pm8.1}Or_{0.41\pm0.52}An_{81.5\pm8.3}$) in 12 inclusions. [c]Average of 22 analyses in three inclusions. Stoichiometry (30 oxygen basis): $(Na_{0.87}K_{0.39})$ $(Mg_{1.34}Fe^{2+}_{0.51}Mn_{0.03}Ca_{0.12})$ $(Al_{2.16}Mg_{0.84})$ $(Si_{10.19}Al_{1.82})$ O_{30}. [d]Average of 14 analyses in Som-1 and Som-2. [e]Average of two analyses in same merrillite grain. [f]Average of 32 analyses. [g]Average of two analyses of same grain, which appears to be an intergrowth of at least two phases. Stoichiometry (6 oxygen basis, all Fe as Fe^{2+}): $(Na_{0.17}Ca_{0.12}Cr_{0.01}Mg_{0.53}$ $Fe^{2+}_{0.56}Mn_{0.02}Ti_{0.45})$ $(Si_{1.47}Al_{0.54})$ O_6 [3.87 cations/6 O]; alternative stoichiometry (6 oxygen basis, all Fe as Fe^{3+}): $(Na_{0.18}Ca_{0.12}Cr_{0.01}Mg_{0.55}Fe^{3+}_{0.58}Mn_{0.02}Ti_{0.46}Al_{0.08})$ $(Si_{1.52}Al_{0.48})$ O_6 [4.00 cations/6 O].

Table 2b. Representative glass compositions determined by electron microprobe technique. Values in parentheses refer to the standard deviation.

	Som-17 Na-K-glass avg.[a]	Som-4 Na-K-glass avg.[b]	Som-1 Na-glass avg.[c]	Som-1 K-glass avg.[d]	Som-20 Na-glass avg.[e]	Som-20 K-glass avg.[f]	Som-2 Na-glass avg.[g]	Som-22 Na-glass (#22.400)	Som-9 Si glass (#9.705)
Incl. type	1	1	3B	3B	3A	3A	2	2	3A
wt%									
SiO_2	70.5 (0.62)	71.4 (1.5)	73.6 (1.9)	70.9 (0.7)	72.5 (1.9)	72.1 (1.4)	71.9 (1.3)	72.4	76.0
TiO_2	0.54 (0.13)	0.66 (0.43)	0.39 (0.23)	0.49 (0.14)	0.40 (0.18)	0.43 (0.17)	0.07 (0.14)	0.32	0.28
Al_2O_3	17.4 (0.29)	16.3 (0.6)	15.5 (0.3)	15.1 (0.3)	16.5 (0.7)	16.3 (0.57)	15.7 (0.2)	15.5	16.6
Cr_2O_3	0.08 (0.06)	0.08 (0.13)	0.04 (0.03)	0.01 (0.02)	0.17 (0.23)	0.09 (0.06)	0.02 (0.04)	0.27	0.16
FeO	0.74 (0.32)	1.11 (0.62)	0.96 (1.01)	0.50 (0.12)	0.66 (0.73)	0.43 (0.17)	0.38 (0.07)	2.43	1.19
MnO	0.03 (0.03)	0.03 (0.03)	0.01 (0.01)	0.04 (0.02)	0.01 (0.02)	0.01 (0.02)	<0.01	0.03	<0.01
MgO	0.28 (0.26)	0.38 (0.26)	0.02 (0.02)	0.11 (0.02)	0.09 (0.12)	0.04 (0.01)	0.12 (0.11)	0.06	<0.01
CaO	2.97 (0.22)	1.85 (0.45)	0.87 (0.05)	0.69 (0.59)	1.24 (0.09)	2.06 (0.14)	1.28 (0.38)	0.29	2.48
Na_2O	7.06 (0.25)	7.04 (0.48)	8.03 (0.28)	2.34 (0.13)	8.27 (0.53)	5.13 (0.56)	8.63 (0.24)	8.89	2.21
K_2O	0.63 (0.09)	0.74 (0.23)	0.26 (0.05)	9.28 (0.34)	0.31 (0.21)	3.86 (0.66)	0.01 (0.01)	0.08	0.23
P_2O_5	0.45 (0.04)	0.33 (0.10)	0.31 (0.07)	0.49 (0.06)	0.19 (0.06)	0.32 (0.12)	0.20 (0.40)	0.17	0.06
Cl	0.03 (0.01)	0.01 (0.01)	0.01 (0.01)	0.05 (0.06)	0.02 (0.02)	0.02 (0.01)	<0.01	0.03	0.02
Total	100.71	99.93	100.00	100.00	100.36	100.79	98.31	100.47	99.23
wt/wt									
K/(Na + K)	0.091	0.105	0.035	0.816	0.040	0.457	0.001	0.010	0.104

[a]Average of 8 analyses. [b]Average of 50 analyses. [c]Average of 13 analyses (coincidentally totals 100 wt%). [d]Average of 12 analyses, totals normalized to 100% before averaging (original totals mainly ~96–97). [e]Average of 7 analyses. [f]Average of 7 analyses. [g]Average of 5 analyses.

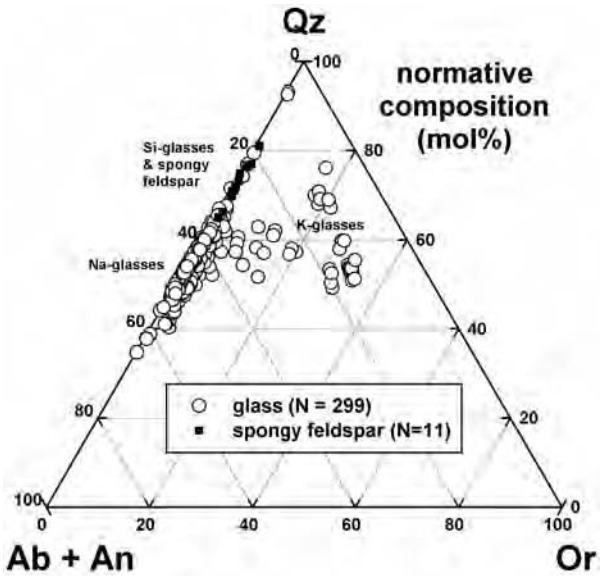

Fig. 6. Normative composition (mol%) of glasses and fine-grained intergrowths of plagioclase and glass (spongy feldspar), in terms of quartz (Qz), orthoclase (Or), albite (Ab), and anorthite (An) components. Glasses consist roughly of a ~50/50 mixture of quartz and plagioclase components with a variable orthoclase component, although more siliceous glass is also present. Spongy feldspar contains more normative quartz than typical glass, similar in bulk composition to Si-rich glass. *N* = number of analyses.

~1.5 cm across. Som-1 is a type 3B inclusion (2.2 × >2.1 mm across) that contains two phosphate arcs (Figs. 5a and 5b); Som-2 is a type 2 inclusion (2.2 × >1.5 mm) (Fig. 3d); Som-3 is a yagiite-bearing type 3B inclusion (1.1 × 1.0 mm) that contains a small phosphate arc and that has two merrillite grains intergrown with the metal host; and Som-4 is an especially large (10.1 × >7.8 mm) type 1 inclusion that contains abundant chromite (Table 1). Complete SIMS data are given in Appendix 1 (all appendix tables are available online at http://meteoritics.org), and CI-normalized abundances are presented in Fig. 7.

Phosphate. Cl-apatite grains are enriched in light rare earth elements (LREE) and show prominent negative Eu anomalies, but the patterns differ in detail between different grains and between inclusions (Figs. 7a and 7b). One of the grains in Som-1 contains a prominent positive Yb anomaly, and both of the grains in this inclusion have a hint of a positive Sm anomaly (Fig. 7b). Merrillite in Som-3 is LREE-enriched with a negative Eu anomaly, and shows a clear positive Yb anomaly (Fig. 7e).

Glasses. Trace-element abundances vary significantly between different analyses of glass within the same inclusion, between different glass types, and between different inclusions (Figs. 7a, 7b, 7e, and 7f). For example, two analyses of Na-K-glass in Som-4 show positive Eu anomalies, while a third analysis shows no Eu anomaly (Fig. 7a). Na and K-glass in Som-1 have abundances that generally resemble Na-K-glass in Som-4, except for containing variable Yb anomalies, strong enrichments in K, Rb, and Ba in K-glass, and strong depletions of these elements in Na-glass (Fig. 7b). Compared to Na-K-glass in Som-4, Na-glass in Som-3 is strongly depleted in REE and in most other elements (except Na, Zr, and Nb), and this glass has prominent negative Sm and Yb anomalies (Fig. 7e). Na-glass in Som-2 is strongly depleted in K, Rb, and Ba compared to Na-K-glass in Som-4 (Fig. 7f).

There is a tendency for CI-normalized abundances in glass to have a complementary relationship to that of other phases in the inclusions. For example, Na-glass in Som-3 has negative Yb anomalies whereas the associated merrillite has a positive Yb anomaly (Fig. 7e), Na-glass in Som-2 is most depleted in those elements (K, Rb, Ba) that are enriched in coexisting yagiite (Fig. 7f), and K-glass in Som-1 has negative Yb anomalies whereas some of the Cl-apatite in Som-1 has a positive anomaly (Fig. 7b). All glasses have low REE/(Zr, Nb, Hf) CI-normalized ratios (Figs. 7a, 7b, 7e, and 7f). This is suggestive of a complementary relationship to phosphate, with high REE/(Zr, Nb, Hf) ratios expected for phosphate on crystal-chemical and experimental grounds.

Plagioclase and Orthopyroxene. Plagioclase shows LREE-enrichments and large positive Eu anomalies (Fig. 7c). The grains vary in Zr, Nb, and LREE abundances that appear to correlate with An content, with the lowest LREE and highest Zr and Nb abundances present in the most calcic plagioclase (Fig. 7c), which is located on the inclusion margin. Orthopyroxene in Som-1 is strongly LREE-depleted (e.g., La/Lu ~0.001 × CI chondrite) (Fig. 7c). Compared to Som-1, orthopyroxene in Som-3 differs in being less strongly LREE-depleted (La/Lu ~ 0.01) and in containing a negative Yb anomaly (Fig. 7e).

Yagiite. Two SIMS analyses were obtained of yagiite in Som-2 and these have similar compositions (Fig. 7f). The composition of yagiite resembles that of Na-glass in the same inclusion for many elements (Ti, Ni, Sr, Zr, Hf, Th, and U), but differs in being strongly enriched in K, Rb, and Ba, enriched in REE, other alkaline earth, and transition elements (Mg, Ca, Sc, V, Mn, Fe), and depleted in Na and Nb (Fig. 7f; Appendix 1).

Phosphate-Rich Segregations. Ten SIMS analyses were obtained in the large and small arcs of Som-1, with each analysis representing a mixture of phases. Although compositions vary from point to point depending on the mixture analyzed, the overall compositions of the arcs are well defined (Fig. 7d). Arcs are strongly enriched in P (~40–60 × CI) and enriched in incompatible elements (e.g., Ti, Y, Nb, REE, Hf, Th, U), with an obvious tendency for the most incompatible elements (LREE, Nb) to be most enriched.

Relative to the bulk inclusion in which they occur, the Som-1 arcs are depleted in those elements that concentrate in Na-glass (Na, Si, and Zr) and enriched in those elements that concentrate in phosphate (P, Ca, REE, Y, Th, U), orthopyroxene (Mg, Sc, V, Cr, Mn, Fe, Ni), and plagioclase (Sr) (Fig. 7d; Appendix 1). Extreme compositions in arc analyses include the metal-facing and orthopyroxene-rich margin of the large arc (1ext4), which has relatively low abundances of incompatibles, and the inclusion-facing and phosphate-rich margin of the small arc (1ext2), which has relatively high abundances of incompatibles (Fig. 7d). The orthopyroxene-rich outer arc area (1ext4) has a possible negative Yb anomaly, whereas the phosphate-rich inner arc area (1ext4) has a prominent positive Sm anomaly and a hint of a positive Yb anomaly (Fig. 7d).

Bulk Compositions

Host Metal

Although silicate inclusions are the focus of this study, INAA was used to analyze the composition of Sombrerete host metal. Table 3 presents the results of our analysis, which is compared to a previous determination for Sombrerete metal. Although the two analyses yield different results for some elements (especially Cr, As, and W), they substantially agree for key elements such as Ir, Ga, Au, and Co. Most notable is the low Ir content of the metal (~0.07 ppm), which is only ~1–2% the value found in H and L chondrites (Chou et al. 1973; Rambaldi 1976, 1977; Kong et al. 1995; Kong and Ebihara 1996). It is unclear why our results for Cr, As, and W differ compared to the previous determination, although we note that the differences for Cr and As are similar to the range found in replicate analyses of oft-analyzed iron meteorites such as Cape York (Cr), Campo del Cielo (Cr), and Gibeon (As) (using data from Koblitz 2003).

Inclusions and Their P-Rich Segregations

The major-element bulk compositions of inclusions and their P-rich segregations were determined by modal reconstruction and defocused beam analysis techniques. The chemical data for individual inclusions (including segregations if present) and segregations alone are given in Appendix 2, and average compositions are summarized in Table 4. Figure 8 shows the compositions of the inclusions in a total alkali-silica diagram with various fields labeled.

The average composition of silicate inclusions in Sombrerete (Table 4) is confirmed to be highly evolved (Prinz et al. 1983), and can be described as a sodic, phosphoran basaltic andesite or Si-poor andesite (Fig. 8). Compared to this composition, the average P-rich segregation in the inclusions is enriched in P, Ca, Cl, Mg, Fe, Mn, and Ti, and depleted in Na, Al, and Si (Table 4). The average Cr content of arcs is less than the average Cr content of inclusions (Table 4), but not if one unusually chromite-rich inclusion (Som-4) is excluded. The segregations are thus P-rich and Si-poor compared to the P-Si-rich melt compositions represented by the inclusions. The compositions of type 1, 2, 3A, and 3B inclusions overlap and vary considerably (Table 4; Fig. 8; Appendix 2).

MODELING AND DISCUSSION

Liquid Immiscibility

Sombrerete shows evidence for multiple types of immiscibility phenomena. These include immiscibility between silicate and metallic melts, which probably formed silicate inclusions in the first place (Prinz et al. 1983), and immiscibility within inclusions to form P-rich segregations, different types of glasses, and possibly spongy feldspar.

The mineralogical, chemical, and textural features of P-rich segregations imply that they formed by liquid immiscibility. A similar interpretation was made for crescent-shaped P-rich objects in Colomera (IIE) inclusions (Fig. 2c of Bogard et al. 2000; Fig. 660 of Buchwald 1975). These segregations contain the same phases as in the remainder of the inclusions, but are greatly enriched in phosphate, consistent with what could occur by immiscibility (e.g., Roedder 1978, 1979). The arcs are enriched in incompatible elements (Table 4; Fig. 7), suggesting that they represent a melt composition. In addition, most elements are enriched in the segregations compared to inclusions, with only Si, Al, Na, K, and Zr depleted in the arcs. This is similar to the pattern seen in experiments and many natural systems in which two liquids unmix, one rich in Fe, P, Ti, Mg, Mn, Ca, REE, and in most other "network-modifier" elements, and the other a more polymerized melt richer in "network-forming" elements such as Si, Al, and alkalis (Watson 1976; Roedder 1978, 1979; Freestone 1978; Visser and Koster Van Groose 1979; Ryerson and Hess 1978). Only Zr clearly defies the pattern expected (Watson 1976; Shearer et al. 2001), being impoverished in the more Fe-rich arc liquid rather than enriched. This is apparently related to the lower content of glass (which concentrates Zr) in arcs compared to the inclusions, and may be evidence of disequilibrium. Further strong support for an immiscible origin of the segregations is provided by their sharply defined, smoothly curving margins (Fig. 5), which probably represent menisci between two liquids. In places, these menisci appear to have served as nucleation sites for orthopyroxene and ilmenite in some areas (Figs. 5b and 5c). In other places, these menisci appear to have remained substantially liquid for a longer time, allowing Fe-Mg exchange to occur between the two liquids and leading to border zones of Mg and Fe depletion within the segregations (Figs. 5b–d).

Petrographic and chemical data suggest that K-glass and Na-glass also formed by the immiscible separation of a melt with an intermediate composition, with the latter preserved in some inclusions as Na-K-glass. The compositions of Na-glass and K-glass are similar to one another and to Na-K-glass for

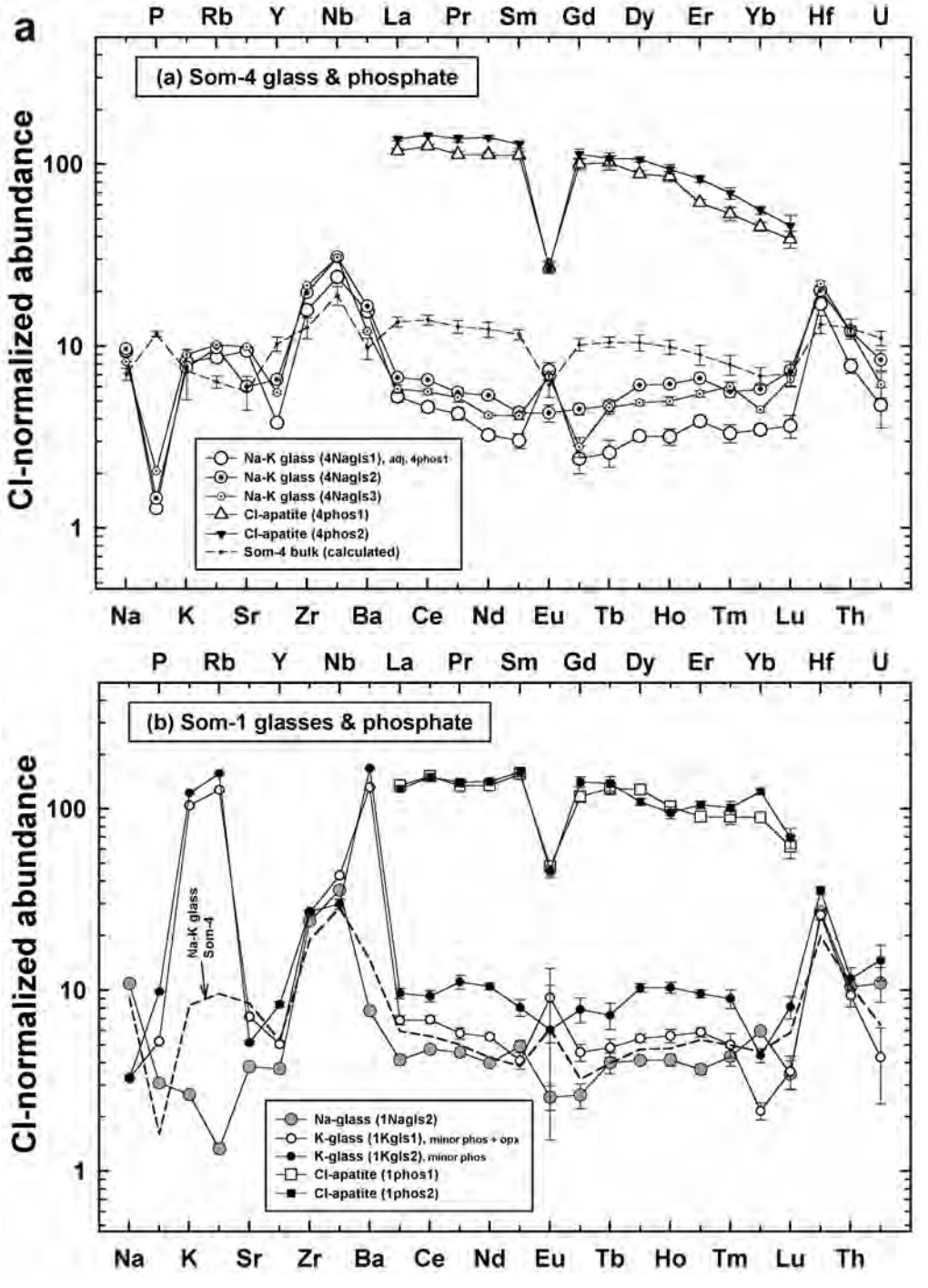

Fig. 7. CI-chondrite-normalized abundances of phases in inclusions. Error bars represent ±1σ uncertainties based on counting statistics. Data are from Appendix 1, and the average CI-chondrite composition of Anders and Grevesse (1989) was used for normalization. a) Glass and Cl-apatite in Som-4, together with an estimate of the bulk composition of the inclusion calculated by modal reconstruction.b) Glasses and Cl-apatite in Som-1.

most elements, with only Na, K, Rb, and Ba having significantly different abundances (Table 2b; Fig. 7), a distinction that is inconsistent with a standard magmatic differentiation process. Na-K-glasses are intermediate in composition to Na-glass and K-glass for Na, K, Rb, and Ba (Fig. 7b), and tie-lines drawn between the K-glasses and Na-glasses pass through the Na-K-glass composition (Figs. 9a and 9b). This suggests either that Na-K-glasses formed by mixing Na melt and K melt, or that the latter two melts separated from Na-K melt. Mixing is unlikely because: 1) it should have produced a complete continuum in glass compositions rather than the discrete compositions observed;

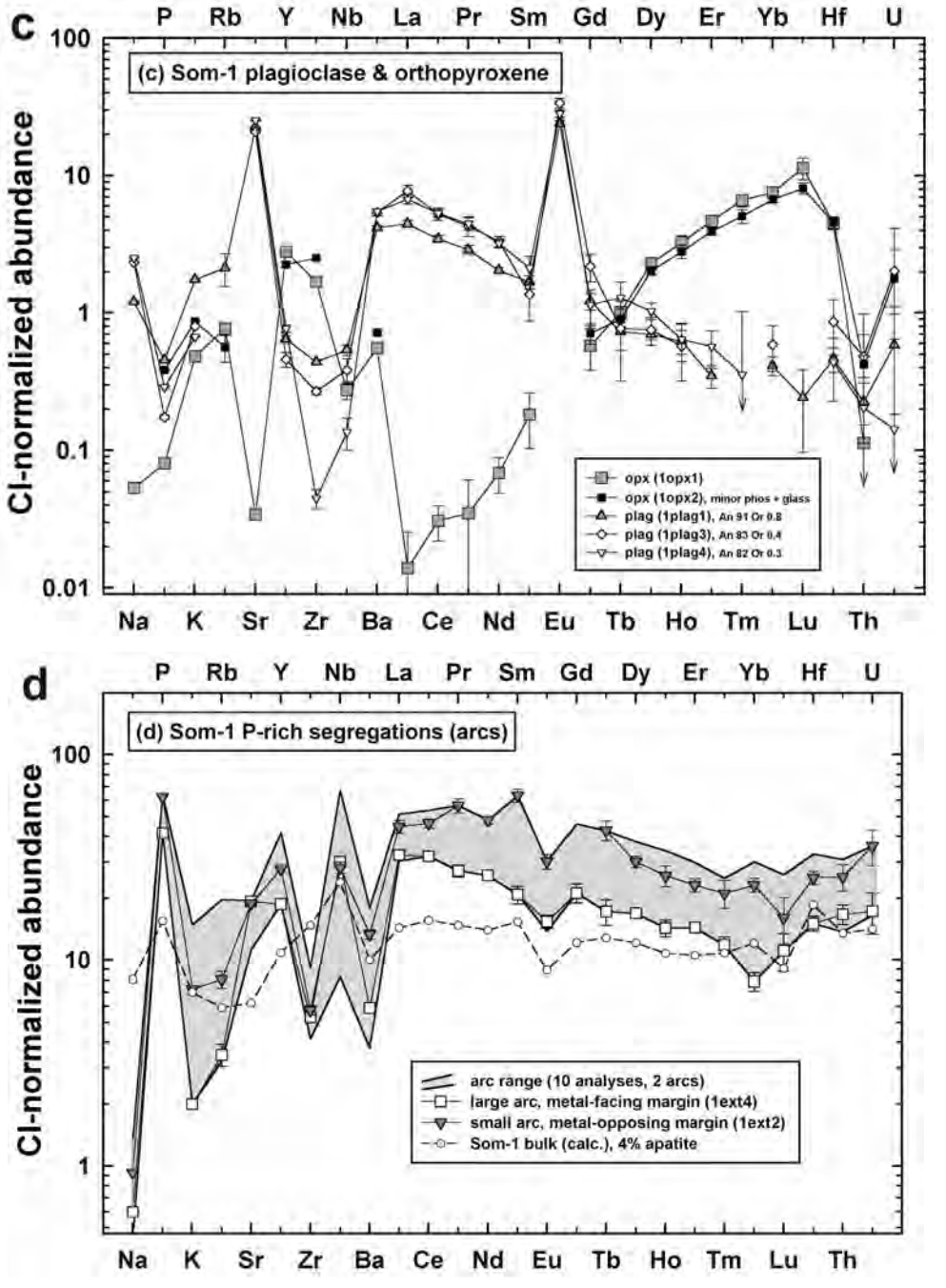

Fig. 7. *Continued*. CI-chondrite-normalized abundances of phases in inclusions. Error bars represent ±1σ uncertainties based on counting statistics. Data are from Appendix 1, and the average CI-chondrite composition of Anders and Grevesse (1989) was used for normalization. c) Orthopyroxene and plagioclase in Som-1. d) Bulk analyses of P-rich segregations in different locations of the large and small arcs in Som-1, together with an estimate of the bulk inclusion composition.

2) it would have had to be totally efficient in some inclusions (those that contain only Na-K-glass) and totally inefficient in others (those that contain only Na-glass and K-glass), an unlikely dichotomy; and 3) it should not have resulted in sharp chemical interfaces between different glass compositions, as observed. Umixing to form Na melt and K melt from Na-K melt can be explained by an immiscibility process in which certain elements prefer to associate based on structural units present in the melts, as suggested by significantly different structures for Na-Si-glass and K-Si-glass (Huang and Cormack 1991), and by the tendency for K-glass to surround preexisting orthopyroxene and plagioclase grains (Fig. 4b), as if melt structure "nucleation" effects were important.

This K-Na melt unmixing model to produce K-rich melt and Na-rich melt is also compatible with the observations of Takeda et al. (2003) for Colomera (IIE), which contains many

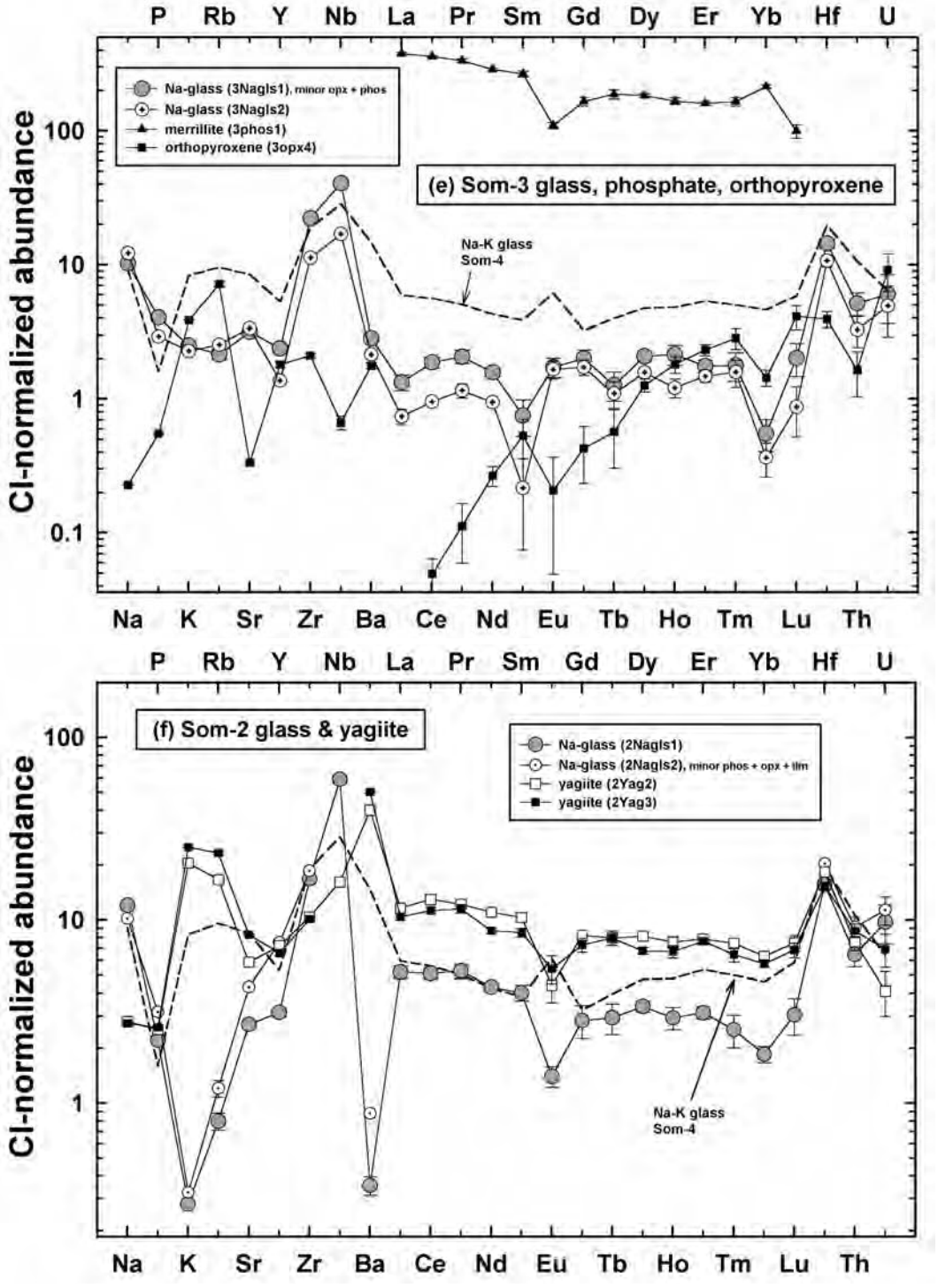

Fig. 7. *Continued.* CI-chondrite-normalized abundances of phases in inclusions. Error bars represent ±1σ uncertainties based on counting statistics. Data are from Appendix 1, and the average CI-chondrite composition of Anders and Grevesse (1989) was used for normalization. e) Glass, merrillite, and orthopyroxene in Som-3. f) Glass and yagiite in Som-2.

small Na-rich inclusions and one large sanidine-rich inclusion. These authors concluded that the two types of material were originally related to one another but that K-rich and Na-rich melts became segregated in some way not involving a standard differentiation process. Our observations suggest that liquid immiscibility could have played a dominate role in the formation of the large sanidine-bearing Colomera inclusion.

In type 2 inclusions, the low K content of Na-glass (see the "Major Elements" section) is almost certainly due to

Table 3. Composition of metal in Sombrerete determined by INAA (this work) compared to values previously obtained by Malvin et al. (1984). Values in parentheses indicate 1σ uncertainties.

	This work	Malvin et al. (1984)
Cr µg/g	10 (3)	40
Co wt%	0.470 (0.024)	0.507
Ni wt%	8.83 (0.06)[a]	10.0
Ga µg/g	16.5 (4.1)	19.1
Ge µg/g	–	11.3
As µg/g	7.8 (0.4)	21.2
W µg/g	0.9 (0.1)	2.04
Ir µg/g	0.069 (0.010)	0.073
Au µg/g	1.8 (0.3)	2.27

[a]±1.0 wt% uncertainty based on multiple counts of Allende standard.

sequestering of K in yagiite, which is a major phase in these inclusions. The Na-glass in this type of inclusion lies along the unmixing trajectory from Na-K-glasses to Na-glasses (Fig. 9b). In addition, yagiite is enriched in K, Rb, and Ba (Fig. 7f), analogous to K-glass (Fig. 7b). This suggests that type 2 inclusions could have experienced the same Na-K unmixing process that affected other inclusions, but instead of resulting in K-glass, yagiite was produced. In other words, a Na-K unmixing process may have contributed to the formation of yagiite. However, yagiite clearly differs from K-glass in containing a higher proportion of ferromagnesian elements (Table 2; Appendix 1), which would have been incorporated in orthopyroxene in other (type 3) inclusions.

Silica-rich glasses and spongy feldspar, which have similar bulk compositions (Fig. 6) and which both preferentially occur near inclusion margins, may also have formed as a result of immiscibility. The textures and composition of spongy feldspar are reminiscent of an association of plagioclase with silica-rich immiscible glass reported for lunar basalt (Rutherford et al. 1974). As with the lunar basalt (Rutherford et al. 1974), rapid crystallization of plagioclase could have depleted melt in those elements not concentrated in plagioclase, producing a localized immiscible melt enriched in normative quartz (Fig. 6). Solidification of such a melt would correspond to Si glass, whereas crystallization would produce spongy feldspar. The intermediate K/Na ratio of Si glass (Table 2b) suggests that both it and spongy feldspar formed before Na-K unmixing occurred.

Rapid Cooling and Crystallization

There is little doubt that Sombrerete inclusions cooled rapidly and that disequilibrium effects were important. Textural evidence for rapid cooling includes the high glass content and fine grain size of all Sombrerete inclusions (Table 1), the skeletal and sieved morphology of spongy feldspar (Fig. 4a), the feathery textures of orthopyroxene in some inclusions (Fig. 3b), and the skeletal or acicular Cl-apatite grains sometimes present (Fig. 3b). The texture of metal in Sombrerete (Fig. 2) also provides evidence for rapid cooling. This texture is similar to "zoneless plessite" that is inferred to have formed by the inversion of martensite (Hutchison and Bevan 1983; Yang and Goldstein 2005). For the ~10 wt% bulk Ni appropriate for Sombrerete metal, such martensite forms upon cooling to below ~500 °C (Yang and Goldstein 2005). It seems likely that cooling was rapid to this temperature, as this would best explain the plessite and fine grain size of kamacite in it, despite the relatively high bulk P content of Sombrerete (~0.27 wt%; Jarosewich 1990) which should have promoted kamacite exsolution (Yang and Goldstein 2005).

Chemical evidence for disequilibrium inside inclusions includes the variable Yb and Sm anomalies found in different analyses of the same phase, such as for apatite and glass in Som-1 (Fig. 7b). Som-3 (Fig. 7e; see "Trace Elements" in the "Phase Chemistry" section) provides an especially good example of disequilibrium. The low abundances of REE and the negative Yb anomalies in the Na-glass and orthopyroxene in Som-3 are consistent with merrillite having previously crystallized from the same melt out of which the other phases formed. However, the presence of a prominent negative Sm anomaly in the glass is difficult to reconcile with the lack of a similar anomaly in orthopyroxene and merrillite. Evidently, the analyzed glass did not form from a melt in complete equilibrium with either the analyzed orthopyroxene or merrillite.

The overlapping bulk compositions of silicate inclusions of different mineralogical and textural types (Table 4; Fig. 8) suggest that the different types did not arise because of differences in bulk composition. Instead, the different mineralogies and textures of inclusions are probably the result of differences in nucleation effects during disequilibrium as a result of rapid cooling. For example, type 1 and 2 inclusions lack larger grains of orthopyroxene and plagioclase. In these inclusions, these phases crystallized either as microlites in the inclusion groundmass, or not at all, because the inclusions cooled too rapidly to allow them to crystallize at their equilibrium temperature. That nucleation was difficult for orthopyroxene and plagioclase is suggested by type 3 inclusions themselves, which contain a concentration of plagioclase and orthopyroxene close to inclusion margins, and a concentration of plagioclase around orthopyroxene (see the "Type 3 Inclusions" section).

Phosphate was an early crystallizing phase in most inclusions and clearly played an important role in affecting phase compositions. Cl-apatite and merrillite microphenocrysts have euhedral textures, suggesting that they were liquidus phases (e.g., Figs. 3a, 3b, and 3d). Trace-element data strongly suggest that glass became depleted in those elements that were sequestered in Cl-apatite and merrillite (REE, Y, Th, and U) (see "Trace Elements" in the "Phase

Table 4. Average bulk composition of various inclusions and fine-grained P-rich segregations (arcs and orb) in Sombrerete. Compositions of inclusions include P-rich segregations where these occur. Values in parentheses refer to the standard deviation; *N* = number of objects averaged. Totals sum to 100% before rounding. Data are from Appendix 2.

	Avg. type 1	Avg. type 2	Avg. type 3A	Avg. type 3B	Avg. all inclusions	Avg. P-rich segregation	Segregation/ inclusion
N	5	4	5	5	19	9	
wt%							
SiO_2	56.6 (6.4)	59.7 (3.6)	57.6 (2.9)	58.5 (3.1)	57.9 (4.4)	21.7 (4.8)	0.37
TiO_2	0.77 (0.21)	0.53 (0.10)	1.01 (0.25)	0.72 (0.11)	0.77 (0.24)	1.14 (0.73)	1.5
Al_2O_3	15.8 (1.2)	15.1 (1.1)	13.5 (1.1)	15.2 (0.8)	14.8 (1.4)	4.61 (1.81)	0.31
Cr_2O_3	3.04 (4.27)	0.06 (0.04)	0.25 (0.10)	0.11 (0.03)	0.91 (2.53)	0.16 (0.05)	0.18
FeO	4.31 (2.69)	5.15 (1.59)	4.83 (0.56)	4.34 (0.80)	4.62 (1.66)	6.06 (1.16)	1.3
MnO	0.13 (0.05)	0.18 (0.03)	0.19 (0.02)	0.21 (0.04)	0.18 (0.05)	0.42 (0.05)	2.3
MgO	1.89 (1.26)	5.03 (0.64)	4.94 (0.45)	4.67 (0.99)	4.08 (1.58)	6.33 (1.84)	1.6
CaO	7.23 (2.80)	5.04 (3.11)	8.21 (1.63)	7.10 (1.15)	7.08 (2.54)	31.5 (4.3)	4.4
Na_2O	5.28 (0.35)	4.51 (0.58)	4.54 (0.46)	5.41 (0.09)	4.96 (0.58)	0.78 (0.37)	0.16
K_2O	0.51 (0.02)	0.69 (0.27)	0.27 (0.11)	0.26 (0.12)	0.42 (0.23)	0.25 (0.16)	0.60
P_2O_5	3.95 (2.32)	3.52 (2.26)	4.02 (1.44)	3.01 (1.01)	3.76 (1.89)	23.7 (3.7)	6.3
Cl	0.52 (0.38)	0.42 (0.26)	0.60 (0.22)	0.40 (0.14)	0.50 (0.28)	3.40 (0.62)	6.8

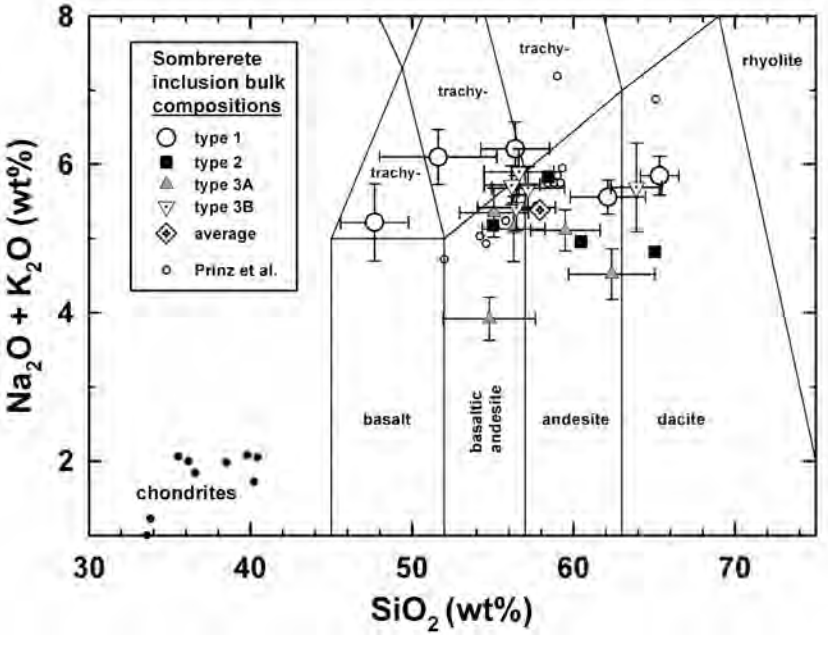

Fig. 8. Total alkali-silica diagram showing that the bulk compositions of inclusions in Sombrerete (data from Appendix 2) range from trachybasalt to dacite, with compositions of alkali-rich basaltic andesite and andesite most common. The data generally agree with the compositions determined by Prinz et al. (1982, 1983; M. Prinz, personal communication). Error bars are ±1σ uncertainties and include estimates for sectioning errors; errors for type 2 inclusions have been omitted for clarity.

Chemistry" section). Similarly, the Ca contents of glasses may be related to phosphate crystallization. Although the Ca contents of glasses are rather low (~0.2–2.4 wt%), there is significant variation between different inclusions (Fig. 9c; Table 2b). Figure 9c shows that glasses with intermediate Na contents (including Na-K-glasses) tend to be the most calcic, whereas glasses that are the most Na-poor (K glasses) and Na-rich tend to be the most depleted in Ca. This pattern can be explained by sequestering of Ca into phosphate, together with the operation of the Na-K unmixing process inferred for Sombrerete residual melts (see the "Liquid Immiscibility" section). Evidently, Na-K-glasses with the highest Ca contents (i.e., in Som-17, Som-18) are the most primitive, as they experienced the least amount of phosphate crystallization and Na-K unmixing (Fig. 9c). However, even the Na-K-glass in Som-4, which has a moderately high Ca content (Fig. 9c), was affected by phosphate crystallization, as evidenced by its relatively low abundances of REE, Y, Th, and U, compared to such elements as Zr, Nb, Ba, and Hf (Fig. 7a).

Orthopyroxene appears to have been a near-liquidus

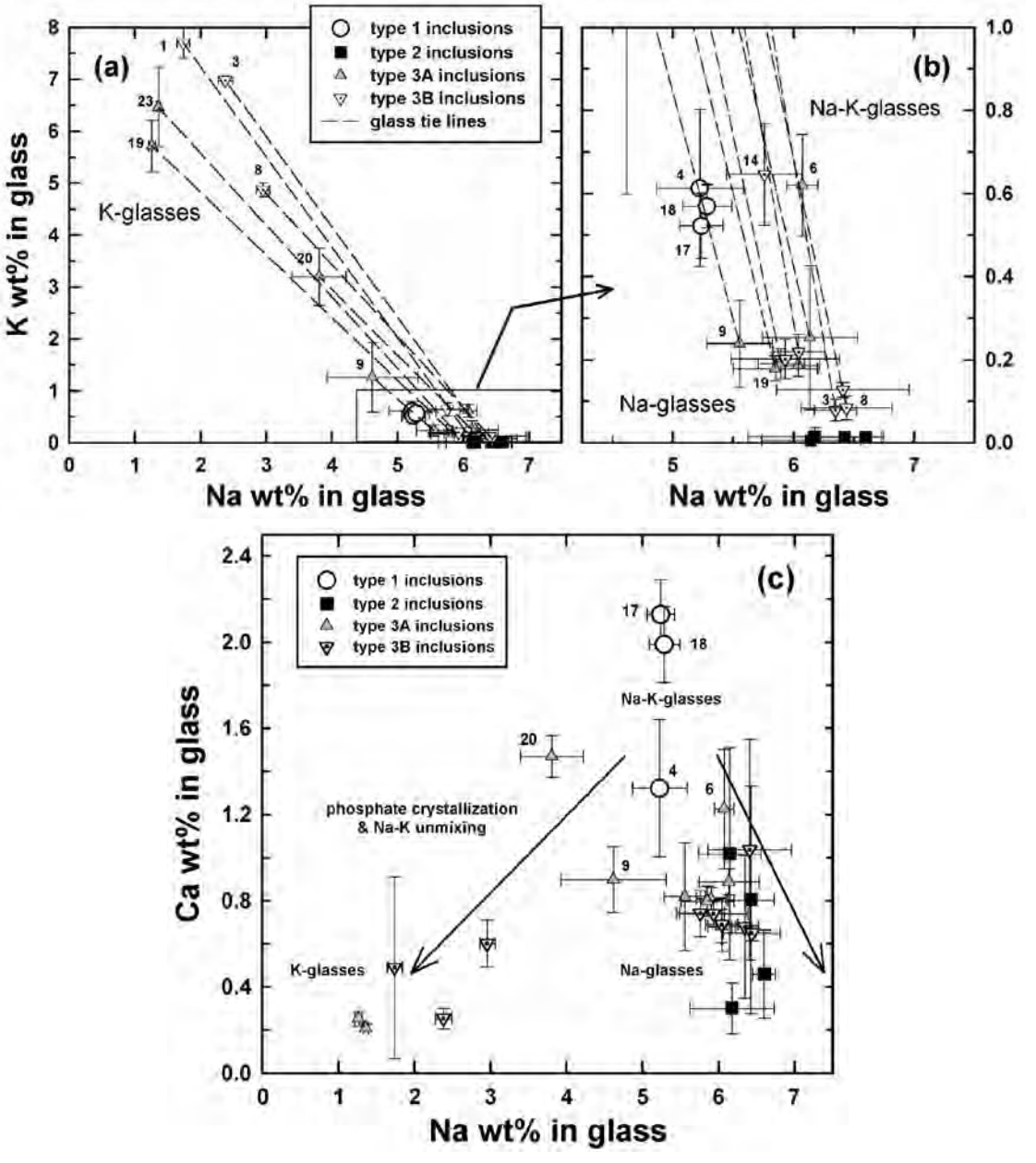

Fig. 9. Diagrams showing Na, K, and Ca contents in glass (averages and ±1σ). Numbers indicate inclusion designations. a, b) Tie lines (dashed) drawn between Na-rich and K-rich glasses in type 3A and 3B inclusions pass through the field of Na-K-glass compositions in other inclusions, consistent with an unmixing process of K and Na from an original Na-K melt. Glasses in type 2 inclusions are especially impoverished in K, probably owing to sequestering of K in yagiite. c) Ca-Na data are consistent with a model in which glass compositions are controlled both by Na-K unmixing and by removal of Ca in phosphate. Na-K-glasses such as those in type 1 inclusions Som-17 and Som-18 are considered to have the most primitive composition.

phase in type 3 inclusions, as suggested by its euhedral to subhedral textures (Figs. 4 and 5b). The generally high Al contents of orthopyroxene (see "Major Elements" in the "Phase Chemistry" section) could be related to a high cooling rate, and probably also reflects the aluminous melt composition from which the pyroxene crystallized. The tendency for plagioclase to be more calcic near inclusion rims and for individual grains to be radially zoned (see "Major Elements" in the "Phase Chemistry" section) can be explained if plagioclase preferentially nucleated close to inclusion margins and grew away from the metal host during fractional crystallization. A similar process appears to have occurred in the Guin silicate-bearing iron (Rubin et al. 1986). Trace-element data for plagioclase show that Ca-Na variations are correlated with the abundances of LREE, Zr, Nb, K, and Rb (Fig. 7c). The most calcic grain (1plag1) has the lowest LREE abundances, consistent with these elements acting as incompatibles. However, this grain also has the

highest abundances of Zr, Nb, K, and Rb, which is inconsistent with the incompatible behavior that might be expected for these elements. Conceivably, Zr and Nb could have behaved as compatible elements if ilmenite was co-crystallizing, whereas K and Rb could have become depleted in residual liquids if they were concentrated in a coexisting immiscible K melt (see the "Liquid Immiscibility" section).

Fluid Flow

Inclusions in Sombrerete show evidence for flow of material while the inclusions and host were partially molten. Inclusions are locally aligned (Fig. 1) and alignment of euhedral crystals within inclusions provides evidence for flow within inclusions after the first-formed crystals were present. For example, the concentric alignment of smaller Cl-apatite grains in inclusions such as Som-17 (Fig. 3a) is ascribed to alignment during fluid flow, as melt swirled in a circular motion within the inclusion. Moreover, the characteristic alignment of orthopyroxene crystals towards arcs, even when grains are not in direct contact with them (e.g., Fig. 5a), could have arisen if the arcs themselves were moving towards the metal host, with orthopyroxene grains following in the wake. Flow regimes associated with arcs were local, as evidenced by different crystal alignment directions within the same inclusion (Fig. 5a). Similarly, the arrangement of orthopyroxene crystals around the P-rich orb is suggestive of movement of the orb from left to right in Fig. 5d. The position of the orb at the edge of a region of spongy feldspar (right side of Fig. 5d) could indicate that the orb was prevented from moving closer to the metal by the presence of preexisting spongy feldspar. The P segregations show no consistent orientations in Sombrerete or within inclusions (Fig. 1), so there is no evidence that flow occurred as a result of buoyancy in a gravitational field. Instead, flow occurred in different directions within Sombrerete.

Filter-Press Differentiation

The inclusions in Sombrerete have widely varying modal abundances (Table 1) and bulk compositions (Fig. 8; Appendix 2), yet their mineral compositions overlap (see "Major Elements" in the "Phase Chemistry" section). A similar situation occurs in other silicate-bearing IIE iron meteorites (Ruzicka et al. 1999), but has not been satisfactorily explained. Here, we provide the results of modeling which suggest that a differentiation process novel to meteorites, which we term "filter-press differentiation," can explain the data for Sombrerete. This process involves crystal-liquid fractionation caused by the metallic host acting as a "filter," preventing already formed crystals over a certain size from moving through the metallic host, but allowing residual melt to be "pressed" into adjacent pockets.

The bulk silica content of inclusions in Sombrerete varies mainly from ~55 to 65 wt% (Fig. 8). The abundances of P_2O_5, CaO, Cl, and (to a lesser extent) MgO and FeO, vary inversely with silica (Fig. 10; Appendix 2). As most of the P, Ca, Cl, Mg, and Fe in the inclusions are contained in Cl-apatite and orthopyroxene, and as Si is concentrated in glass, we examined whether or not the major-element variations for Sombrerete inclusions could result solely or primarily from the removal or addition of phosphate and orthopyroxene from a common precursor.

Model trend lines in Fig. 10 represent the compositions that would be obtained by loss of these phases from a common, Si-poor precursor. The two trend lines show removal of Cl-apatite alone (solid line), or removal of a mixture of 10 parts Cl-apatite and three parts orthopyroxene (dashed line), from a precursor that has a bulk chemical and modal composition similar to that of Som-6, which is the largest (~4 × 3 mm) of the inclusions near the Si-poor terminus of the main chemical trend (Fig. 10). The Si-rich ends of the model trend lines correspond to those compositions that would be obtained if all apatite and/or orthopyroxene were removed from a Som-6-like mineralogy. The model trend lines pass through the overall trend of the data and terminate roughly at the appropriate compositions (Fig. 10). This suggests that the compositions of many inclusions in Sombrerete can be quantitatively explained by apatite and orthopyroxene loss from a single, Si-poor precursor. The most significant discrepancies between the modeled and observed compositions are for the type 1 inclusions Som-4, 17, and 18, although two other type 1 inclusions (Som-13 and 15) fit the model (Fig. 10).

Table 5 compares modeled and observed compositions for selected inclusions. The table shows that excellent matches are typically obtained between modeled and observed compositions for MgO, Al_2O_3, SiO_2, P_2O_5, Cl, CaO, MnO, and FeO. Evidently, variations in the proportions of apatite, orthopyroxene, and glass are largely responsible for variations in the bulk compositions of these inclusions. In Table 5, the poorest matches between the model and observations are obtained for TiO_2 and Cr_2O_3, which in the inclusions tend to decrease as silica content increases, opposite to the modeled trend (Table 5). This implies that Ti- and Cr-rich phases, such as ilmenite and chromite, were lost concurrently with apatite and orthopyroxene.

There are good reasons to believe that the chemical and modal variations described above are indicative of a differentiation sequence, and not merely an artifact of analyzing unrepresentative portions of inclusions. First, the grain size in the inclusions is small (typically <100 μm and often <25 μm across) compared to the size of the inclusions themselves (average ~2.5 mm in diameter), making it highly unlikely that variations in modes and bulk composition are entirely an artifact of unrepresentative sampling. Indeed, the errors indicated for inclusion compositions in Fig. 10 and Table 5 include a realistic estimate for possible sectioning errors, taking into account grain and inclusion sizes and the number of point counts (see the "Analytical Methods and Samples"

section). Second, it would be difficult to explain as a sectioning artifact the presence of apparently correlated variations in the abundances of phosphate, orthopyroxene, and oxide minerals. Third, Cl-apatite and orthopyroxene are liquidus or near-liquidus phases in the inclusions (see the "Rapid Cooling and Crystallization" section), suggesting that these phases would be those most likely to become fractionated during inclusion differentiation, consistent with the model.

Although we discount the possibility that chemical variations are entirely the result of sectioning artifacts, there are provisos. Uncertainties for Na_2O and K_2O are larger in those inclusions that contain K-glass and Na-glass, as only a few larger K-glass patches occur in any given inclusion, and these could have been over- or undersampled. Sectioning effects might also be important for arcs, as they too occur only as a few larger bodies in inclusions. Arcs are enriched in those elements that concentrate in apatite, and calculations show that under- or oversampling of arcs will move apparent inclusion compositions along a trend similar to that for apatite variation alone. However, this effect would be limited to type 3B inclusions only, and there is no tendency for these inclusions to have different compositions than observed for other inclusions, suggesting that any such sampling artifact is small. In addition, arcs contain too little orthopyroxene to account for a significant orthopyroxene-variation trend. Altogether, the provisos discussed here do not invalidate the conclusion that Sombrerete inclusions show real variations in mineral proportions.

Thus, the variable compositions of Sombrerete inclusions are best explained by a model in which a single precursor composition underwent crystal-liquid fractionation to form a variety of inclusion compositions, while the inclusions were enclosed in the metallic host. Most inclusions can be modeled as having formed by the removal from an Si-poor precursor of between 10–80% Cl-apatite alone, or between 10–80% of a 50-50 mixture of Cl-apatite and orthopyroxene. These early-crystallizing phases (see the "Rapid Cooling and Crystallization" section), together with oxide minerals, separated from residual melt, with the residual melt transported elsewhere to form other inclusions. Such transport requires flow of inclusion liquids, consistent with textural data for Sombrerete (see the "Fluid Flow" section). In this way, the bulk compositions of inclusions would differ depending on how flow occurred between them and what proportion of early-formed crystals and residual melt they each trapped.

The metal host itself appears to have acted as a "filter" to allow preferential movement between one inclusion and another of residual melt relative to early formed crystals. Judging from the grain size in Sombrerete, the effective size of the metallic filter may have been ultimately rather small (<100 μm). The apparent requirement that inclusion liquids were able to move from one inclusion to another implies that the liquids were "pressed" through the metallic host by some sort of physical force. To accommodate the movement of inclusion liquids, the metal host itself would probably need to

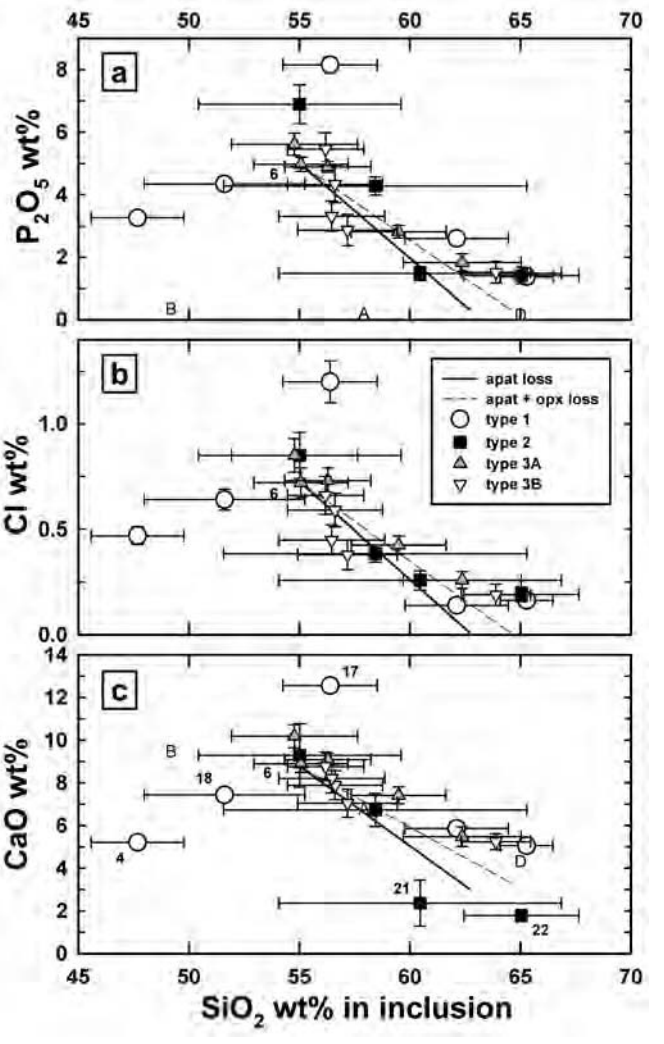

Fig. 10. Variation diagrams suggest that the bulk compositions of most inclusions can be explained by fractionation of Cl-apatite and orthopyroxene from a Si-poor precursor composition similar to that of Som-6. The solid line indicates loss of apatite alone, the dashed line indicates concurrent loss of 10 parts apatite + 3 parts orthopyroxene. Numbers indicate inclusion designations. Letters (B, A, D) indicate average terrestrial basalt, andesite, and dacite compositions, respectively (Best 1982).

be at least partially molten. Transport of inclusion melt may have occurred along what would become metal grain boundaries, with the last passageways between inclusions probably corresponding to the discontinuities in metal observed between inclusions (Fig. 1).

In Sombrerete, the filter-press differentiation mechanism appears to have enabled Si-poor, P-rich liquids (phosphoran basaltic andesite) to differentiate within the host to more siliceous compositions (andesite and even dacite) (Fig. 8). Provided that melt was able to flow between inclusions, such melt would have tended to homogenize the compositions of minerals within them, resulting in similar mineral compositions between inclusions, as observed.

However, different phase compositions could ultimately

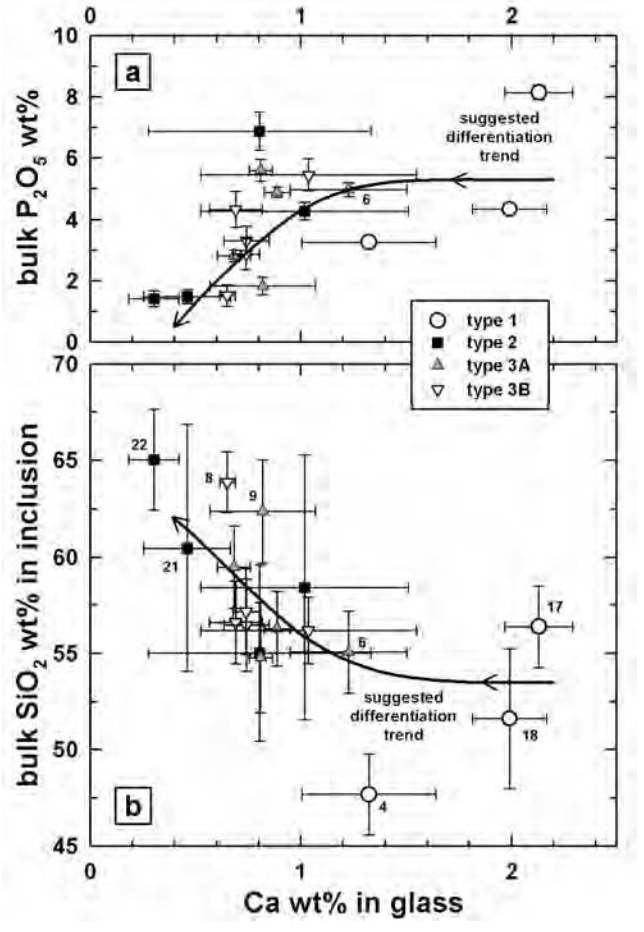

Fig. 11. Average Ca content in glass versus (a) bulk P_2O_5 and (b) bulk silica content in different Sombrerete inclusions. Crude correlations are shown, positive in part (a) and negative in part (b), which are consistent with the filter-press model for the differentiation of Sombrerete inclusions in an open system (see text). In contrast, in situ phosphate crystallization within inclusions acting as closed systems would drive down the Ca content in the residual melt (glass), but would be expected to result in a negative bulk P_2O_5-glass Ca trend, and a positive bulk SiO_2-glass Ca trend, opposite to those shown here.

arise if the inclusions became physically and chemically isolated from one another, if and when the metal "sealed up" the inclusions. That this occurred in Sombrerete is suggested not only by the arrangement of inclusions, which are separated by metal, but also by the different textural types of inclusions, which imply eventual crystallization in an isolated system. Eventual isolation is also implied by the tendency for different inclusions to contain different glass types and glass Ca contents.

Figure 11 shows the relationship between the glass Ca content and bulk P_2O_5 and SiO_2 contents in different inclusions. It was previously suggested that variations in glass Ca content are the result mainly of phosphate crystallization, which would have made Ca behave as a compatible element during crystallization (see the "Rapid Cooling and Crystallization" section). Figure 11 shows that although some scatter occurs, glass Ca content is generally positively correlated with bulk P_2O_5 and negatively correlated with bulk SiO_2. These trends are the expected result of the filter-press differentiation mechanism, because removal of Cl-apatite would tend to drive down bulk P_2O_5 and drive up bulk SiO_2, while also depleting the Ca content in the residual melt now preserved as glass.

It is important to note that although the correlations in glass Ca content and bulk composition are entirely consistent with the filter-press model, they are totally at odds with an alternative model in which the glass composition reflects in situ crystallization of phosphate. For an in situ model in which inclusions were in complete chemical isolation from one another, one would expect that those inclusions containing the most phosphate (highest bulk P_2O_5 and lowest bulk SiO_2) would contain glass with the lowest Ca content, and vice versa. This is clearly opposite to what is observed (Fig. 11). Thus, the relationship between glass composition and bulk composition provides further strong support for the filter-press model.

Although phosphate and orthopyroxene fractionation can explain most of the data for Sombrerete, it has difficulty in explaining the bulk compositions of three inclusions in particular (all type 1), namely Som-4, 17, and 18, which lie off the main chemical trends shown by other inclusions (Fig 10). All three inclusions contain glass of a "primitive" (calcic) composition (Figs. 9c and 11), presumably indicative of little apatite fractionation. Moreover, all three are MgO-poor, as if they lost a Mg-rich phase (Fig. 10c). A clue to the origin of these inclusions is that two of them (Som-18 and especially Som-4) contain elevated quantities of chromite (Table 1). We note that the addition of chromite to a Som-6-like precursor composition can explain the composition of Som-18 and Som-4, and that removal of such chromite can generally explain the composition of Som-17, although for all three inclusions it appears that removal of an additional Mg-rich phase besides chromite is needed. We suggest that chromite and other Mg-rich phases may have fractionated in these inclusions relatively early.

Model Parental Liquid

As discussed in the previous section, it appears that the varied compositions of most inclusions in Sombrerete could have been derived from a single parental liquid by differentiation occurring within the confines of the metal host. Here we estimate the composition of this liquid using two independent approaches: 1) determining melt compositions corresponding to early-crystallizing phosphate, and 2) equating the bulk compositions of inclusions to melt compositions and inferring how these might differ from the parent composition.

With the first approach, the measured trace-element compositions for phosphates (Appendix 1) are combined with representative equilibrium mineral/melt partition coefficients

(*D* values; Appendix 3) to calculate the parental melt compositions for these phosphates, and thereby of the inclusions themselves. This procedure is simple, but it has some uncertainties. Clearly, equilibrium was not fully maintained within inclusions (see the "Rapid Cooling and Crystallization" section), so equilibrium *D* values may not be appropriate. Moreover, the equilibrium *D* values themselves depend on a variety of factors such as composition and fO_2, and this introduces uncertainty. That said, the average REE abundances of parental melts for Cl-apatite are shown in Fig. 12 (unshaded squares). These indicate HREE abundances of ~15–20 × CI chondrites, with progressive enrichment of LREE to as much as ~30 × CI for La (Fig. 12).

The second approach is based on the assumption that the bulk compositions of the inclusions themselves represent liquid compositions, which were derived from the parental liquid. Sufficient data were obtained for Som-1 (type 3B) and Som-4 (type 1) to estimate the bulk trace-element compositions of these inclusions, by combining EMP and SIMS data for phase compositions with modal data (Table 6). In the calculations, the CI-normalized abundances of Y, Th, and U in phosphate (which were not measured) were equated to that measured for Ho, Er, and Ho in phosphate, respectively, based on the measured compositions of arcs (Fig. 7d). This makes the reasonable assumption that phosphate controls the abundances of these elements in arcs.

The bulk composition for Som-4 can be calculated in a straightforward way. It has an LREE-enriched pattern (up to ~15 × CI chondrites), and enrichments in Nb, Hf, Th, and U compared to the REE (Figs. 7a, 12). Unfortunately, it is not immediately obvious how to relate the composition for Som-4 to a model original precursor liquid for other Sombrerete inclusions, because Som-4 does not form part of the main chemical trend shown by most inclusions (see the "Filter-Press Differentiation" section).

In contrast, the major-element composition of Som-1 does fall on the main chemical trend for Sombrerete inclusions (see the "Filter-Press Differentiation" section), but an extra step is needed to use trace-element data to calculate the correct bulk composition of this inclusion. This inclusion has most of its phosphate present as microlites which are too small to point-count, so Fig. 12 shows the effect of adding different amounts of phosphate to the apparent (microlite-free) composition obtained using SIMS data. An estimate of the true composition can be obtained by adding a sufficient amount of Cl-apatite to the microlite-free (SIMS) composition to equal the total amount of P and Cl determined for the inclusion based on independent EMPA methods (downward triangle in Fig. 12). This takes into account the presence of microlites in glass by treating the composition of glass as the composition obtained by defocused beam analyses, in which both glass and microlites were analyzed together. (The same procedure was used to calculate major-element compositions for all type 3B inclusions). The P and Ca SIMS and EMPA data for Som-1 agree exactly if ~4 wt% total apatite is assumed (excluding the phosphate in arcs, which is already taken into account) (Fig. 12). This suggests that the corrected composition for Som-1 corresponds to 4 wt% (non-arc) apatite (Fig. 12; Table 6).

The bulk compositions for Som-4 and Som-1 (4% apatite) are broadly similar for many elements (Fig. 12; Table 6), but differ in the abundances of elements concentrated in chromite (V, Cr, and Fe; enriched in Som-4) and orthopyroxene (Mg and Sc; enriched in Som-1); Som-1 also contains slightly more REE and a positive Yb anomaly (Fig. 12). Nonetheless, the similarity in composition for so many elements in these two inclusions suggests that they are generally representative of a common liquid composition.

The Som-1 and Som-4 inclusion compositions are somewhat REE-depleted compared to the parental melt compositions calculated for the Cl-apatite within them (Fig. 12). However, this discrepancy can be readily understood if both the Som-1 and Som-4 liquids experienced Cl-apatite removal from the original parental melt, as a result of filter-press differentiation (see the "Filter-Press Differentiation" section). Thus, we infer that the parental melt was enriched in normative apatite compared to both the Som-4 and Som-1 (4% apatite) compositions. As noted above, the composition of Som-1 is more closely related to the compositions of other inclusions. By adding normative Cl-apatite to the bulk composition of Som-1, REE abundances similar to those inferred for the parental melts of Cl-apatite are obtained (Fig. 12). Moreover, the abundances of the most incompatible elements (LREE, Nb) become similar with a Som-1-like composition with 10 wt% apatite (Fig. 12; Table 6), as would be expected for an unfractionated precursor.

Thus, we suggest that the precursor liquid for Sombrerete inclusions was probably close to the composition obtained by adjusting Som-1 to 10% apatite (Fig. 12; Table 6). This provides a good match to the parental melts inferred for Cl-apatite, and provides LREE/Nb abundance ratios of ~1 as would be expected for partial melts of a chondritic source. Based on the high observed modal abundances of Cl-apatite found in inclusions (Table 1), a precursor liquid with ~10% normative apatite is reasonable. Moreover, this value is bracketed on the low end by the corrected bulk composition for Som-1 (~4% apatite), which almost certainly experienced some phosphate loss from the precursor, and on the upper end by the high normative phosphate content required to explain the compositions of arcs (~20% apatite), which almost certainly represent a phosphate-enriched composition (see the "Liquid Immiscibility" section).

Partial Melting Models

The model parental melt for Sombrerete (Table 6; Fig. 12) has the overall chemical attributes of what one would expect for

Table 5. Example comparisons between model (italicized and bolded notation) and observed Sombrerete inclusion compositions, assuming variable fractionation of Cl-apatite and orthopyroxene from a single precursor composition (Som-6 analogue).[a] Inclusion compositions are from Appendix 2A; values in parentheses refer to ±1σ uncertainties. Totals sum to 100% before rounding.

wt%	Na_2O	MgO	Al_2O_3	SiO_2	P_2O_5	Cl	K_2O	CaO	TiO_2	Cr_2O_3	MnO	FeO
Model precursor	***4.94***	***5.19***	***13.6***	***55.1***	***4.97***	***0.72***	***0.43***	***8.75***	***1.01***	***0.35***	***0.22***	***4.77***
	(0.24)	(0.45)	(0.68)	(2.1)	(0.23)	(0.07)	(0.09)	(0.40)	(0.07)	(0.10)	(0.03)	(0.47)
15% apatite loss	***5.06***	***5.19***	***13.9***	***56.2***	***4.27***	***0.61***	***0.45***	***7.89***	***1.03***	***0.35***	***0.22***	***4.78***
Som-1	5.43	5.10	14.0	56.6	4.33	0.59	0.47	7.89	0.82	0.07	0.24	4.44
	(0.24)	(0.41)	(0.7)	(2.2)	(0.59)	(0.08)	(0.07)	(0.68)	(0.10)	(0.02)	(0.02)	(0.44)
50% apatite loss	***5.34***	***5.20***	***14.7***	***58.9***	***2.65***	***0.37***	***0.47***	***5.88***	***1.08***	***0.37***	***0.22***	***4.81***
Som-24	5.49	5.22	15.2	57.2	2.87	0.38	0.19	7.05	0.78	0.10	0.23	5.35
	(0.26)	(0.45)	(0.7)	(2.3)	(0.50)	(0.07)	(0.03)	(0.66)	(0.11)	(0.07)	(0.02)	(0.50)
70% apatite loss	***5.50***	***5.21***	***15.2***	***60.4***	***1.72***	***0.22***	***0.49***	***4.74***	***1.11***	***0.38***	***0.22***	***4.83***
Som-9	4.28	4.51	14.1	62.4	1.83	0.26	0.24	5.48	1.14	0.21	0.20	5.39
	(0.27)	(0.53)	(0.74)	(2.7)	(0.28)	(0.04)	(0.07)	(0.46)	(0.16)	(0.03)	(0.03)	(0.76)
80% apatite loss	***5.58***	***5.21***	***15.4***	***61.2***	***1.25***	***0.15***	***0.49***	***4.17***	***1.13***	***0.39***	***0.22***	***4.84***
Som-22	3.93	5.75	15.7	65.0	1.42	0.19	0.89	1.78	0.41	0.03	0.19	4.63
	(1.61)	(2.09)	(0.9)	(2.6)	(0.26)	(0.03)	(0.33)	(0.28)	(0.29)	(0.02)	(0.06)	(1.84)
80% apatite loss + 56% orthopyroxene loss	***6.38***	***2.56***	***17.3***	***62.6***	***1.26***	***0.15***	***0.56***	***4.42***	***1.20***	***0.39***	***0.12***	***3.04***
Som-8	5.47	2.97	16.3	63.9	1.52	0.19	0.22	5.24	0.76	0.16	0.14	3.11
	(0.56)	(0.13)	(0.4)	(1.6)	(0.35)	(0.05)	(0.04)	(0.37)	(0.03)	(0.01)	(0.01)	(0.18)
Som-15	5.33	2.23	16.2	65.3	1.38	0.16	0.51	5.06	0.84	0.11	0.15	2.71
	(0.18)	(0.81)	(0.5)	(1.2)	(0.14)	(0.03)	(0.08)	(0.19)	(0.38)	(0.03)	(0.05)	(0.79)

[a]Models assume that Cl-apatite and orthopyroxene have compositions identical to the average composition measured in Sombrerete, and that the precursor contains 11.7 wt% Cl-apatite and 20.1 wt% orthopyroxene, the same as for Som-6.

a partial melt of a chondritic precursor, including enrichments in incompatible lithophile elements and depletions in compatible elements such as Mg, V, Cr, Fe, and Ni. A low degree of partial melting can explain the high abundances of incompatible elements (~20 × CI for Nb and LREE), and is consistent with the negative Eu anomaly and relatively low abundance of Sr (~6 × CI) (Fig. 12), as they imply retainment of some Eu and Sr in plagioclase in the source region.

Using a best estimate of equilibrium *D* values for some well-constrained elements (Appendix 3), Fig. 13 shows that the composition of the inferred parental melt can be successfully reproduced by a simple model assuming equilibrium ("batch") melting of a chondritic protolith. This chondritic protolith is assumed to have CR-chondrite-like abundances of all elements except the REE and Y, and H-chondrite-like abundances of the REE and Y. The former assumption was made as the O-isotopic composition of Sombrerete (Mayeda and Clayton 1980) somewhat resembles that of CR chondrites (Lodders and Fegley 1988), whereas the latter assumption was made because the REE abundances in H chondrites are similar to that in CR chondrites but apparently more precisely determined, as implied by more uniform CI abundances. Figure 13 plots the compositions of melts that would be expected for melt fractions of 1, 4, 8, and 15 wt%, assuming a plausible residue composition dominated by olivine and orthopyroxene and containing some plagioclase and a small amount of chromite. The residue composition assumed corresponds to that expected for a eutectic melt of a chondrite, as inferred based on the forsterite-nepheline-quartz system (Morse 1980), assuming that chromite is a restite mineral.

For most elements, models of 4–8% partial melting bracket the inferred compositions (Fig. 13). The overall agreement between the model batch melts and the parental melt for Sombrerete is excellent. The match between predicted and inferred melt compositions is better for Mn and especially for Rb assuming a CR-like (as opposed to H-like) chondritic precursor. This suggests that the protolith for Sombrerete could indeed have been a CR-like precursor, consistent with oxygen-isotope data.

The abundances of some elements (Ni especially, also Cr and to a lesser extent Ba) do not fit the simple partial melting model (Fig. 13), but the discrepancies for these elements can be understood. The abundance of Ni in the parental liquid is far lower than one would expect based on melting in a silicate system, and this clearly reflects the siderophile tendency of Ni and the partitioning of this element into metal. The Cr discrepancy may indicate an incorrect choice of *D* value for Cr, although the abundance of Cr in the parental melt may also have been underestimated if early chromite fractionation had occurred, as suggested by some data (see the "Filter-Press Differentiation" section). Finally, Ba contents in the parental

Table 6. CI-chondrite-normalized bulk composition of Som-4 and Som-1 calculated by combining SIMS, electron microprobe, and modal data, compared to an estimated parental liquid composition (see text). Values in parentheses are 1σ errors. CI-chondrite abundances of Anders and Grevesse (1989) were assumed.

	Som-4[a, b]	Som-1 apparent bulk[c, d]	Som-1 corrected bulk[a, d, e]	Model parental liquid[f]
Na	7.03 (0.55)	6.60 (0.26)	8.06 (0.32)	7.29 (0.32)
Mg	0.104 (0.014)	0.329 (0.024)	0.312 (0.022)	0.281 (0.022)
Si	2.10 (0.09)	2.63 (0.09)	2.49 (0.08)	2.24 (0.08)
P	11.7 (0.4)	7.20 (0.72)	15.5 (1.5)	28.6 (4.5)
K	7.38 (2.28)	5.62 (0.67)	6.99 (0.83)	6.29 (0.88)
Ca	4.02 (0.24)	4.06 (0.25)	6.08 (0.37)	9.61 (0.92)
Sc	1.26 (0.20)	3.06 (0.19)	2.93 (0.18)	2.75 (0.17)
Ti	14.7 (4.1)	8.34 (1.14)	11.3 (1.5)	10.2 (1.2)
V	10.9 (1.4)	0.385 (0.026)	0.369 (0.025)	0.346 (0.024)
Cr	28.5 (2.5)	0.195 (0.014)	0.173 (0.012)	0.161 (0.039)
Mn	0.772 (0.107)	1.10 (0.07)	0.920 (0.062)	0.825 (0.073)
Fe	0.335 (0.035)	0.177 (0.015)	0.181 (0.015)	0.189 (0.019)
Ni	0.006 (<0.001)	0.009 (0.002)	0.009 (0.002)	0.008 (0.001)
Rb	6.39 (0.49)	6.14 (0.86)	5.89 (0.82)	5.52 (0.77)
Sr	5.65 (1.19)	6.47 (0.43)	6.20 (0.41)	5.81 (0.38)
Y[g]	10.3 (0.9)	7.09 (0.67)	10.8 (1.3)	15.9 (1.9)
Zr	12.7 (1.7)	15.4 (0.6)	14.8 (0.6)	13.8 (0.6)
Nb	19.0 (2.3)	24.9 (1.9)	23.9 (1.9)	22.4 (1.7)
Ba	9.80 (1.33)	10.4 (0.9)	10.0 (0.9)	9.39 (0.83)
La	13.6 (0.8)	9.34 (0.94)	14.3 (1.8)	21.6 (2.7)
Ce	13.9 (0.9)	9.85 (0.96)	15.6 (2.0)	23.3 (2.9)
Pr	12.8 (1.0)	9.58 (1.02)	14.8 (2.0)	21.9 (2.9)
Nd	12.4 (1.2)	8.70 (0.90)	14.0 (1.9)	21.2 (2.9)
Sm	11.6 (0.7)	9.27 (1.05)	15.3 (2.3)	22.2 (3.3)
Eu	6.15 (0.91)	7.36 (0.73)	8.96 (0.98)	10.2 (1.1)
Gd	10.2 (0.8)	7.20 (0.94)	12.2 (2.1)	18.3 (3.2)
Tb	10.5 (0.7)	7.66 (0.87)	12.8 (1.9)	18.9 (2.9)
Dy	10.5 (1.1)	7.59 (0.76)	12.1 (1.5)	17.7 (2.3)
Ho	9.96 (0.89)	7.03 (0.67)	10.8 (1.3)	15.9 (1.9)
Er	9.00 (1.13)	6.84 (0.61)	10.5 (1.1)	14.6 (1.6)
Tm	7.95 (1.01)	7.20 (0.65)	10.8 (1.2)	14.2 (1.6)
Yb	6.88 (0.77)	8.01 (0.61)	12.1 (1.0)	14.9 (1.3)
Lu	7.10 (1.11)	6.70 (0.67)	9.09 (1.06)	11.4 (1.3)
Hf	13.2 (1.5)	19.3 (1.1)	18.6 (1.0)	17.4 (1.9)
Th[g]	12.5 (1.6)	9.95 (0.89)	13.5 (1.5)	17.4 (1.9)
U[g]	11.1 (1.0)	10.5 (1.0)	14.2 (1.7)	19.0 (2.2)

[a]Except where noted, assumes average composition of phases and arcs determined by electron microprobe (major elements, V in chromite) and by SIMS (trace elements).

[b]Omits suspect Ni value for 4Nagls1.

[c]Based on SIMS data, neglecting presence of apatite microlites.

[d]For glass and orthopyroxene, assumes 1Nagls2, 1Kgls2, and 1opx1 values.

[e]Takes into account Cl-apatite microlites, assuming 4 wt% total apatite (excluding that present in arcs) in Som-1.

[f]Assumed to be equivalent to corrected Som-1 bulk composition, except with an enhanced (10 wt% total) apatite component of average (Som-1 and Som-4) composition.

[g]CI-normalized abundances in apatite of Y, Th, and U assumed to be the same as for Ho, Er, and Ho, respectively (see text).

melt are somewhat lower than one would expect from the simple model (Fig. 13), and this probably indicates a problem in correctly estimating the composition of Ba in the parental melt. The Ba content in the parental melt would be a lower limit if the Ba content in phosphate was non-negligible, or if the amount of Ba-rich K-glass in Som-1 was underestimated.

A low-degree of partial melting is best able to explain the Ca-P-Cl-rich composition of Sombrerete inclusions. These elements are concentrated in clinopyroxene and phosphate in a chondritic precursor, which are among the first phases to melt (Feldstein et al. 2001; Jurewicz et al. 1995), so partial melting would place much of these elements into the melt fraction. The P/Ca ratio of the melt would be greater than chondritic if a greater proportion of Ca was retained in the source (e.g., in plagioclase), consistent with Sombrerete inclusions, which have a P/Ca ratio ~4 times that of a CR chondrite.

Still, one can ask whether the remarkably high P content of Sombrerete (an average 3.76 wt% P_2O_5 in inclusions, Table

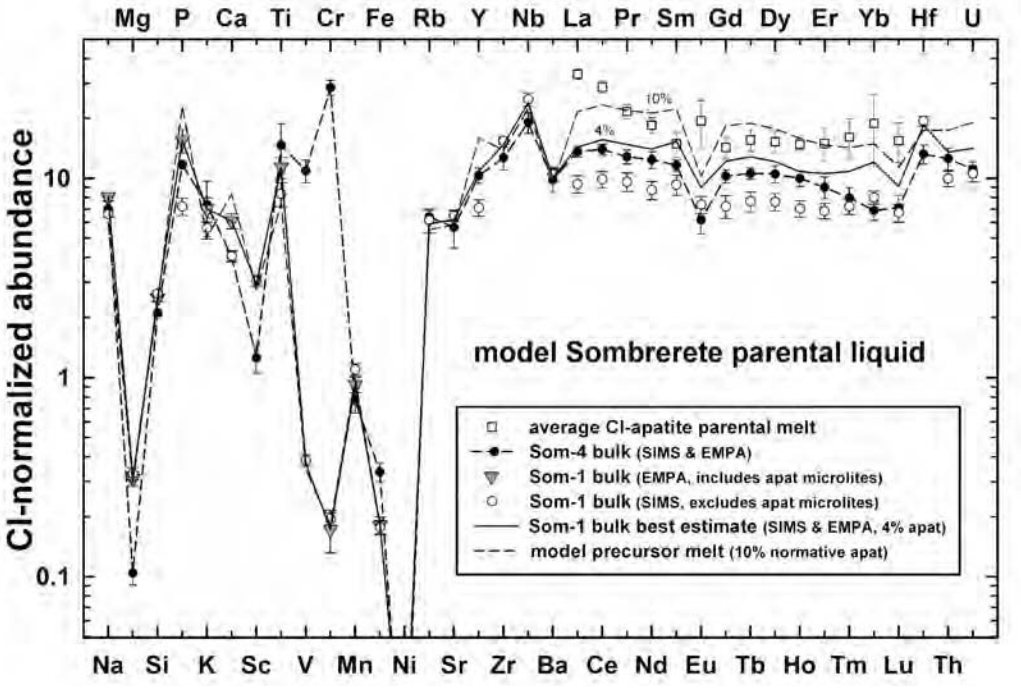

Fig. 12. A diagram showing compositions relevant for estimating the composition of a parental melt out of which Sombrerete inclusions could have crystallized (see text). This parent composition is taken to be similar to the calculated bulk composition of the Som-1 inclusion with an enhanced normative apatite (10 wt%) content (Som-1 "10% line"), and is similar to the composition of the calculated melt in equilibrium Cl-apatite microphenocrysts (squares). A correspondence between the bulk P and Ca contents determined for Som-1 from EMPA data (downward triangles) and the Som-1 "4% line" suggests that this inclusion contains ~4 wt% normative apatite excluding that present in arcs. The average CI-chondrite composition of Anders and Grevesse (1989) was used for normalization.

4) is consistent with simple partial melting of a chondritic precursor. Although D values for P are uncertain, a rough evaluation can be made. According to Ulmer (1989), $D_P^{ol/melt} \leq 0.01$ and $D_P^{opx/melt} = 0.03$, whereas Brunet and Chazot (2001) suggest $D_P^{ol/melt} \sim 0.1$ (where ol = olivine and opx = low-Ca pyroxene). Assuming that P does not partition into other minerals, a bulk partition coefficient of ~0.02–0.07 therefore seems reasonable. To produce the average inclusion composition with 4–8% partial melting, this implies a source region with ~970–2370 µg/g P, depending on the precise value of the partition coefficient. This rough estimate overlaps the range of 950–2130 µg/g P found in various chondrites (~1030 µg/g in CR chondrites) (Lodders and Fegley 1988). If D values are on the low end, good matches for a CR-chondrite protolith are obtained. Thus, provided that P is not sequestered in another mineral such as metal, the high P content of inclusions in Sombrerete does not appear to require special circumstances. The main requirements are a low degree of melting and sufficiently high fO_2 during melting and crystallization to keep P in an oxidized form.

Crystallization Models

Crystallization within inclusions was modeled using the SIMS data obtained for Som-1, 2, 3, and 4. These models test the validity of fractional crystallization (see the "Rapid Cooling and Crystallization" section), whether immiscibility was important for some elements (see the "Liquid Immiscibility" section), whether crystallization behaved in an open-system manner consistent with the filter-press mechanism (see the "Filter-Press Differentiation" section), and whether anomalies for Sm and Yb in glass reflect crystallization as will be argued later (the next section).

Models for fractional or equilibrium crystallization were devised assuming the same starting melt composition (model parental melt, Table 6) for three different types of mineral/melt partition coefficients (D values). The first method assumed representative values of equilibrium D values based on experiments (Appendix 3). The second assumed apparent D values for Sombrerete obtained from measured concentration ratios between minerals and glass (Appendix 4), and the last method assumed apparent D values based on mineral compositions and the bulk compositions of inclusions Som-1 and Som-4. The latter two methods gave generally acceptable results, but the first did not, possibly as a result of disequilibrium. In the models described below, only the results using apparent D values based on mineral/glass concentration ratios are discussed, although for some elements in phosphate for which no other data were available, literature D values were used. The use of apparent D values tests the ability to relate measured phase compositions to one another in a quantitative way, using the

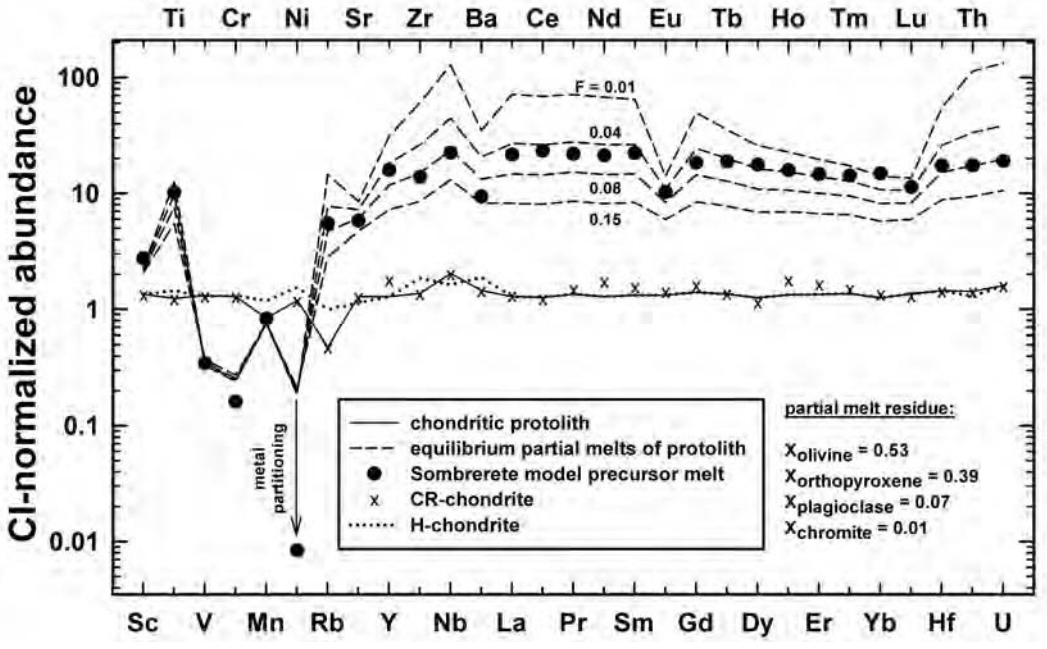

Fig. 13. The CI-chondrite-normalized abundance of the inferred parental melt in Sombrerete (filled circles) is compared to the composition of melts (dashed lines) produced by equilibrium (batch) partial melting of a chondritic precursor (taken to be a CR chondrite with average H-chondrite abundances of lanthanides and Y). The residue mineralogy is taken to be 53% olivine, 39% orthopyroxene, 7% plagioclase, and 1% chromite, reasonable for a low-degree partial melt of this type of precursor. The assumed D values (Appendix 3) are based mainly on representative experimental data for equilibrium partitioning. In general, an excellent correspondence between the inferred and modeled compositions is obtained, suggesting that the parental melts in Sombrerete were produced by ~4-8% partial melting. The CR- and H-chondrite compositions of Lodders and Fegley (1998) were assumed, and the average CI-chondrite composition of Anders and Grevesse (1989) was used for normalization.

standard equations for fractional and equilibrium-crystallization, but does not require that true equilibrium was achieved. The specific results given below are for best-fit cases, based on many trial calculations.

Som-4

The composition of Na-K-glass in Som-4 (type 1) can be explained by ~5–10% fractional crystallization of apatite and orthopyroxene in the relative proportion (by mass) of ~65/35, respectively (Fig. 14a). This inclusion contains no orthopyroxene, yet crystallization of orthopyroxene can explain the low abundances of ferromagnesian elements (Sc, V, Cr, Mn) in the glass, although conceivably chromite fractionation could also account for this depletion and may be needed to explain the especially low V and Cr contents (Fig. 14a). The models slightly overestimate the amount of Yb found in the glass (Fig. 14a), implying that the slight Yb excess in the model parental liquid did not exist for the liquids out of which Som-4 crystallized.

Som-1

The composition of Na-glass in Som-1 (type 3B) can be explained by ~20–30% fractional crystallization of apatite, orthopyroxene, and plagioclase in the relative proportion of ~20/31/49, respectively. These proportions are similar to those found in the inclusion, although the amount of orthopyroxene in the model is somewhat lower than observed. Positive Yb and Sm anomalies are present in both the glass and model liquids. Although the models and measured compositions agree for most elements, the measured Rb content in the Na-glass is much lower than predicted by the models (by a factor of ~5), and the measured Ba content is also lower (by a factor of ~2).

Som-3

The Na-glass in Som-3 (type 3B) has a highly fractionated composition, including large negative Yb and Sm anomalies and relatively low overall REE contents, which can be modeled as a result of ~30% fractional crystallization of apatite, merrillite, orthopyroxene, and plagioclase in the proportion of ~19/1/35/45, respectively (Fig. 14b). Except for merrillite, the implied amounts of crystallizing phases are in excess of the amount present in the inclusion. The model results strongly suggest that the low overall REE abundances and negative Yb and Sm anomalies of the glass in Som-3 are caused mainly by the fractionation of small quantities of merrillite enriched in these elements. Once again, the crystallization models do not account for the low Rb and Ba contents of the Na-glass (Fig. 14b). The observed contents of Ho and Y, as well as some elements that might concentrate in ilmenite (Ti, Zr, Nb, Hf), are also somewhat low compared to the model predictions, but

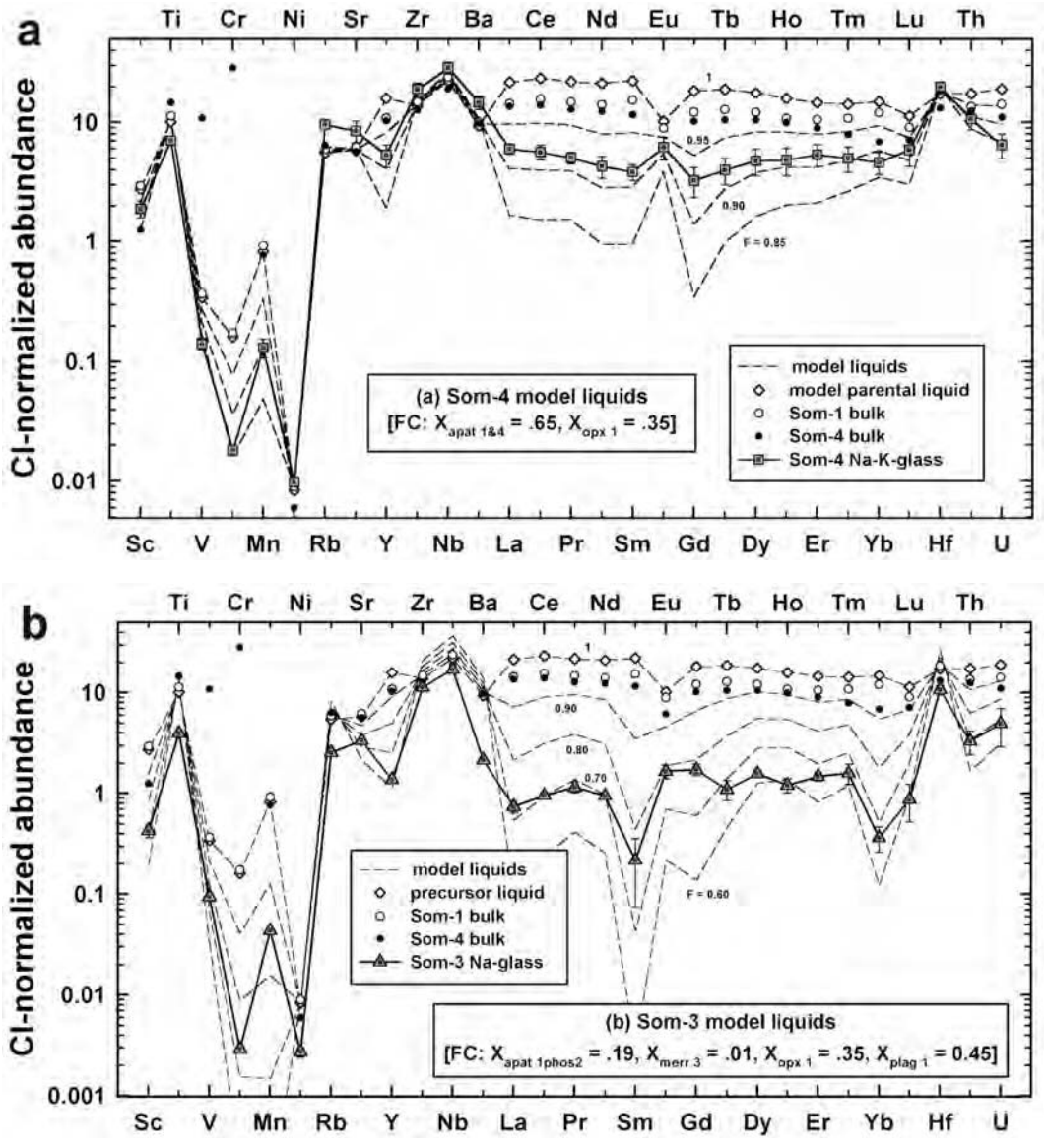

Fig. 14. Diagrams comparing model liquids produced by fractional crystallization (FC) to measured glass compositions in inclusions (a) Som-4 and (b) Som-3. *F* = fraction of liquid remaining; *X* = weight fraction of crystallizing phases (with subscripts showing the compositions that were assumed). Apparent mineral-melt partition coefficients (Appendix 4) were used (see text). In (b), model results for Th and U are illustrative only as they are based on uncertain *D* values for Th and U in merrillite (~360 and ~280, respectively), similar to the values inferred for LREE. The CI-normalized abundances of Anders and Grevesse (1989) were used for normalization.

overall the agreement is good considering the highly fractionated composition of the glass.

Som-2

The Na-glass in Som-2 (type 2) appears to record a complex history. The composition of this glass is best explained by a two-step model involving a) ~12% fractional crystallization of apatite, yagiite, and orthopyroxene in the ratio of ~38/6/56, followed by b) ~55% equilibrium crystallization of apatite, yagiite, and plagioclase in the ratio ~3/30/67, respectively. An equilibrium crystallization step involving yagiite is needed to explain the low Ba and Rb contents of the glass without depleting the glass too much in these elements, as would result from fractional crystallization alone. On the other hand, some fractional crystallization is needed to account for the overall abundances of many elements. The total amount of apatite, orthopyroxene, and plagioclase crystallization required by the models exceed the amount present in the inclusion. The best-fit models do a good job of matching the data for many elements, but the REEs are somewhat discrepant, and a better fit would result if the initial liquid had higher abundances of the LREE, and lower abundances of the HREE, with no initial positive Yb anomaly.

Summary

Crystallization models for Som-1, 2, 3, and 4 show that the varied glass compositions in these inclusions can be quantitatively explained to first order by varying degrees of crystallization of such phases as apatite, orthopyroxene, plagioclase, merrillite, and yagiite, assuming apparent *D* values based on mineral/glass concentration ratios. In all inclusions, fractional crystallization was a dominant process. For inclusions that contain K-glass (Som-1 and Som-3) or yagiite (Som-2 and Som-3), Rb and Ba abundances in Na-glass cannot be produced by fractional crystallization alone. In Som-1 and Som-3, which both contain appreciable K-glass, Rb and Ba probably were removed from Na melt and concentrated in K melt as a result of liquid immiscibility (see the "Liquid Immiscibility" section). For Som-2, some equilibrium crystallization of yagiite is also necessary. All four inclusions could have crystallized from a similar parental melt, although the positive Yb anomaly assumed for the precursor liquid was not widespread. Finally, the models provide evidence that crystallization did not always occur within the confines of the present inclusions, suggestive of open-system behavior such as proposed for filter-press differentiation (see the "Filter-Press Differentiation" section).

Origin of Yb and Sm Anomalies

A striking feature of the trace-element data is the presence of chondrite-normalized anomalies in Yb and Sm found in some analyses of Cl-apatite, merrillite, orthopyroxene, Na-glass, and K-glass. Similar, puzzling anomalies have been found in silicate inclusions from the Colomera and Miles (IIE) irons (Hsu et al. 1997; Hsu 2003; Takeda et al. 2003), as well as in silicate and sulfide minerals from enstatite chondrites and enstatite achondrites (e.g., Floss and Crozaz 1993; Crozaz and Lundberg 1995; Hsu and Crozaz 1998; Floss et al. 2003).

In Sombrerete, positive Yb and Sm anomalies are sometimes found in phosphates, and negative anomalies are sometimes found in glass and pyroxene. As shown in the previous section, the negative anomalies in the glass can be quantitatively explained by crystal-liquid fractionation of phosphates that contain positive anomalies. The same process can work to create negative anomalies in orthopyroxene, if the orthopyroxene crystallized from the same melt as a phosphate that had positive anomalies.

How the positive anomalies were established in the phosphates to begin with is not obvious. Such anomalies apparently cannot be explained on the basis of mineral-melt partitioning alone. However, Yb and Sm can become fractionated from other REE if a gas is present, as they are relatively volatile under reducing conditions (Boynton 1989; Lodders and Fegley 1993). Lodders and Fegley (1993) modeled condensation of the REE and actinides in oldhamite (CaS) under conditions of high C/O in the gas. For gas with C/O = 1.2, much more reducing than solar composition (C/O ~0.42), they found that relative REE volatilities decrease in the sequence Yb << Eu < Sm < Tm < other REE. This volatility sequence is independent of the mineral phase that is present, and depends only on the fO_2 of the gas and the equilibrium constants involved in forming different gaseous REE species (Boynton 1989).

We suggest that the positive anomalies in phosphate formed as a result of gas-melt-phosphate partitioning. If gas, melt, and phosphate are all present, mass balance requires:

$$C^{\text{bulk}} = (C^{\text{gas}} \cdot X_{\text{gas}}) + (C^{\text{melt}} \cdot X_{\text{melt}}) + (C^{\text{phos}} \cdot X_{\text{phos}}) \quad (1)$$

where C = mass concentration of an element in the bulk system and in the different phases, and X = mass fraction of the different phases. Defining $D^{\text{phos/melt}} = C^{\text{phos}}/C^{\text{melt}}$ and $D^{\text{phos/gas}} = C^{\text{phos}}/C^{\text{gas}}$, Equation 1 can be solved for $D^{\text{phos/melt}}$ as follows:

$$D^{\text{phos/melt}} = X_{\text{melt}} / [(C^{\text{bulk}}/C^{\text{phos}}) - X_{\text{phos}} - (X_{\text{gas}}/D^{\text{phos/gas}})] \quad (2)$$

Equation 2 shows that, if a gas is present, the compatibility of a given REE in phosphate depends in part on the value of $D^{\text{phos/gas}}$, as well as on the mass fractions of the different phases and the bulk partitioning ratio $C^{\text{bulk}}/C^{\text{phos}}$. If the element (e.g., Yb, Sm) is relatively volatile and the value of $D^{\text{phos/gas}}$ is relatively low, then the value of $D^{\text{phos/melt}}$ will tend to be relatively high (i.e., the element is relatively compatible in phosphate). This can be understood if the volatile element concentrates in gas primarily at the expense of liquid, and it would explain negative Yb and Sm anomalies in glass and orthopyroxene that solidified from such liquid. However, to account for positive anomalies of these same elements in phosphate, and to explain the complementary anomalies between phosphate and the coexisting phases, we suggest that not only is there a tendency for the volatile elements to move into gas relative to liquid, but that there is also a tendency for them to concentrate into phosphate relative to liquid, as a result of 3-phase partitioning effects. Whether this will occur cannot be determined without a more thorough thermodynamic and kinetic analysis. However, trial calculations for Sombrerete using Equation 2 show that for plausible bulk system and apatite compositions, large positive values in $D^{\text{phos/melt}}$ for Yb and Sm can result from combinations involving a small amount of phosphate (e.g., $X_{\text{phos}} \sim 0.01$) and a small amount of gas (e.g., $X_{\text{gas}} < 0.01$), if the concentration of Yb and Sm in the gas phase is comparable to or larger than in the phosphate. This could correspond to a melt-rich system with Yb and Sm being near their "condensation temperatures."

A reducing gas for Sombrerete is implied to create phosphate with Yb and Sm anomalies, but this gas was probably transitory. Equilibrium was not fully maintained, as shown by the spatially variable nature of the anomalies. Moreover, highly reducing conditions for Sombrerete seem inconsistent with the presence of relatively ferrous

orthopyroxene and chromite in the inclusions, and even with the phosphate itself, which is an oxygen-rich phase. We therefore suggest that the anomalies were produced at high temperature by the presence of a reducing gas that was quickly lost, under disequilibrium conditions. Extreme but short-lived reduction has been documented for soils affected by lightning strikes (Essene and Fisher 1986) and for experimentally shocked basaltic melts (Rowan and Ahrens 1994). A possible reduction mechanism for Sombrerete is the formation of a high-C/O gas by rapid heating of C-bearing target materials (e.g., graphite, organic compounds or carbides) or by the degassing of oxygen during hypervelocity impact.

This model is a variant of one originally proposed by Takeda et al. (2003) to account for Yb anomalies in phosphate and glass in Colomera (IIE iron) inclusions. These authors suggested that a gas could have helped to transport Yb from one phase to another after metal-silicate mixing, as a result of a redox reaction involving P-bearing metal, phosphate, and silicate melt. Our model is similar but emphasizes the effect of partitioning in the presence of a gas. In both models, exchange of Yb with gas would have occurred during crystallization of phosphate, which occurred relatively early in the solidification process for Sombrerete inclusions and at a later stage for Colomera inclusions.

If a transient gas was present in Sombrerete, it may have played a role in helping to transport inclusion liquids through the metallic host. A transport mechanism is needed to account for flow and differentiation phenomena in Sombrerete (see the "Fluid Flow" and "Filter-Press Differentiation" sections). A pressurized gas potentially offers a good way to accomplish such transport, as it could physically couple to the liquids and move these liquids down local pressure gradients.

Origin of Sombrerete

Important constraints for the origin of Sombrerete include the following: 1) the rounded shapes of inclusions and their igneous textures; 2) certain petrographic and phase-chemical features of the inclusions, such as their high glass content, fine grain size, often skeletal crystal morphologies, evidence that nucleation effects were important, and compositional variability of minerals and glasses; 3) the fractionated compositions of inclusions; 4) the fractionated composition of the host metal; 5) evidence that a reducing gas was present momentarily at start of inclusion crystallization; 6) evidence that silicate and phosphatic liquids flowed, both within inclusions and through the metallic matrix. In this section, these constraints are used to evaluate the origin of Sombrerete.

The first and last constraints imply that inclusions were originally liquid. As shown in this paper, the fractionated compositions of inclusions (constraint 3) can be explained by a combination of low-degree partial melting of a chondritic protolith together with subsequent crystal-liquid fractionation occurring while inclusion liquids were enclosed within metal. The second constraint implies rapid cooling and a lack of complete chemical equilibrium. The apparent presence of a reducing gas present momentarily at the start of crystallization (constraint 5) also suggests a rapidly evolving system, one in which conditions were changing quickly at high temperature. There is thus no doubt that following partial melting, inclusions solidified near a cooling surface, not deep within the parent body.

The metallic host was probably also substantially liquid, as suggested by the rounded shapes of the inclusions (constraint 1), the apparent ability for inclusion liquids to flow through metallic host (constraint 6) without creating large void spaces, and the fractionated composition of the metal (constraint 4). Iridium is a compatible element in metallic systems and will concentrate in solid Fe-Ni metal relative to metallic liquid, so its low abundance in Sombrerete suggests that the metal host represents a liquid fraction, similar to the silicate it encloses.

In principle, such metallic liquid could have been produced during fractional crystallization, in a process similar to that believed to have affected magmatic iron meteorites (e.g., Hutchison 2004). A simple calculation for Ir can be made using the fractional crystallization equation ($C_L/C_o = F^{[D-1]}$), where F = liquid fraction, C_L/C_o = the concentration in metallic liquid normalized to the starting concentration, and D = (solid metal)/(liquid metal) partition coefficient. Taking $C_L/C_o = 0.02$ (C_o = H-chondrite metal) and $D_{Ir} \sim 4$, the value estimated for a metallic melt of H-chondrite composition (using the D value parameterization of Chabot and Jones 2003 and the overall procedure of Ruzicka et al. 2005 to find the appropriate metal composition), one gets $F = 0.27$. In other words, using a traditional model for magmatic iron meteorites, the low Ir content of Sombrerete metal can be explained as the metallic liquid remaining after ~73% fractional crystallization of metal in a typical chondritic system.

Conceivably, inclusion liquids could have been floating as immiscible blobs in metallic liquid that was itself undergoing extensive fractional crystallization. However, if solid and liquid metal were separating from one another in this way, it is unclear why liquid silicate and liquid metal did not separate completely, as the density contrast between liquid silicate and liquid metal would have been larger than between liquid and solid metal. Moreover, extensive fractional crystallization of the metallic liquids seems unlikely, as rapid cooling (constraint 2) might not provide the time needed for gravitational settling of solid from liquid metal.

More likely, the fractionated metal in Sombrerete was produced by partial melting. Metallic liquid with an Ir content of ~2% of the starting composition, as implied for Sombrerete metal, can be obtained with ~50% equilibrium partial melting in the Fe-Ni-S system, assuming an H-chondrite-like metallic system (Ruzicka et al. 2005) and the D value parameterization of Chabot and Jones (2003). This melt fraction corresponds to a temperature of ~1300 °C (Hsieh et al. 1987), somewhat higher than one would expect for the low degree of melting implied for the silicate inclusions. However, a partial melt

origin for the metal has the advantage of being able to produce metal and inclusion liquid by the same process, potentially much more quickly than a fractional crystallization origin for the metal would allow.

Thus, the evidence suggests that both silicate and metal formed as liquid fractions by partial melting of a chondritic protolith, and that this liquid solidified rapidly near a cooling surface. The heat source responsible for partial melting could have been either purely endogenic (e.g., caused by the decay of short-lived radionuclides), purely exogenic (i.e., hypervelocity impact), or some combination of these.

We argue that endogenic or exogenic processes operating alone are inconsistent with the data for Sombrerete. The only endogenic process seemingly capable of producing a rapidly cooled metal-silicate rock is a gas-charged eruption (Wilson and Keil 1991; Keil and Wilson 1993) that would rapidly deliver these components to a cooling surface. However, it is very unlikely that any gas-charged eruption could bring a metal-rich melt to the surface as large as or larger than the ~10 kg mass of Sombrerete without dispersing the magma into small pieces (pyroclasts). Additionally, gas-charged melts could move so rapidly that they would be lost from all but the largest parent bodies altogether (Wilson and Keil 1991; Keil and Wilson 1993; Keil 2000), making it impossible to produce Sombrerete this way. On the other hand, it is not obvious how impact heating could produce the fractionated liquid composition of Sombrerete. Keil et al. (1997) suggest that impacts do not produce large volumes of fractionated partial melts, based on theoretical studies and observations of terrestrial impact crater rocks. Moreover, any collisional event sufficiently intense to result in significant impact melting could also result in permanent collisional disruption of the parent body (Stöffler et al. 1988) or in the permanent loss from the parent body of much impact-melt ejecta (Keil et al. 1997), which would appear to limit the feasibility of the process. However, others have argued that impacts can produce a significant, albeit localized, amount of impact melt on porous targets immediately below the impact contact point (Rubin 2005).

On balance, we favor a model in which simultaneous endogenic heating and impact played an important role in the origin of Sombrerete. We suggest that endogenic heating (e.g., by decay of short-lived radionuclides) was the principal heat source involved in partial melting, and that it produced silicate and metallic liquids that had not separated much from one another, owing to the large proportion of unmelted solid. In our view, dynamical forces during a collision occurring simultaneously with endogenic heating served as the main way to separate metallic and silicate liquids from solids, to bring these materials close to a cooling surface, and to concentrate them in the Sombrerete-forming region. Although impact-induced metal-silicate mixing is widely believed to have been involved in producing various silicate-bearing iron meteorites (e.g., Wasson and Wang 1986; Ruzicka et al. 1999; Benedix et al. 2000; Bogard et al. 2000; Wasson and Kallemeyn 2002; Hsu 2003; Takeda et al. 2003), for Sombrerete such impact-induced processes would have had to separate liquids from solids, with the liquid fraction corresponding to the meteorite. This separation may have arisen owing to a different response of liquid and solid to stress waves during shock. Rapid cooling of Sombrerete suggests that the impact event responsible for liquid-solid separation and metal-silicate mixing disrupted the planetesimal, temporarily breaking it apart into smaller pieces that cooled quickly. Reaccretion of the smaller pieces into a second-generation (and possibly much smaller) planetesimal would be needed to facilitate long-term storage of the material for eventual delivery to Earth. In this model, although endogenic heating is considered to be the primary heating mechanism, impact processes are critical for enabling solid-liquid separation, metal-silicate mixing, and rapid cooling to occur. Collisional disruption of the parent body is envisioned to be the main reason why differentiation was arrested in it.

Although this model is reminiscent of parent body breakup models proposed for IVA and IAB irons (Haack et al. 1996; Benedix et al. 2000), it differs in some important ways. Far from the random mixture of solid and liquid components envisioned for the reaccreted IVA and IAB bodies (Haack et al. 1996; Benedix et al. 2000), Sombrerete is composed of fractionated liquid components only, which probably requires that any reaccreted body was composed of liquids that were separated from solids during the breakup event. Moreover, unlike IVA and IAB irons, excavated materials for Sombrerete cooled rapidly and would have had to end up close to the cooling surface of a reaccreted body.

In some ways, the proposed model for Sombrerete of simultaneous endogenic heating and impact mobilization is similar to what is believed to have occurred for the unique, metallic-melt breccia Portales Valley (H7), which has affinities to silicate-bearing IIE iron meteorites (Ruzicka et al. 2005). However, the situation between Portales Valley and Sombrerete is totally different in that only Sombrerete shows evidence for substantial differentiation, rapid cooling, and a parent body breakup event.

Implications for Other Silicate-Bearing Irons

If the Sombrerete parent body formed by simultaneous internal heating and collision, the same may be true of other silicate-bearing irons. The petrology of Sombrerete most closely resembles certain silicate-bearing IIE irons whose inclusions have nonchondritic mineralogies and fractionated bulk compositions, including Colomera, Miles, Kodaikanal, Weekeroo Station, and Elga (e.g., Prinz et al. 1983; Bogard et al. 2000); the ungrouped Guin iron is similar (Rubin et al. 1986). All of these “evolved IIE-type” meteorites contain alkali-silica-rich globular-to-ameboid inclusions, some of

which are glassy. As with Sombrerete, Colomera contains yagiite and phosphate-rich segregations (Bogard et al. 2000; Takeda et al. 2003) and may have been affected by K-Na melt immiscibility (see the "Liquid Immiscibility" section), and Colomera and Miles have localized Yb anomalies (see the "Origin of Yb and Sm Anomalies" section). These properties suggest a similar origin for the evolved IIE-type irons, with Colomera being a particularly close analog to Sombrerete.

Previous studies concluded that the evolved IIE irons formed by partial melting and impact-induced metal-silicate mixing (Prinz et al. 1982, 1983; Rubin et al. 1986; Ruzicka et al. 1999; Bogard et al. 2000; Snyder et al. 2001; Takeda et al. 2003; Hsu 2003), consistent with our conclusions. Although there has been widespread agreement that metal-silicate mixing occurred as a result of impact processes, there has been disagreement as to the nature of the heat source, either impact-induced partial melting (Prinz et al. 1982, 1983; Snyder et al. 2001) or endogenic heating (Bogard et al. 2000; Takeda et al. 2003). The situation for Weekeroo Station, Miles, and Colomera is blurred further in that they show evidence for two melting events, an early one that resulted in coarse pyroxene and plagioclase grown under near-equilibrium conditions, and a later one that resulted in partial remelting of feldspathic materials, producing glass and fine-grained feldspathic materials (Ruzicka et al. 1999; Bogard et al. 2000; Takeda et al. 2003; Hsu 2003).

We suggest that our model for Sombrerete involving impact-induced disruption of an already partly molten parent body is also applicable to the evolved IIE irons. Impact disruption is consistent with the rapid cooling environment needed to produce the observed glassy and quench textures, and impact could have resulted in partial remelting of feldspathic materials. Similarly, coarser pyroxene and plagioclase could have formed in the original crystal mush inferred to have been present during partial melting (Takeda et al. 2003) prior to impact. Differences in silicate inclusions between the evolved irons in terms of grain sizes and textures could partly reflect the proportion of coarse silicates and melt in the original crystal mush, the extent of impact-induced remelting, and the way in which solid and liquid components were mixed with metal. If, as we infer, the evolved IIEs and Guin formed in essentially the same way as Sombrerete, at least three parent body breakup events are required, one each for Sombrerete, Guin, and the fractionated IIEs, owing to their different isotopic and chemical characteristics (see Introduction).

This model of simultaneous endogenic heating and impact is also consistent with the predominantly old (>4.3 Ga) ages inferred for the evolved IIE irons (Bogard et al. 2000), as potential endogenic heat sources such as short-lived radionuclide decay would have been effective only in the earliest moments of solar system history (e.g., Hutchison 2004). Only evolved Kodaikanal with an apparently young age (~3.7 Ga) is possibly inconsistent with early differentiation, although this age could reflect late shock heating of an early differentiate (Bogard et al. 2000). Moreover, caution must be used in interpreting age data for silicate inclusions, as shock melting events could have been manifested in different ways with different chronometers, depending on which phases were remelted (Snyder et al. 2001).

Simultaneous internal heating and collision is also compatible with the properties of the unfractionated IIE irons Watson, Netschaëvo, and Techado, provided they were derived from a parent body that was not considerably molten prior to impact. At the time of metal-silicate mixing, silicates were molten but not fractionated in Watson and they were largely unmolten in Netschaëvo and Techado (e.g., Olsen et al. 1994; Bogard et al. 2000). These meteorites have been interpreted as reflecting heating that was capable of melting silicate in Watson and mobilizing metal in Netschaëvo and Techado (Olsen et al. 1994; Bogard et al. 2000). This heating could have occurred during a collision while the parent body was being internally heated to metamorphic temperatures, as was proposed for the H-group Portales Valley meteorite, which is very similar to Netschaëvo (Ruzicka et al. 2005). There is little evidence for rapid cooling in the silicates of the unfractionated IIEs and no reason to believe that their parent body was collisionally disrupted. We consider it improbable that any of these meteorites originated on the same parent body as for the evolved IIE irons, as only the latter were differentiated. This implies that there could have been at least one additional parent body undergoing simultaneous internal heating and collision, and that this body (possibly the H-chondrite parent body) was undifferentiated.

Finally, similar processes of internal heating and collisional disruption may have affected the parent bodies of IVA and IAB meteorites (Haack et al. 1996; Benedix et al. 2000). If so, considering the variety of IAB meteorites (Wasson and Kallemeyn 2002) and the distinct oxygen-isotope compositions of IABs and IVAs (both different from IIE, Guin, and Sombrerete), two or more additional simultaneous heating/breakup events on different bodies can be postulated.

Thus, at least six parent bodies for silicate-bearing irons could have experienced simultaneous impact and endogenic heating, some of which were probably collisionally disrupted. This suggests that many planetesimals in the early solar system were colliding while they were hot, and that this process could have widely affected solar system matter.

CONCLUSIONS

Petrographic and geochemical data suggest that Sombrerete and the silicate inclusions it contains formed by complex differentiation and crystallization phenomena. Inclusions contain variable proportions of different types of quartzofeldspathic glass, aluminous orthopyroxene, plagioclase, Cl-apatite, chromite, yagiite, phosphate-rich

segregations that have arc- and orb-like forms, ilmenite, merrillite, rare SiO_2 polymorph, and a mixed phase that could be a decomposed kaersutite amphibole. Phosphate-rich segregations formed by immiscible separation of P-rich liquids, and Na-glass and K-glass formed by immiscible separation of alkali and alkali earth elements from Na-K-rich melt. Textural and mineralogical variations between inclusions are best explained as a result of differences in crystallization history during rapid cooling. Fractional crystallization was a dominant process, and yagiite crystallized late in an approach to equilibrium crystallization, possibly aided by immiscibility. The bulk compositions of inclusions are highly fractionated and best explained by a two-step differentiation model, with the first step involving low-degree partial melting (~4–8%) of a chondritic precursor, and the second step involving mainly fractional crystallization while inclusion liquids were enclosed in the metallic host. The first process resulted in a parental liquid that can be described as a phosphoran basaltic andesite; the second resulted in inclusion melts as siliceous as dacite. Differentiation within the metallic host appears to have occurred as a result of a filter-press mechanism, in which crystals of apatite, orthopyroxene, and other minerals were less able than residual liquids to flow through the metallic host. Ytterbium and Sm anomalies are sometimes found in various phases and may have formed by phosphate-melt-gas partitioning under highly reducing conditions; such a gas would have been present momentarily at the start of inclusion crystallization. Solidification in Sombrerete was relatively rapid, but not so fast as to prevent flow, crystallization, and immiscible separation of liquids. Sombrerete formed by rapid mixing of metallic and silicate liquids near a cooling surface, most likely as a result of a major collision that affected a partly molten parent body. At least six separate meteorite parent bodies and possibly many more may have experienced a similar process of simultaneous impact and internal heating to produce various silicate-bearing iron meteorites. The data support the idea that high impact fluxes may have characterized the earliest moments of solar system history.

Acknowledgments–A substantial contribution to this work was made by Martin Prinz (deceased), who stimulated the first author's interest in the origin of silicate-bearing iron meteorites, and who made available thin sections, bulk samples, and data for Sombrerete before his health failed. The authors wish to dedicate this paper to the memory of Marty, both for his contributions to this specific project and the many others he made over the years to the meteoritical community. Constructive and comprehensive reviews of this manuscript by Mitsuru Ebihara, Alfred Kracher, Dave Mittlefehldt, Alan Rubin, Ed Scott, and Tim McCoy are appreciated. This work was supported by NASA grants NAG5-12856 (A. R.) and NNG04GB37G (C. F.).

Editorial Handling—Dr. Edward Scott

REFERENCES

Alexander C. M. O. D. 1994. Trace element distributions within ordinary chondrite chondrules: Implications for chondrule formation conditions and precursors. *Geochimica et Cosmochimica Acta* 58:3451–3467.

Anders E. and Grevesse N. 1989. Abundances of the elements: Meteoritic and solar. *Geochimica et Cosmochimica Acta* 53:197–214.

Bacon C. R. and Druitt T. H. 1988. Compositional evolution of the zoned calcalkaline magma chamber of Mount Mazama, Crater Lake, Oregon. *Contributions to Mineralogy and Petrology* 98: 224–256.

Beatty P. 1993. The effect of partial melting of spinel peridotite on uranium series disequilibria: Constraints from partitioning studies. *Earth and Planetary Science Letters* 177:379–391.

Beatty P. 1994. Systematics and energetics of trace-element partitioning between olivine and silicate melts: Implications for the natural of mineral/melt partitioning. *Chemical Geology* 117: 57–71.

Benedix G. K., McCoy T. J., Keil K., and Love S. G. 2000. A petrologic study of IAB iron meteorites: Constraints on the formation of the IAB-winonaite parent body. *Meteoritics & Planetary Science* 35:1127–1141.

Benjamin T. M., Jones J. H., Heuser W. R., and Burnett D. S. 1983. Laboratory actinide partitioning: Whitlockite/liquid and influence of actinide concentration levels. *Geochimica et Cosmochimica Acta* 47:1695–1705.

Best M. G. 1982. *Igneous and metamorphic petrology.* New York: W. H. Freeman and Company. 630 p.

Bindemann I. N., Davis A. M., and Drake M. J. 1998. Ion microprobe study of plagioclase-basalt partition experiments at natural concentration levels of trace elements. *Geochimica et Cosmochimica Acta* 62:1175–1193.

Bogard D. D., Garrison D. H., and McCoy T. J. 2000. Chronology and petrology of silicates from IIE iron meteorites: Evidence of complex parent body evolution. *Geochimica et Cosmochimica Acta* 64:2133–2154.

Bougalt H. and Hekinian R. 1974. Rift valley in the Atlantic Ocean near 36°50′N: Petrology and geochemistry of basaltic rocks. *Earth and Planetary Science Letters* 24:249–261.

Boynton W. V. 1989. Cosmochemistry of the rare earth elements: Condensation and evaporation processes. In *Geochemistry and mineralogy of rare earth elements*, edited by Lipin B. R. and McKay G. A. Washington, D.C.: Mineralogical Society of America. pp. 1–24.

Brunet F. and Chazot G. 2001. Partitioning of phosphorus between olivine, clinopyroxene and silicate glass in a spinel lherzolite xenolith from Yemen. *Chemical Geology* 176:51–72.

Bunch T. E. and Fuchs L. H. 1969. Yagiite, a new sodium-magnesium analogue of osumilite. *American Mineralogist* 54:14–18.

Buchwald V. 1975. *Handbook of iron meteorites.* Berkeley, California: University of California Press. 1418 p.

Chabot N. L. and Jones J. H. 2003. The parametrization of solid metal-liquid metal partitioning of siderophile elements. *Meteoritics & Planetary Science* 38:1425–1436.

Chou C.-L., Baedecker A. A., and Wasson J. T. 1973. Distribution of Ni, Ga, Ge and Ir between metal and silicate portions of H-group chondrites. *Geochimica et Cosmochimica Acta* 37:2159–2171.

Colson R. O., McKay G. A., and Taylor L. A. 1988. Temperature and composition dependencies of trace element partitioning: Olivine/

melt and low-Ca pyroxene/melt. *Geochimica et Cosmochimica Acta* 52:539–553.

Crozaz G. and Lundberg L. 1995. The origin of oldhamite in unequilibrated enstatite chondrites. *Geochimica et Cosmochimica Acta* 59:3817–3831.

Dostal J., Dupuy C., Carron J. P., Le Guen de Kerneizan M., and Maury R. C. 1983. Partition coefficients of trace elements: Application to volcanic rocks of St. Vincent, West Indies. *Geochimica et Cosmochimica Acta* 37:525–533.

Drake M. J. and Weill D. F. 1975. The partition of Sr, Ba, Ca, Y, Eu^{2+}, Eu^{3+} and other REE between plagioclase feldspar and magmatic silicate liquid. *Geochimica et Cosmochimica Acta* 39:689–712.

Duke J. M. 1976. The distribution of the period four transition elements among olivine, calcic clinopyroxene and mafic silicate liquid. *Journal of Petrology* 17:499–521.

Dunn T. 1987. Partitioning of Hf, Lu, Ti, and Mn between olivine, clinopyroxene and basaltic liquid. *Contributions to Mineralogy and Petrology* 96:476–484.

Dunn T. and Sen C. 1994. Mineral/matrix partition coefficients for orthopyroxene, plagioclase, and olivine in basaltic to andesitic systems: A combined analytical and experimental study. *Geochimica et Cosmochimica Acta* 58:717–733.

Essene E. J. and Fisher D. C. 1986. Lightning strike fusion: Extreme reduction and metal-silicate liquid immiscibility. *Science* 234: 189–193.

Ewart A., Bryan W. B., and Gill J. 1973. Mineralogy and geochemistry of the younger volcanic islands of Tonga, S.W. Pacific. *Journal of Petrology* 14:429–465.

Ewart A. and Griffen W. L. 1994. Applications of proton-microprobe data: Trace-element partitioning in volcanic rocks. *Chemical Geology* 117:251–284.

Feldstein S. N, Jones R. H., and Papike J. J. 2001. Disequilibrium partial melting experiments on the Leedey L6 chondrite: Textural controls on melting processes. *Meteoritics & Planetary Science* 36:1421–1441.

Floss C. and Crozaz G. 1993. Heterogeneous REE patterns in oldhamite from aubrites: Their nature and origin. *Geochimica et Cosmochimica Acta* 57:4039–4057.

Floss C. and Jolliff B. 1998. Rare earth element sensitivity factors in calcic plagioclase (anorthite). In *Secondary ion mass spectrometry, SIMS XI*, edited by Gillen G., Lareau R., Bennett J., and F. Stevie. New York: John Wiley & Sons. pp. 785–788.

Floss C., James O. B., McGee J. J., and Crozaz G. 1998. Lunar ferroan anorthosite petrogenesis: Clues from trace element distributions in FAN subgroups. *Geochimica et Cosmochimica Acta* 62:1255–1283.

Floss C., Fogel R. A., Lin Y., and Kimura M. 2003. Diopside-bearing EL6 EET 90102: Insights from rare earth element distributions. *Geochimica et Cosmochimica Acta* 67:543–555.

Freestone I. C. 1978. Liquid immiscibility in alkali-rich magmas. *Chemical Geology* 23:115–123.

Frey F. A. 1969. Rare earth abundances in a high-temperature peridotite intrusion. *Geochimica et Cosmochimica Acta* 33: 1429–1447.

Fujimaki H. 1986. Partition coefficients of Hf, Zr, and REE between zircon, apatite, and liquid. *Contributions to Mineralogy and Petrology* 94:42–45.

Fujimaki H. and Tstsumoto M. 1984. Partition coefficients of Hf, Zr and REE between phenocrysts and groundmass. *Journal of Geophysical Research* 89:662–672.

Gaetani G. A. and Grove T. L. 1997. Partitioning of rare earth elements between clinopyroxene and silicate melt: Crystal-chemical controls. *Geochimica et Cosmochimica Acta* 59:1951–1962.

Gaines R. V., Skinner C. W., Foord E. E., Mason B., and Rosenzweig A. 1997. *Dana's new mineralogy: The system of mineralogy of James Dwight Dana and Edward Salisbury Dana.* New York: John Wiley & Sons. 1819 p.

Garrison D., Hamlin S., and Bogard D. 2000. Chlorine abundances in meteorites. *Meteoritics & Planetary Science* 35:419–429.

Green D. H., Ringwood A. E., Ware N. G., Hibberson W. O., Major A., and Kiss E. 1971. Experimental petrology and petrogenesis of Apollo 12 basalts. Proceedings, 2nd Lunar Science Conference. pp. 601–615.

Green T. H. 1994. Experimental studies of trace-element partitioning applicable to igneous petrogenesis—Sedona 16 years later. *Chemical Geology* 117:1–36.

Haack H., Scott E. R. D., Love S. G., Brearley A. J., and McCoy T. J. 1996. Thermal histories of IVA stony-iron and iron meteorites: Evidence for asteroid fragmentation and reaccretion. *Geochimica et Cosmochimica Acta* 60:3103–3113.

Hsieh K.-C., Vlach K. C., and Chang Y. A. 1987. The Fe-Ni-S system, I. A thermodynamic analysis of the phase equilibria and calculation of the phase diagram from 1173 to 1623 K. *High Temperature Science* 23:17–38.

Hsu W. 1995. Ion microprobe studies of the petrogenesis of enstatite chondrites and eucrites. Ph.D. thesis. Washington University, Saint Louis, Missouri, USA.

Hsu W. 2003. Rare earth element geochemistry and petrogenesis of Miles (IIE) silicate inclusions. *Geochimica et Cosmochimica Acta* 67:4807–2821.

Hsu W., Takeda H., Huss G. R., and Wasserburg G J. 1997. Mineralogy and chemical compositions of Colomera (IIE) silicate inclusions. *Meteoritics & Planetary Science* 32:A61–62.

Hsu W. and Crozaz G. 1998. Mineral chemistry and the origin of enstatite in unequilibrated chondrites. *Geochimica et Cosmochimica Acta* 62:1993–2004.

Huang C. and Cormack A. N. 1991. Structural differences and phase separation in alkali silicate glasses. *The Journal of Chemical Physics* 95:3634–3642.

Hutchison R. 2004. *Meteorites: A petrologic, chemical and isotopic synthesis.* Cambridge: Cambridge University Press. 506 p.

Hutchison R. and Bevan A. W. R. 1983. Conditions and time of chondrule accretion. In *Chondrules and their origins,* edited by King E. A. Houston: Lunar and Planetary Institute. pp. 162–179.

Irving A. J. 1978. A review of experimental studies of crystal/liquid trace element partitioning. *Geochimica et Cosmochimica Acta* 42:743–770.

Irving A. J. and Frey F. A. 1984. Trace element abundances in megacrysts and their host basalts: Constraints on partition coefficients and megacryst genesis. *Geochimica et Cosmochimica Acta* 48:1201–1221.

Jarosewich E. 1990. Chemical analyses of meteorites: A compilation of stony and iron meteorite analyses. *Meteoritics* 25:323–337.

Jolliff B. L., Haskin L. A., Colson R. O., and Wadhwa M. 1993. Partitioning in REE-saturating minerals: Theory, experiment, and modelling of whitlockite, apatite, and evolution of lunar residual magmas. *Geochimica et Cosmochimica Acta* 57:4069–4094.

Jones R. H. and Layne G. D. 1997. Minor and trace element partitioning between pyroxene and melt in rapidly cooled chondrules. *American Mineralogist* 82:534–545.

Jurewicz A. J. G., Mittlefehldt D. W., and Jones J. H. 1995. Experimental partial melting of the St. Severin (LL) and Lost City (H) chondrites. *Geochimica et Cosmochimica Acta* 59:391–408.

Keil K. and Wilson L. 1993. Explosive volcanism and the compositions of cores of differentiated asteroids. *Earth and Planetary Science Letters* 117:111–124.

Keil K., Stöffler D., Love S. G., and Scott E. R. D. 1997. Constraints

on the role of impact heating and melting in asteroids. *Meteoritics* 32:349–363.
Keil K. 2000. Thermal alteration of asteroids: Evidence from meteorites. *Planetary and Space Sciences* 48:887–903.
Keleman P. B. and Dunn J. T. 1992. Depletion of Nb relative to other highly incompatible elements by melt/rock reaction in the upper mantle. *Eos* 73:656–657.
Kennedy A. K., Lofgren G. E., and Wasserburg G. J. 1993. An experimental study of trace element partitioning between olivine, orthopyroxene and melt in chondrules: Equilibrium values and kinetic effects. *Earth and Planetary Science Letters* 115:177–195.
Klock W. and Palme H. 1988. Partitioning of siderophile and chalcophile elements between sulfide, olivine, and glass in a naturally reduced basalt from Disko Island, Greenland. Proceedings, 18th Lunar and Planetary Science Conference. pp. 471–483.
Koblitz J. 2003. MetBase-Meteorite data retrieval software. MetBase version 6.0 for Windows. CD-ROM.
Kong P. and Ebihara M. 1996. Metal phases of L chondrites: Their formation and evolution in the nebula and in the parent body. *Geochimica et Cosmochimica Acta* 60:2667–2680.
Kong P., Ebihara M., Nagahara H., and Endo K. 1995. Chemical characteristics of metal phases of the Richardton H5 chondrite. *Earth and Planetary Science Letters* 136:407–419.
Lodders K. and Fegley B., Jr. 1993. Lanthanide and actinide chemistry at high C/O ratios in the solar nebula. *Earth and Planetary Science Letters* 117:125–145.
Lodders K. and Fegley B., Jr. 1998. *The planetary scientist's companion.* New York: Oxford University Press. 371 p.
Luhr J. F. and Carmichael I. S. E. 1980. The Colima volcanic complex, Mexico. 1: Post-caldera andesites from Volcan Colima. *Contributions to Mineralogy and Petrology* 71:343–372.
Malvin D. J., Wang D., and Wasson J. T. 1984. Chemical classification of iron meteorites. X—Multielement studies of 43 irons, resolution of group IIIE from IIIAB, and evaluation of Cu as a taxonomic parameter. *Geochimica et Cosmochimica Acta* 48:785–804.
Mahood G. A. and Stimac J. A. 1990. Trace-element partitioning in pantellerites and trachytes. *Geochimica et Cosmochimica Acta* 54:2257–2276.
Mayeda T. K. and Clayton R. N. 1980. Oxygen isotopic compositions of aubrites and some unique meteorites. Proceedings, 11th Lunar and Planetary Science Conference. pp. 1145–1151.
McKay G. A. and Weill D. F. 1976. Petrogenesis of KREEP. Proceedings, 7th Lunar Science Conference. pp. 2427–2447.
McKay G. A. and Weill D. F. 1977. KREEP petrogenesis revisited. Proceedings, 8th Lunar Science Conference. pp. 2339–2355.
Morse S. A. 1980. *Basalts and phase diagrams: An introduction to the quantitative use of phase diagrams in igneous petrology.* New York: Springer-Verlag. 493 p.
Nielsen R. L., Gallahan W. E., and Newberger F. 1992. Experimentally determined mineral-melt partition coefficients for Sc, Y and REE for olivine, orthopyroxene, pigeonite, magnetite and ilmenite. *Contributions to Mineralogy and Petrology* 110:488–499.
Olsen E., Davis A., Clarke R. S., Schultz L., Weber H. W., Clayton R., Mayeda T., Jarosewich E., Sylvester P., Grossman L., Wang M.-S., Lipschutz M. E., Steele I. M., and Schwade J. 1994. Watson: A new link in the IIE iron chain. *Meteoritics* 29:200–213.
Paster T. P., Schauwecher D. S., and Haskin L. A. 1974. The behavior of some trace elements during solidification of the Skaergaard layered series. *Geochimica et Cosmochimica Acta* 38:1549–1577.
Prinz M., Nehru C. E., and Delaney J. S. 1982. Sombrerete: An iron with highly fractionated amphibole-bearing Na-P-rich silicate inclusions (abstract). 13th Lunar and Planetary Science Conference. pp. 634–635.
Prinz M., Nehru C. E., Delaney J. S., Weisberg M., and Olsen E. 1983. Globular silicate inclusions in IIE irons and Sombrerete: Highly fractionated minimum melts (abstract). 14th Lunar and Planetary Science Conference. pp. 618–619.
Rambaldi E. 1976. Trace-element content of metals from L chondrites. *Earth and Planetary Science Letters* 31:224–238.
Rambaldi E. R. 1977. Trace element content of metals from H- and LL-group chondrites. *Earth and Planetary Science Letters* 36:347–358.
Roedder E. 1978. Silicate liquid immiscibility in magmas and in the system K_2O-FeO-Al_2O_3-SiO_2: An example of serendipity. *Geochimica et Cosmochimica Acta* 42:1597–1617.
Roedder E. 1979. Silicate liquid immiscibility in magmas. In *The evolution of the igneous rocks,* edited by Yoder H. S. Princeton, New Jersey: Princeton University Press. pp. 15–57.
Rowan L. R. and Ahrens T. J. 1994. Observations of impact-induced molten metal-silicate partitioning. *Earth and Planetary Science Letters* 122:71–88.
Rubin A. E., Jerde E. A., Zong P., Wasson J. T., Westcott J. W., Mayeda T. K., and Clayton R. N. 1986. Properties of the Guin ungrouped iron meteorite: The origin of Guin and of group-IIE irons. *Earth and Planetary Science Letters* 76:209–226.
Rubin A. E. 2005. What heated the asteroids? *Scientific American* 292:82–90.
Rutherford M. J., Hess P. C., and Daniel G. H 1974. Experimental liquid line of descent and liquid immiscibility for basalt 70017. Proceedings, 5th Lunar Science Conference. pp. 569–583.
Ruzicka A., Fowler G. W., Snyder G. A., Prinz M., Papike J. J., and Taylor L. A. 1999. Petrogenesis of silicate inclusions in the Weekeroo Station IIE iron meteorite: Differentiation, remelting, and dynamic mixing. *Geochimica et Cosmochimica Acta* 63:2123–2143.
Ruzicka A., Killgore M., Mittlefehldt D. W., and Fries M. 2005. Portales Valley: Petrology of a metallic-melt meteorite breccia. *Meteoritics & Planetary Science* 40:261–296.
Ryerson F. J. and Hess P. C. 1978. The role of P_2O_5 in silicate melts. *Geochimica et Cosmochimica Acta* 44:611–624.
Shearer C. K., Papike J. J., and Spilde M. N. 2001. Trace-element partitioning between immiscible lunar melts: An example from naturally occurring lunar melt inclusions. *American Mineralogist* 86:238–246.
Schnetzler C. C. and Philpotts J. A. 1970. Partition coefficients of rare earth elements between igneous matrix material and rock-forming mineral phenocrysts. *Geochimica et Cosmochimica Acta* 34:331–340.
Schwandt C. and McKay G. 1998. Rare earth element partition coefficients from enstatite/melt synthesis experiments. *Geochimica et Cosmochimica Acta* 62:2845–2848.
Snyder G. A., Lee D.-C., Ruzicka A., Prinz M., Taylor L. A., and Halliday A. N. 2001. Hf-W, Sm-Nd, and Rb-Sr isotopic evidence of late impact fractionation and mixing of silicates on iron meteorite parent bodies. *Earth and Planetary Science Letters* 186:311–324.
Solomon M. 1963. Counting and sampling errors in modal analysis by point counter. *Journal of Petrology* 4:367–382.
Stöffler D., Bischoff A., Buchwald V. F., and Rubin A. E. 1988. Shock effects in meteorites. In *Meteorites and the early solar system,* edited by Kerridge J. F. and Matthews M. S. Tucson, Arizona: The University of Arizona Press. pp. 165–202.
Takahashi E. 1978. Partitioning of Ni^{2+}, Co^{2+}, Fe^{2+}, Mn^{2+} and Mg^{2+} between olivine and silicate melts: Compositional dependence of

partition coefficient. *Geochimica et Cosmochimica Acta* 42: 1829–1844.

Takeda H., Hsu W., and Huss G. R. 2003. Mineralogy of silicate inclusions of the Colomera IIE iron and crystallization of Cr diopside and alkali feldspar from a partial melt. *Geochimica et Cosmochimica Acta* 67:2269–2288.

Ulmer P. 1989. Partitioning of high field strength elements among olivine, pyroxenes, garnet and calc alkaline picrobasalt: Experimental results and an application. In *GERM—Geochemical earth reference model* (http://earthref.org/GERM), downloaded July 10, 2006.

Villemant B. 1988. Trace element evolution in the Plegrean Fields, Central Italy: Fractional crystallization and selective enrichment. *Contributions to Mineralogy and Petrology* 98: 169–183.

Villemant B., Jaffrezic H., Joran J.-L., and Treuil M. 1981. Distribution coefficients of major and trace elements: Fractional crystallization in the alkali basalt series of Cahine des Puys (Massif Central, France). *Geochimica et Cosmochimica Acta* 45: 1997–2016.

Visser W. and Koster van Groose A. F. 1979. Effects of P_2O_5 and TiO_2 on liquid-liquid equilibria in the system K_2O-FeO-Al_2O_3-SiO_2. *American Journal of Science* 279:970–988.,

Wasson J. T. 1985. *Meteorites: Their early record of solar-system history.* New York: W. H. Freeman and Company. 267 p.

Wasson J. T. and Kallemeyn G. W. 2002. The IAB iron-meteorite complex: A group, five subgroups, numerous grouplets, closely related, mainly formed by crystal segregation in rapidly cooling melts. *Geochimica et Cosmochimica Acta* 66:2445–2473.

Wasson J. T. and Wang J. 1986. A nonmagmatic origin of group-IIE iron meteorites. *Geochimica et Cosmochimica Acta* 50:725–732.

Watson E. B. 1976. Two-liquid partition coefficients: Experimental data and geochemical implications. *Contributions to Mineralogy and Petrology* 56:119–134.

Watson E. B. 1977. Partitioning of Mn between forsterite and silicate liquid. *Geochimica et Cosmochimica Acta* 41:1363–1374.

Watson E. B. and Green T. H. 1981. Apatite/liquid partition coefficients for the rare earth elements and strontium. *Earth and Planetary Science Letters* 56:405–421.

Weill D. F. and McKay G. A. 1975. The partitioning of Mg, Fe, Sr, Ce, Sm, Eu and Yb in lunar igneous systems and a possible origin of KREEP by equilibrium partial melting. Proceedings, 6th Lunar Science Conference. pp. 1143–1158.

Wheelock M. M., Keil K., Floss C., Taylor G. J., and Crozaz G. 1994. REE geochemistry of oldhamite-dominated clasts from the Norton County aubrite: Igneous origin of oldhamite. *Geochimica et Cosmochimica Acta* 58:449–458.

Wilson L. and Keil K. 1991. Consequences of explosive eruptions on small solar system bodies: The case of the missing basalts on the aubrite parent body. *Earth and Planetary Science Letters* 104: 505–512.

Yang J. and Goldstein J. I. 2005. The formation of the Widmanstätten structure in meteorites. *Meteoritics & Planetary Science* 40:239–253.

Zinner E. and Crozaz G. 1986a. A method for the quantitative measurement of rare earth elements by ion microprobe. *International Journal of Mass Spectrometry and Ion Processes* 69:17–38.

Zinner E. and Crozaz G. 1986b. Ion probe determination of the abundances of all the rare earth elements in single mineral grains. In *Secondary ion mass spectrometry, SIMS V,* edited by Benninghoven A., Colton R. J., Simons D. S., and Werner H. W. New York: Springer-Verlag. pp. 444–446.

Appendices

Petrology of silicate inclusions in the Sombrerete ungrouped iron meteorite: Implications for the origins of IIE-type silicate-bearing irons

Ruzicka, Hutson, and Floss (2006)

APPENDIX 1: Composition of various phases in Sombrerete determined by SIMS

APPENDIX 2: Normalized bulk compositions of inclusions and fine-grained P-rich segregations in Sombrerete

APPENDIX 3: Representative literature values for equilibrium mineral/melt partition coefficients based mainly on experiments involving basalt or andesite compositions

APPENDIX 4: Apparent mineral/melt partition coefficients based on mineral/glass concentration ratios in Sombrerete

Appendix 1a. Composition of glass and phosphate in Som-4, determined by SIMS. Values in parentheses represent uncertainties (based on counting statistics). n.d. = not determined.

	Na-glass (#4Nagls1)	Na-glass (#4Nagls2)	Na-glass (#4Nagls3)	Cl-apatite (#4phos1)	Cl-apatite (#4phos2)
Na wt%	4.72 (<0.01)	4.85 (<0.01)	4.11 (<0.01)	n.d.	n.d.
Mg µg/g	1640 (7)	3190 (7)	3480 (6)	n.d.	n.d.
Si wt%	33.4*	33.4*	33.4*	n.d.	n.d.
P µg/g	1570 (9)	1780 (7)	2520 (7)	n.d.	n.d.
K µg/g	4600 (8)	4280 (5)	5030 (5)	n.d.	n.d.
Ca wt%	1.99 (<0.01)	1.31 (<0.01)	1.36 (<0.01)	37.4*	37.4*
Sc µg/g	9.13 (0.26)	10.6 (0.2)	13.2 (0.2)	n.d.	n.d.
Ti µg/g	2870 (4)	3140 (3)	3190 (3)	n.d.	n.d.
V µg/g	7.50 (0.22)	7.08 (0.15)	9.31 (0.16)	n.d.	n.d.
Cr µg/g	54.1 (0.7)	44.4 (0.4)	46.0 (0.4)	n.d.	n.d.
Mn µg/g	198 (1)	311 (1)	270 (1)	n.d.	n.d.
Fe wt%	1.41 (<0.01)	1.09 (<0.01)	1.26 (<0.01)	n.d.	n.d.
Ni µg/g	328 (7)	99.6 (2.5)	97.6 (2.4)	n.d.	n.d.
Rb µg/g	20.1 (0.8)	22.6 (0.6)	23.5 (0.6)	n.d.	n.d.
Sr µg/g	73.9 (0.8)	46.9 (0.4)	77.7 (0.5)	n.d.	n.d.
Y µg/g	5.94 (0.21)	10.3 (0.2)	8.70 (0.16)	n.d.	n.d.
Zr µg/g	62.2 (1.0)	77.5 (0.8)	84.8 (0.8)	n.d.	n.d.
Nb µg/g	5.91 (0.31)	7.61 (0.18)	7.56 (0.24)	n.d.	n.d.
Ba µg/g	36.2 (0.8)	38.7 (0.6)	28.2 (0.5)	n.d.	n.d.
La µg/g	1.25 (0.09)	1.58 (0.06)	1.37 (0.07)	27.8 (0.9)	32.4 (0.8)
Ce µg/g	2.80 (0.16)	3.94 (0.14)	3.40 (0.12)	76.3 (1.7)	87.5 (1.5)
Pr µg/g	0.380 (0.030)	0.498 (0.026)	0.466 (0.026)	10.1 (0.4)	12.4 (0.5)
Nd µg/g	1.47 (0.08)	2.44 (0.06)	1.89 (0.06)	51.2 (1.4)	63.7 (1.4)
Sm µg/g	0.446 (0.042)	0.636 (0.044)	0.611 (0.028)	16.5 (0.9)	19.0 (0.9)
Eu µg/g	0.413 (0.045)	0.241 (0.026)	0.384 (0.024)	1.54 (0.10)	1.50 (0.10)
Gd µg/g	0.475 (0.084)	0.888 (0.063)	0.550 (0.068)	19.8 (1.4)	22.4 (1.4)
Tb µg/g	0.094 (0.016)	0.172 (0.013)	0.167 (0.013)	3.71 (0.33)	3.92 (0.29)
Dy µg/g	0.780 (0.046)	1.49 (0.05)	1.19 (0.04)	21.5 (0.8)	25.9 (0.9)
Ho µg/g	0.177 (0.018)	0.345 (0.019)	0.278 (0.015)	4.78 (0.30)	5.24 (0.30)
Er µg/g	0.617 (0.031)	1.06 (0.04)	0.871 (0.034)	9.77 (0.42)	13.2 (0.6)
Tm µg/g	0.081 (0.009)	0.136 (0.009)	0.146 (0.008)	1.29 (0.11)	1.68 (0.12)
Yb µg/g	0.565 (0.035)	0.947 (0.031)	0.731 (0.024)	7.38 (0.41)	9.13 (0.45)
Lu µg/g	0.089 (0.013)	0.179 (0.011)	0.161 (0.014)	0.941 (0.100)	1.12 (0.15)
Hf µg/g	1.78 (0.08)	2.11 (0.07)	2.29 (0.08)	n.d.	n.d.
Th µg/g	0.230 (0.021)	0.357 (0.024)	0.354 (0.019)	n.d.	n.d.
U µg/g	0.039 (0.010)	0.068 (0.009)	0.050 (0.008)	n.d.	n.d.

*Normalized to value obtained by electron microprobe.

Appendix 1b. Composition of glass, phosphate, orthopyroxene and plagioclase in Som-1, determined by SIMS. Values in parentheses represent uncertainties (based on counting statistics). b.d. = below detection; n.d. = not determined; incl = inclusion.

	Na-glass (#1Nagls2)	K-glass [1,2] (#1Kgls1)	K-glass [1] (#1Kgls2)	Cl-apatite (#1phos1)	Cl-apatite (#1phos2)
Na wt%	5.45 (<0.01)	1.65 (<0.01)	1.64 (<0.01)	n.d.	n.d.
Mg µg/g	940 (7)	9060 (30)	2150 (10)	n.d.	n.d.
Si wt%	33.3*	31.9*	32.0*	n.d.	n.d.
P µg/g	3770 (20)	6390 (30)	12040 (40)	n.d.	n.d.
K µg/g	1480 (5)	58500 (80)	68700 (90)	n.d.	n.d.
Ca wt%	1.36 (<0.01)	2.64 (0.02)	2.93 (0.02)	36.6*	37.5*
Sc µg/g	3.82 (0.31)	6.27 (0.41)	2.65 (0.39)	n.d.	n.d.
Ti µg/g	2750 (5)	2920 (7)	2730 (7)	n.d.	n.d.
V µg/g	4.75 (0.21)	5.94 (0.31)	2.58 (0.16)	n.d.	n.d.
Cr µg/g	52.4 (0.8)	123 (2)	36.7 (0.9)	n.d.	n.d.
Mn µg/g	162 (2)	637 (4)	439 (3)	n.d.	n.d.
Fe wt%	0.397 (0.006)	1.21 (0.01)	0.565 (0.001)	n.d.	n.d.
Ni µg/g	40.8 (4.3)	72.6 (7.7)	27.8 (4.7)	n.d.	n.d.
Rb µg/g	3.06 (0.20)	294 (4)	363 (5)	n.d.	n.d.
Sr µg/g	29.6 (0.6)	55.9 (1.1)	40.3 (0.9)	n.d.	n.d.
Y µg/g	5.78 (0.21)	7.91 (0.31)	13.1 (0.5)	n.d.	n.d.
Zr µg/g	95.0 (1.6)	106 (2)	107 (2)	n.d.	n.d.
Nb µg/g	8.75 (0.37)	10.6 (0.4)	7.33 (0.47)	n.d.	n.d.
Ba µg/g	18.1 (0.6)	310 (4)	394 (4)	n.d.	n.d.
La µg/g	0.97 (0.07)	1.61 (0.09)	2.27 (0.15)	31.8 (1.1)	30.4 (1.3)
Ce µg/g	2.86 (0.14)	4.17 (0.20)	5.63 (0.41)	92.0 (2.2)	90.9 (2.7)
Pr µg/g	0.406 (0.023)	0.518 (0.036)	0.994 (0.087)	12.0 (0.6)	12.6 (0.6)
Nd µg/g	1.81 (0.07)	2.52 (0.09)	4.76 (0.21)	61.3 (1.8)	64.5 (2.0)
Sm µg/g	0.724 (0.056)	0.605 (0.065)	1.18 (0.13)	23.0 (1.2)	23.7 (1.5)
Eu µg/g	0.144 (0.022)	0.511 (0.224)	0.339 (0.256)	2.69 (0.17)	2.53 (0.19)
Gd µg/g	0.519 (0.084)	0.896 (0.096)	1.54 (0.24)	23.1 (1.7)	27.8 (1.9)
Tb µg/g	0.145 (0.019)	0.176 (0.020)	0.265 (0.044)	4.74 (0.37)	5.05 (0.48)
Dy µg/g	0.999 (0.049)	1.32 (0.07)	2.51 (0.13)	31.2 (1.1)	26.6 (1.2)
Ho µg/g	0.230 (0.017)	0.313 (0.027)	0.576 (0.04)	5.75 (0.45)	5.32 (0.41)
Er µg/g	0.584 (0.038)	0.938 (0.057)	1.52 (0.08)	14.4 (0.7)	16.8 (0.8)
Tm µg/g	0.105 (0.012)	0.121 (0.019)	0.218 (0.026)	2.19 (0.20)	2.46 (0.20)
Yb µg/g	0.971 (0.045)	0.350 (0.038)	0.713 (0.064)	14.6 (0.6)	20.4 (0.92)
Lu µg/g	0.084 (0.015)	0.087 (0.018)	0.197 (0.028)	1.50 (0.21)	1.69 (0.21)
Hf µg/g	2.80 (0.14)	2.70 (0.17)	3.68 (0.19)	n.d.	n.d.
Th µg/g	0.308 (0.032)	0.276 (0.037)	0.342 (0.047)	n.d.	n.d.
U µg/g	0.089 (0.019)	0.035 (0.016)	0.118 (0.026)	n.d.	n.d.

*Normalized to value obtained by electron microprobe. [1]Inferred minor phosphate contamination (elevated values for P, Ca, Sr, and REE). [2]Inferred minor orthopyroxene contamination (elevated values for Mg, Sc, V, Cr, Mn and Ni).

(continued)

Appendix 1b, continued.

	opx incl. rim (#1opx1)	opx [3] incl. rim (#1opx2)	plag incl. rim (#1plag1)	plag (#1plag3)	plag incl. interior (#1plag4)
Na wt%	0.027 (<0.01)	1.06 (<0.01)	0.603 (0.001)	1.18 (<0.01)	1.26 (<0.01)
Mg µg/g	138700 (200)	108900 (100)	2820 (10)	75.5 (3.1)	284 (4)
Si wt%	24.0*	23.9*	20.5*	21.3*	21.3*
P µg/g	98.2 (2.9)	469 (6)	556 (4)	213 (7)	353 (7)
K µg/g	270 (2)	483 (3)	978 (2)	449 (4)	373 (3)
Ca wt%	0.806 (0.016)	1.12 (0.01)	11.72 (0.02)	10.15 (0.04)	10.54 (0.03)
Sc µg/g	61.0 (0.6)	51.7 (0.5)	4.73 (0.21)	3.59 (0.52)	3.45 (0.38)
Ti µg/g	3000 (10)	2290 (10)	168 (1)	157 (3)	161 (2)
V µg/g	72.3 (0.9)	57.2 (0.8)	1.65 (0.08)	1.51 (0.16)	1.48 (0.11)
Cr µg/g	1980 (10)	1710 (10)	19.0 (0.4)	24.6 (0.8)	4.56 (0.23)
Mn µg/g	9190 (17)	6490 (10)	186 (1)	116 (2)	106 (2)
Fe wt%	12.34 (0.03)	10.57 (0.03)	0.496 (0.004)	0.514 (0.012)	0.284 (0.007)
Ni µg/g	58.4 (2.9)	161 (5)	34.1 (3.3)	64.5 (5.1)	24.1 (4.1)
Rb µg/g	1.77 (0.13)	1.29 (0.29)	4.91 (1.32)	b.d.	b.d.
Sr µg/g	0.267 (0.014)	11.5 (0.2)	175 (1)	163 (3)	197 (2)
Y µg/g	4.37 (0.22)	3.52 (0.18)	1.01 (0.05)	0.715 (0.088)	1.20 (0.08)
Zr µg/g	6.66 (0.27)	9.93 (0.29)	1.74 (0.08)	1.06 (0.07)	0.177 (0.028)
Nb µg/g	0.068 (0.010)	0.579 (0.032)	0.132 (0.012)	0.0949 (0.019)	0.034 (0.009)
Ba µg/g	1.30 (0.05)	1.68 (0.07)	9.79 (0.34)	12.7 (0.7)	12.9 (0.6)
La µg/g	0.003 (0.003)	b.d.	1.05 (0.06)	1.82 (0.19)	1.58 (0.12)
Ce µg/g	0.019 (0.005)	b.d.	2.09 (0.12)	3.17 (0.33)	3.21 (0.22)
Pr µg/g	0.003 (0.002)	b.d.	0.258 (0.019)	0.384 (0.064)	0.399 (0.041)
Nd µg/g	0.031 (0.009)	b.d.	0.926 (0.047)	1.51 (0.14)	1.46 (0.10)
Sm µg/g	0.027 (0.012)	b.d.	0.248 (0.027)	0.202 (0.073)	0.315 (0.068)
Eu µg/g	b.d.	b.d.	1.34 (0.07)	1.89 (0.15)	1.59 (0.10)
Gd µg/g	0.114 (0.039)	0.140 (0.023)	0.240 (0.034)	0.431 (0.098)	0.225 (0.066)
Tb µg/g	0.037 (0.008)	0.033 (0.006)	0.026 (0.007)	0.028 (0.016)	0.047 (0.014)
Dy µg/g	0.559 (0.037)	0.493 (0.035)	0.169 (0.015)	0.183 (0.041)	0.251 (0.035)
Ho µg/g	0.182 (0.021)	0.156 (0.017)	0.035 (0.007)	0.032 (0.014)	0.036 (0.011)
Er µg/g	0.745 (0.038)	0.625 (0.041)	0.056 (0.010)	b.d.	0.091 (0.028)
Tm µg/g	0.160 (0.016)	0.123 (0.014)	b.d.	b.d.	0.009 (0.016)
Yb µg/g	1.23 (0.07)	1.09 (0.05)	0.067 (0.011)	0.096 (0.035)	b.d.
Lu µg/g	0.277 (0.050)	0.197 (0.018)	0.006 (0.004)	b.d.	b.d.
Hf µg/g	0.468 (0.047)	0.476 (0.046)	0.048 (0.010)	0.090 (0.039)	0.046 (0.022)
Th µg/g	0.003 (0.006)	0.013 (0.008)	0.007 (0.003)	0.014 (0.015)	0.006 (0.008)
U µg/g	b.d.	0.014 (0.009)	0.005 (0.003)	0.017 (0.017)	0.001 (0.001)

*Normalized to value obtained by electron microprobe. [3]Inferred minor Na-glass contamination (elevated values for Na, K, Sr, and Nb).

Appendix 1c. Composition of the small arc within Som-1 in different locations, determined by SIMS*. Values in parentheses represent uncertainties (based on counting statistics, or standard deviation for average value). b.d. = below detection.

	interior (#1int1)	inner border (#1ext1)	interior (#1int2)	inner border (#1ext2)	average
Na wt%	0.674 (0.002)	0.611 (0.002)	0.281 (0.001)	0.465 (0.002)	0.508 (0.151)
Mg wt%	7.14 (0.02)	6.20 (0.02)	8.22 (0.02)	6.43 (0.02)	7.00 (0.79)
Si wt%	17.5 (<0.1)	17.6 (<0.1)	16.7 (<0.1)	17.6 (<0.1)	17.4 (0.4)
P wt%	7.81 (0.02)	7.44 (0.02)	7.09 (0.02)	7.63 (0.02)	7.49 (0.27)
K µg/g	4980 (20)	8300 (30)	2710 (10)	4050 (20)	5010 (2060)
Ca wt%	17.8 (0.1)	17.5 (0.1)	18.1 (0.1)	18.7 (0.1)	18.0 (0.4)
Sc µg/g	35.5 (1.1)	42.8 (1.3)	49.0 (1.2)	38.4 (1.2)	41.4 (5.1)
Ti wt%	0.770 (0.002)	1.97 (0.01)	1.51 (<0.01)	1.02 (<0.01)	1.32 (0.46)
V µg/g	55.0 (1.2)	68.5 (1.5)	66.8 (1.5)	49.7 (1.3)	60.0 (7.9)
Cr µg/g	1180 (10)	1360 (10)	1510 (10)	1120 (10)	1290 (150)
Mn wt%	0.448 (0.002)	0.428 (0.002)	0.511 (0.002)	0.455 (0.002)	0.460 (0.031)
Fe wt%	11.2 (0.06)	9.48 (0.06)	9.48 (0.06)	7.56 (0.05)	9.44 (1.30)
Ni µg/g	989 (24)	588 (20)	608 (20)	411 (42)	649 (211)
Rb µg/g	23.3 (2.0)	45.3 (2.4)	12.6 (1.6)	18.6 (1.8)	25.0 (12.4)
Sr µg/g	135 (2)	147 (3)	152 (2)	147 (2)	145 (6)
Y µg/g	37.8 (1.0)	50.0 (1.4)	48.6 (1.3)	43.3 (1.3)	44.9 (4.8)
Zr µg/g	24.0 (1.0)	36.2 (1.5)	29.5 (1.4)	22.6 (1.2)	28.1 (5.3)
Nb µg/g	5.37 (0.35)	15.0 (0.9)	11.8 (0.6)	6.94 (0.45)	9.77 (3.84)
Ba µg/g	23.0 (1.3)	42.3 (1.9)	20.2 (1.3)	31.3 (1.7)	29.2 (8.6)
La µg/g	9.94 (0.59)	11.5 (0.7)	11.5 (0.8)	10.5 (0.8)	10.9 (0.7)
Ce µg/g	25.3 (1.3)	30.0 (1.4)	29.3 (1.5)	28.0 (1.5)	28.2 (1.8)
Pr µg/g	3.43 (0.28)	4.15 (0.33)	4.59 (0.37)	5.04 (0.39)	4.30 (0.60)
Nd µg/g	18.1 (0.8)	20.4 (0.8)	21.4 (0.9)	21.7 (0.9)	20.4 (1.4)
Sm µg/g	6.82 (0.57)	7.70 (0.63)	7.61 (0.64)	9.30 (0.68)	7.86 (0.90)
Eu µg/g	1.53 (0.12)	1.20 (0.13)	1.19 (0.12)	1.69 (0.14)	1.40 (0.22)
Gd µg/g	7.83 (0.85)	7.79 (0.93)	6.82 (0.86)	b.d.	7.48 (0.47)
Tb µg/g	1.10 (0.17)	b.d.	1.18 (0.15)	1.55 (0.17)	1.28 (0.20)
Dy µg/g	6.69 (0.41)	9.14 (0.50)	8.06 (0.47)	7.31 (0.46)	7.80 (0.91)
Ho µg/g	1.32 (0.14)	1.89 (0.17)	1.47 (0.16)	1.43 (0.17)	1.53 (0.22)
Er µg/g	4.03 (0.27)	4.75 (0.27)	4.12 (0.27)	3.69 (0.28)	4.14 (0.38)
Tm µg/g	0.487 (0.070)	b.d.	0.571 (0.079)	0.511 (0.078)	0.523 (0.035)
Yb µg/g	3.85 (0.29)	4.89 (0.37)	3.69 (0.29)	3.77 (0.30)	4.05 (0.49)
Lu µg/g	0.429 (0.062)	0.63 (0.11)	0.381 (0.088)	0.391 (0.099)	0.458 (0.102)
Hf µg/g	2.06 (0.19)	3.41 (0.25)	2.57 (0.19)	2.62 (0.19)	2.66 (0.48)
Th µg/g	0.587 (0.108)	0.653 (0.080)	0.809 (0.113)	0.745 (0.110)	0.699 (0.085)
U µg/g	0.266 (0.050)	0.270 (0.056)	0.134 (0.040)	0.291 (0.058)	0.240 (0.062)

*Normalized to 52.35 wt% Na + Mg + Si + P + K + Ca + Ti + Cr + Mn + Fe, the average bulk composition of the small arc determined by electron microprobe.

Appendix 1d. Composition of the large arc within Som-1 in different locations, determined by SIMS*. Values in parentheses represent uncertainties (based on counting statistics, or standard deviation for average value).

	interior (#1int3)	inner border (#1ext3)	interior (#1int4)	outer border (#1ext4)	interior (#1int5)	inner border (#1ext5)	average
Na wt%	0.244 (0.001)	0.283 (0.001)	0.275 (0.001)	0.299 (0.001)	0.239 (0.001)	0.216 (0.001)	0.259 (0.029)
Mg wt%	8.22 (0.01)	6.16 (0.02)	7.75 (0.01)	8.66 (0.02)	9.51 (0.02)	7.75 (0.01)	8.01 (1.02)
Si wt%	15.1 (<0.1)	15.1 (<0.1)	15.9 (<0.1)	17.1 (<0.1)	16.4 (<0.1)	14.8 (<0.1)	15.7 (0.8)
P wt%	6.82 (0.01)	7.48 (0.02)	6.14 (0.01)	5.06 (0.01)	6.69 (0.02)	6.86 (0.01)	6.51 (0.76)
K µg/g	2010 (10)	4530 (20)	2660 (10)	1110 (6)	1760 (8)	4380 (10)	2740 (1290)
Ca wt%	17.7 (0.1)	17.3 (0.1)	16.7 (0.1)	15.9 (0.1)	14.0 (0.1)	16.3 (0.1)	16.3 (1.2)
Sc µg/g	44.0 (0.7)	39.7 (1.3)	47.1 (0.6)	54.2 (1.0)	47.9 (1.1)	49.5 (0.7)	47.1 (4.5)
Ti wt%	0.399 (0.001)	1.90 (0.01)	1.62 (<0.01)	1.53 (<0.01)	1.73 (<0.01)	2.31 (<0.01)	1.58 (0.59)
V µg/g	55.4 (0.8)	48.7 (1.3)	64.0 (0.8)	78.1 (1.2)	71.5 (1.3)	70.4 (0.9)	64.7 (10.0)
Cr µg/g	1400 (5)	1130 (8)	1470 (4)	1830 (7)	1500 (7)	1590 (5)	1490 (210)
Mn wt%	0.490 (0.001)	0.396 (0.002)	0.496 (0.001)	0.518 (0.002)	0.447 (0.002)	0.529 (0.001)	0.479 (0.045)
Fe wt%	8.10 (0.03)	7.44 (0.05)	8.76 (0.03)	14.5 (0.1)	8.84 (0.05)	10.1 (<0.01)	9.62 (2.31)
Ni µg/g	859 (14)	439 (40)	571 (10)	1050 (20)	538 (16)	641 (12)	683 (208)
Rb µg/g	11.9 (1.1)	23.0 (1.7)	15.5 (1.0)	8.00 (0.98)	7.50 (0.70)	23.9 (1.3)	15.0 (6.6)
Sr µg/g	148 (1)	130 (2)	141 (1)	150 (2)	87.9 (1.5)	118 (1)	129 (21)
Y µg/g	65.3 (0.9)	47.5 (1.4)	50.5 (0.7)	29.2 (0.8)	35.2 (0.9)	47.9 (0.8)	45.9 (11.5)
Zr µg/g	16.5 (0.6)	32.6 (1.6)	19.4 (0.6)	20.8 (0.8)	21.5 (0.7)	28.3 (0.9)	23.2 (5.5)
Nb µg/g	2.06 (0.09)	13.4 (0.7)	9.64 (0.36)	7.38 (0.22)	9.20 (0.41)	16.5 (0.7)	9.70 (4.55)
Ba µg/g	16.6 (0.7)	22.5 (1.4)	18.3 (0.7)	13.8 (0.6)	8.81 (0.38)	20.9 (0.8)	16.8 (4.6)
La µg/g	11.9 (0.5)	11.2 (0.7)	12.0 (0.4)	7.59 (0.38)	7.12 (0.38)	11.0 (0.5)	10.1 (2.0)
Ce µg/g	32.4 (0.9)	28.9 (1.6)	30.2 (0.8)	19.3 (0.9)	19.7 (0.9)	29.5 (0.9)	26.7 (5.2)
Pr µg/g	4.46 (0.26)	4.68 (0.39)	4.29 (0.2)	2.42 (0.15)	3.20 (0.17)	4.86 (0.29)	3.99 (0.88)
Nd µg/g	21.5 (0.6)	19.7 (0.9)	20.0 (0.6)	11.7 (0.5)	13.7 (0.5)	21.1 (0.7)	17.9 (3.8)
Sm µg/g	6.68 (0.41)	7.14 (0.63)	5.29 (0.36)	3.06 (0.31)	4.09 (0.30)	6.69 (0.47)	5.49 (1.50)
Eu µg/g	1.16 (0.08)	1.49 (0.13)	0.965 (0.064)	0.861 (0.061)	0.776 (0.059)	0.978 (0.094)	1.04 (0.23)
Gd µg/g	8.10 (0.70)	7.19 (0.99)	9.08 (0.06)	4.16 (0.44)	5.01 (0.52)	8.04 (0.73)	6.93 (1.76)
Tb µg/g	1.29 (0.12)	1.35 (0.19)	1.33 (0.13)	0.624 (0.089)	0.842 (0.086)	1.27 (0.13)	1.12 (0.28)
Dy µg/g	8.87 (0.37)	7.84 (0.50)	8.04 (0.34)	4.10 (0.21)	5.22 (0.26)	7.84 (0.35)	6.98 (1.71)
Ho µg/g	1.63 (0.12)	1.45 (0.16)	1.60 (0.13)	0.795 (0.074)	0.936 (0.078)	1.60 (0.11)	1.34 (0.34)
Er µg/g	4.54 (0.21)	3.69 (0.30)	4.57 (0.19)	2.29 (0.12)	2.75 (0.14)	3.98 (0.25)	3.63 (0.86)
Tm µg/g	0.591 (0.055)	0.457 (0.083)	0.590 (0.048)	0.287 (0.027)	0.349 (0.036)	0.605 (0.052)	0.480 (0.126)
Yb µg/g	2.94 (0.20)	2.42 (0.23)	2.82 (0.18)	1.28 (0.13)	1.90 (0.13)	3.13 (0.21)	2.42 (0.65)
Lu µg/g	0.459 (0.071)	0.320 (0.088)	0.511 (0.067)	0.270 (0.056)	0.292 (0.052)	0.425 (0.060)	0.379 (0.090)
Hf µg/g	2.40 (0.17)	2.65 (0.30)	2.64 (0.14)	1.57 (0.13)	2.05 (0.14)	2.82 (0.18)	2.36 (0.43)
Th µg/g	0.906 (0.094)	0.732 (0.115)	0.795 (0.064)	0.491 (0.053)	0.403 (0.053)	0.789 (0.076)	0.686 (0.178)
U µg/g	0.246 (0.040)	0.212 (0.052)	0.211 (0.026)	0.140 (0.032)	0.191 (0.040)	0.186 (0.031)	0.198 (0.032)

*Normalized to 48.80 wt% Na + Mg + Si + P + K + Ca + Ti + Cr + Mn + Fe, the average bulk composition of the large arc determined by electron microprobe.

Appendix 1e. Composition of glass, orthopyroxene, and merrillite in Som-3, determined by SIMS. Values in parentheses represent uncertainties (based on counting statistics). n.d. = not determined; b.d. = below detection; incl. = inclusion.

	Na-glass [1] (#3Nagls1)	Na-glass (#3Nagls3)	orthopyroxene incl. rim (#3opx4)	merrillite incl. rim (#3phos1)
Na wt%	5.13 (0.01)	6.12 (0.01)	0.114 (<0.001)	n.d.
Mg wt%	1.18 (<0.01)	0.012 (<0.001)	12.9 (<0.1)	n.d.
Si wt%	34.3*	34.3*	24.1*	n.d.
P µg/g	4930 (30)	3580 (20)	672 (10)	n.d.
K µg/g	1400 (10)	1270 (10)	2150 (10)	n.d.
Ca wt%	1.36 (0.01)	0.985 (0.009)	0.706 (0.019)	33.6*
Sc µg/g	4.91 (0.43)	2.49 (0.36)	49.2 (0.7)	n.d.
Ti µg/g	2625 (7)	1730 (5)	2330 (10)	n.d.
V µg/g	11.5 (0.5)	5.30 (0.28)	55.2 (1.0)	n.d.
Cr µg/g	223 (2)	7.68 (0.38)	1520 (10)	n.d.
Mn µg/g	769 (5)	86.4 (1.4)	9880 (20)	n.d.
Fe wt%	1.41 (0.02)	0.253 (0.006)	14.8 (0.1)	n.d.
Ni µg/g	104 (6)	27.7 (3.4)	163 (8)	n.d.
Rb µg/g	4.95 (0.44)	5.85 (0.48)	16.5 (0.8)	n.d.
Sr µg/g	24.8 (0.7)	26.2 (0.7)	2.61 (0.10)	n.d.
Y µg/g	3.71 (0.21)	2.14 (0.13)	2.83 (0.16)	n.d.
Zr µg/g	87.9 (2.0)	44.6 (1.3)	8.31 (0.30)	n.d.
Nb µg/g	10.0 (0.4)	4.19 (0.22)	0.164 (0.019)	n.d.
Ba µg/g	6.64 (0.37)	5.02 (0.39)	4.15 (0.21)	n.d.
La µg/g	0.313 (0.042)	0.174 (0.023)	b.d.	88.6 (1.8)
Ce µg/g	1.13 (0.10)	0.577 (0.038)	0.030 (0.009)	217 (3)
Pr µg/g	0.185 (0.021)	0.103 (0.013)	0.010 (0.005)	29.9 (1.0)
Nd µg/g	0.716 (0.052)	0.428 (0.034)	0.121 (0.021)	131 (3)
Sm µg/g	0.111 (0.033)	0.032 (0.021)	0.078 (0.026)	39.2 (1.9)
Eu µg/g	0.097 (0.016)	0.093 (0.014)	0.012 (0.009)	6.16 (0.31)
Gd µg/g	0.394 (0.061)	0.339 (0.044)	0.084 (0.038)	32.7 (2.4)
Tb µg/g	0.046 (0.011)	0.040 (0.009)	0.021 (0.010)	6.82 (0.53)
Dy µg/g	0.506 (0.039)	0.384 (0.032)	0.308 (0.033)	44.6 (1.4)
Ho µg/g	0.119 (0.021)	0.067 (0.011)	0.101 (0.015)	9.30 (0.54)
Er µg/g	0.280 (0.030)	0.235 (0.024)	0.369 (0.035)	25.5 (0.9)
Tm µg/g	0.043 (0.010)	0.039 (0.009)	0.069 (0.012)	4.01 (0.29)
Yb µg/g	0.090 (0.024)	0.059 (0.017)	0.234 (0.032)	34.9 (1.2)
Lu µg/g	0.049 (0.014)	0.021 (0.009)	0.100 (0.020)	2.43 (0.29)
Hf µg/g	1.51 (0.12)	1.12 (0.11)	0.408 (0.056)	n.d.
Th µg/g	0.151 (0.030)	0.097 (0.026)	0.048 (0.018)	n.d.
U µg/g	0.049 (0.020)	0.040 (0.016)	0.075 (0.023)	n.d.

*Normalized to value determined by electron microprobe. [1]Inferred orthopyroxene contamination (elevated values for Mg, Sc, Cr, Mn, Fe, Ni) and minor phosphate contamination (elevated values for P, Ca).

Appendix 1f. Composition of glass and yagiite in Som-2, determined by SIMS. Values in parentheses represent uncertainties (based on counting statistics).

	Na-glass (#2Nagls1)	Na-glass [1] (#2Nagls2)	yagiite (#2yag2)	yagiite (#2yag3)
Na wt%	6.02 (0.01)	5.10 (<0.01)	1.40 (<0.01)	1.37 (<0.01)
Mg wt%	0.051 (0.001)	2.79 (<0.01)	3.65 (<0.01)	4.58 (<0.01)
Si wt%	33.7*	34.3*	27.9*	29.2*
P µg/g	2700 (20)	3870 (20)	3080 (10)	3170 (10)
K µg/g	156 (2)	181 (1)	11500 (10)	14000 (20)
Ca wt%	0.694 (0.007)	1.98 (0.02)	1.34 (0.01)	1.77 (0.02)
Sc µg/g	2.38 (0.32)	24.9 (0.4)	16.6 (0.3)	26.2 (0.3)
Ti µg/g	3020 (10)	10500 (10)	2400 (<10)	1750 (<10)
V µg/g	4.85 (0.25)	14.9 (0.3)	14.3 (0.3)	15.7 (0.3)
Cr µg/g	23.9 (0.6)	401 (2)	123 (1)	173 (1)
Mn µg/g	115 (1)	1640 (<10)	844 (3)	1160 (<10)
Fe wt%	0.412 (0.007)	5.99 (0.02)	1.75 (0.01)	2.02 (0.01)
Ni µg/g	79.7 (3.3)	2200 (20)	121 (2)	57.4 (1.9)
Rb µg/g	1.84 (0.20)	2.77 (0.29)	38.3 (1.0)	53.6 (1.2)
Sr µg/g	21.1 (0.5)	33.8 (0.5)	45.8 (0.6)	64.7 (0.7)
Y µg/g	4.92 (0.26)	11.8 (0.3)	11.3 (0.3)	10.3 (0.3)
Zr µg/g	66.2 (1.5)	73.3 (1.2)	41.0 (0.8)	39.9 (0.8)
Nb µg/g	14.5 (0.7)	29.9 (0.8)	3.98 (0.07)	27.9 (0.2)
Ba µg/g	0.829 (0.096)	2.06 (0.12)	93.6 (1.2)	118 (1)
La µg/g	1.22 (0.09)	2.64 (0.12)	2.73 (0.09)	2.44 (0.10)
Ce µg/g	3.08 (0.19)	7.61 (0.29)	7.82 (0.23)	6.81 (0.27)
Pr µg/g	0.469 (0.042)	1.08 (0.06)	1.09 (0.04)	1.03 (0.06)
Nd µg/g	1.96 (0.09)	4.85 (0.14)	5.00 (0.12)	3.95 (0.12)
Sm µg/g	0.592 (0.057)	1.22 (0.10)	1.52 (0.08)	1.26 (0.07)
Eu µg/g	0.079 (0.010)	0.233 (0.016)	0.247 (0.049)	0.303 (0.053)
Gd µg/g	0.559 (0.115)	1.79 (0.17)	1.62 (0.11)	1.43 (0.13)
Tb µg/g	0.107 (0.021)	0.294 (0.027)	0.289 (0.027)	0.289 (0.025)
Dy µg/g	0.824 (0.056)	1.93 (0.09)	1.98 (0.06)	1.65 (0.07)
Ho µg/g	0.163 (0.023)	0.368 (0.028)	0.422 (0.030)	0.374 (0.029)
Er µg/g	0.499 (0.040)	1.17 (0.06)	1.25 (0.04)	1.22 (0.05)
Tm µg/g	0.061 (0.013)	0.146 (0.012)	0.180 (0.011)	0.157 (0.014)
Yb µg/g	0.302 (0.031)	0.656 (0.046)	1.03 (0.042)	0.937 (0.041)
Lu µg/g	0.074 (0.017)	0.179 (0.023)	0.182 (0.018)	0.166 (0.015)
Hf µg/g	1.63 (0.10)	2.12 (0.10)	1.91 (0.08)	1.60 (0.08)
Th µg/g	0.190 (0.027)	0.268 (0.035)	0.223 (0.023)	0.257 (0.022)
U µg/g	0.079 (0.019)	0.092 (0.016)	0.033 (0.009)	0.056 (0.011)

*Normalized to value determined by electron microprobe. [1]Inferred orthopyroxene contamination (elevated values for Mg, Sc, Cr, Mn, Fe) and minor phosphate contamination (elevated values for P, Ca, Y, REE, Th, U).

Appendix 2a. Normalized bulk composition (wt%) of Sombrerete inclusions determined by modal reconstruction (MR) and defocussed beam analysis (DBA). Values in parentheses represent uncertainties estimated by propagating errors in modes and phase compositions (MR technique), or uncertainties estimated from the standard deviation of multiple analyses (DBA technique).

	Type	SiO_2	TiO_2	Al_2O_3	Cr_2O_3	FeO	MnO	MgO	CaO	Na_2O	K_2O	P_2O_5	Cl	technique
Som-1	3B	56.6	0.82	14.0	0.07	4.44	0.24	5.10	7.89	5.43	0.47	4.33	0.59	MR
		(2.2)	(0.10)	(0.7)	(0.02)	(0.44)	(0.02)	(0.41)	(0.68)	(0.24)	(0.07)	(0.59)	(0.08)	
Som-2	2	58.4	0.68	15.2	0.04	3.68	0.16	4.59	6.73	5.28	0.55	4.28	0.39	MR
		(6.9)	(0.22)	(1.7)	(0.01)	(0.67)	(0.03)	(0.70)	(0.78)	(0.59)	(0.12)	(0.29)	(0.04)	
Som-4	1	47.7	1.06	15.9	11.1	8.19	0.20	1.70	5.21	4.73	0.49	3.26	0.47	MR
		(2.1)	(0.30)	(0.8)	(1.0)	(0.86)	(0.03)	(0.22)	(0.31)	(0.37)	(0.15)	(0.11)	(0.04)	
Som-6	3A	55.1	0.97	13.5	0.40	4.73	0.17	5.24	8.89	4.92	0.43	4.97	0.72	MR
		(2.1)	(0.07)	(0.7)	(0.10)	(0.47)	(0.03)	(0.45)	(0.40)	(0.24)	(0.09)	(0.23)	(0.07)	
Som-8	3B	63.9	0.76	16.3	0.16	3.11	0.14	2.97	5.24	5.47	0.22	1.52	0.19	MR
		(1.6)	(0.03)	(0.4)	(0.01)	(0.18)	(0.01)	(0.13)	(0.37)	(0.56)	(0.04)	(0.35)	(0.05)	
Som-9	3A	62.4	1.14	14.1	0.21	5.39	0.20	4.51	5.48	4.28	0.24	1.83	0.26	MR
		(2.7)	(0.16)	(0.7)	(0.03)	(0.76)	(0.03)	(0.53)	(0.46)	(0.27)	(0.07)	(0.28)	(0.04)	
Som-10	2	55.0	0.54	13.3	0.12	4.45	0.13	4.21	9.29	4.86	0.32	6.89	0.85	MR
		(4.6)	(0.49)	(1.6)	(0.03)	(2.4)	(0.06)	(1.66)	(1.49)	(1.18)	(0.06)	(0.62)	(0.11)	
Som-11	3B	56.2	0.80	13.3	0.11	4.16	0.20	4.60	8.77	5.50	0.22	5.46	0.66	MR
		(1.7)	(0.11)	(0.5)	(0.03)	(0.40)	(0.02)	(0.31)	(0.67)	(0.23)	(0.03)	(0.52)	(0.09)	
Som-13	1	62.1	0.83	15.2	0.11	3.33	0.15	4.05	5.86	5.05	0.51	2.60	0.14	MR
		(2.3)	(0.07)	(0.6)	(0.03)	(0.25)	(0.02)	(0.39)	(0.20)	(0.20)	(0.03)	(0.14)	(0.02)	
Som-14	3B	56.5	0.53	15.4	0.11	4.47	0.22	5.40	8.21	5.25	0.17	3.31	0.45	MR
		(2.4)	(0.09)	(0.8)	(0.01)	(0.45)	(0.02)	(0.49)	(0.67)	(0.29)	(0.02)	(0.48)	(0.07)	

(continued.)

Appendix 2a, continued.

	Type	SiO_2	TiO_2	Al_2O_3	Cr_2O_3	FeO	MnO	MgO	CaO	Na_2O	K_2O	P_2O_5	Cl	technique
Som-15	1	65.3 (1.2)	0.84 (0.38)	16.2 (0.5)	0.11 (0.03)	2.71 (0.79)	0.15 (0.05)	2.23 (0.81)	5.06 (0.19)	5.33 (0.18)	0.51 (0.08)	1.38 (0.14)	0.16 (0.03)	DBA
Som-16	3A	59.5 (2.1)	0.92 (0.16)	15.1 (0.7)	0.11 (0.09)	4.01 (0.41)	0.19 (0.02)	4.43 (0.42)	7.42 (0.40)	4.97 (0.26)	0.14 (0.02)	2.82 (0.20)	0.43 (0.04)	MR
Som-17	1	56.4 (2.1)	0.43 (0.11)	13.9 (0.6)	0.06 (0.05)	0.78 (0.26)	0.03 (0.03)	0.27 (0.21)	12.6 (0.3)	5.71 (0.28)	0.50 (0.08)	8.15 (0.23)	1.20 (0.10)	MR
Som-18	1	51.7 (3.6)	0.67 (0.05)	17.5 (1.0)	3.83 (0.65)	6.55 (3.16)	0.12 (0.02)	1.19 (0.15)	7.44 (0.28)	5.56 (0.33)	0.54 (0.04)	4.34 (0.18)	0.64 (0.05)	MR
Som-19	3A	54.8 (2.9)	1.38 (0.18)	11.7 (0.8)	0.20 (0.03)	5.52 (0.56)	0.23 (0.04)	5.63 (0.62)	10.2 (0.5)	3.75 (0.26)	0.17 (0.03)	5.61 (0.36)	0.85 (0.08)	MR
Som-20	3A	56.3 (2.0)	0.62 (0.10)	13.4 (0.6)	0.31 (0.13)	4.52 (0.49)	0.17 (0.02)	4.90 (0.34)	9.09 (0.30)	4.78 (0.32)	0.35 (0.12)	4.89 (0.17)	0.73 (0.06)	MR
Som-21	2	60.5 (6.4)	0.50 (0.37)	16.3 (1.5)	0.07 (0.03)	7.84 (3.35)	0.22 (0.09)	5.56 (3.11)	2.36 (1.08)	3.96 (2.27)	1.00 (0.60)	1.48 (0.22)	0.26 (0.05)	DBA
Som-22	2	65.0 (2.6)	0.41 (0.29)	15.7 (0.9)	0.03 (0.02)	4.63 (1.84)	0.19 (0.06)	5.75 (2.09)	1.78 (0.28)	3.93 (1.61)	0.89 (0.33)	1.42 (0.26)	0.19 (0.03)	DBA
Som-24	3B	57.2 (2.3)	0.78 (0.11)	15.2 (0.7)	0.10 (0.07)	5.35 (0.50)	0.23 (0.02)	5.22 (0.45)	7.05 (0.66)	5.49 (0.26)	0.19 (0.03)	2.87 (0.50)	0.38 (0.07)	MR
mean (& std. dev.) all types		57.9 (4.4)	0.77 (0.24)	14.8 (1.4)	0.91 (2.53)	4.62 (1.66)	0.18 (0.05)	4.08 (1.58)	7.08 (2.54)	4.96 (0.58)	0.42 (0.23)	3.76 (1.89)	0.50 (0.28)	

Appendix 2b. Normalized bulk composition (wt%) of fine-grained P-rich segregations in type 3B Sombrerete inclusions determined by averaging multiple microprobe analyses. N = number of analyses. Values in parentheses represent the standard deviation.

	N	beam size (μm)	SiO_2	TiO_2	Al_2O_3	Cr_2O_3	FeO	MnO	MgO	CaO	Na_2O	K_2O	P_2O_5	Cl
Som-1 large arc	15	40	29.4 (5.6)	0.97 (0.50)	8.12 (3.56)	0.12 (0.04)	6.26 (1.09)	0.44 (0.08)	7.11 (1.52)	25.4 (3.4)	0.78 (0.45)	0.55 (0.42)	18.3 (3.7)	2.61 (0.57)
Som-1 small arc	12	40	29.0 (3.9)	1.67 (1.03)	6.07 (1.42)	0.11 (0.02)	7.43 (1.83)	0.39 (0.05)	6.42 (1.29)	25.0 (2.6)	1.55 (0.96)	0.26 (0.23)	19.3 (1.8)	2.75 (0.30)
Som-3 arc	8	40	17.5 (5.2)	1.30 (0.29)	2.85 (1.23)	0.11 (0.04)	4.90 (0.59)	0.45 (0.06)	4.84 (0.41)	35.4 (3.0)	0.51 (0.13)	0.50 (0.23)	27.5 (1.9)	4.12 (0.27)
Som-8 arc	14	4	17.5 (3.6)	1.07 (1.26)	4.83 (4.23)	0.16 (0.08)	4.78 (2.13)	0.35 (0.10)	3.72 (2.45)	36.8 (3.1)	0.49 (0.18)	0.07 (0.13)	26.3 (2.2)	4.02 (0.40)
Som-11 large arc core	22	20	17.2 (1.6)	0.59 (0.84)	5.41 (3.54)	0.21 (0.05)	5.12 (1.41)	0.27 (0.07)	7.86 (2.09)	31.6 (1.4)	1.40 (0.17)	0.09 (0.12)	29.1 (1.0)	1.18 (0.40)
Som-11 large arc rim	32	20	16.7 (1.2)	0.76 (0.91)	2.21 (0.48)	0.20 (0.04)	5.24 (1.04)	0.37 (0.04)	7.28 (1.65)	33.2 (1.5)	0.61 (0.33)	0.28 (0.26)	29.3 (1.1)	3.93 (1.02)
Som-11 large arc*	54	20	16.9 (1.6)	0.71 (0.68)	3.20 (1.22)	0.20 (0.04)	5.20 (0.92)	0.34 (0.04)	7.45 (1.44)	32.7 (2.6)	0.86 (0.25)	0.22 (0.18)	29.2 (2.4)	3.08 (0.72)
Som-11 small arc	12	20	17.2 (1.0)	0.51 (0.48)	2.24 (1.04)	0.23 (0.04)	5.73 (0.70)	0.50 (0.04)	7.57 (0.66)	35.7 (0.9)	0.40 (0.06)	0.16 (0.15)	25.7 (0.5)	4.12 (0.27)
Som-11 bubble	12	20	20.2 (2.2)	2.84 (2.74)	4.27 (3.00)	0.15 (0.05)	4.91 (1.87)	0.37 (0.07)	3.33 (1.83)	34.0 (1.9)	0.85 (0.50)	0.28 (0.19)	24.7 (2.1)	4.04 (0.37)
Som-14 large arc	4	40	25.1 (0.8)	1.04 (0.14)	6.33 (1.87)	0.26 (0.01)	7.80 (1.48)	0.45 (0.04)	7.47 (0.79)	27.4 (1.5)	1.21 (0.21)	0.07 (0.02)	19.9 (1.5)	2.95 (0.17)
Som-24 long arc	15	4	22.4 (10.6)	0.13 (0.07)	3.57 (4.00)	0.13 (0.05)	7.51 (3.97)	0.48 (1.00)	9.10 (4.64)	30.8 (11.5)	0.38 (0.22)	0.11 (0.13)	22.5 (8.3)	2.89 (1.35)

* Determined from arc core and rim compositions based on corresponding areas of each determined from Cl x-ray map.

Appendix 3. Representative literature values for equilibrium mineral/melt partition coefficients based mainly on experiments involving basalt or andesite compositions.

	olivine	orthopyroxene	plagioclase	apatite	merrillite	spinel
Sc	0.21	1.2	0.011	0.3	–	0.048
Ti	0.024	0.081	0.042	–	–	3.6*
V	0.22	0.9	0.05	–	–	300*
Cr	0.95	2.9	0.04	–	–	320§
Mn	0.91	0.88	0.04	0.13	–	24*
Ni	9.6	3.3	0.12	–	–	5.5
Zn	1.4	3.5	0.14	0.67	–	0.71*
Ga	0.1	0.32	1.6	0.25	–	4.6
Rb	0.02	0.024	0.047	0.4	–	–
Sr	3.8E-4	0.0058	2.05	1.25	1.0	–
Y	0.0061	0.068	0.022	6.4¶	14.4	0.01¶
Zr	0.004	0.026	0.0033	0.76	–	0.02
Nb	0.0011	0.0097	0.019	–	–	0.02
Ba	1.7E-5	0.0099	0.41	0.19	–	–
La	1.4E-5	0.0024	0.102	3.9	21.5	0.01
Ce	8.3E-5	0.0059	0.088	5	22.7	0.01
Pr	1.7E-4	0.0094	0.075	6.1	23.6	0.01
Nd	2.5E-4	0.012	0.061	7.2	24.5	0.01
Sm	4.2E-4	0.020	0.034	9.4	24.9	0.01
Eu	3.2E-4	0.0069	1.2	1.9	3.2	0.01
Gd	9.7E-4	0.040	0.030	8.3	22.1	0.01
Tb	0.0041	0.062	0.028	7.7	19.6	0.01
Dy	0.0071	0.085	0.026	7.1	17.4	0.01
Ho	0.010	0.11	0.024	6.4	14.8	0.01
Er	0.013	0.13	0.023	5.7	12.6	0.01
Tm	0.016	0.15	0.021	4.9	9.9	0.01
Yb	0.020	0.17	0.019	4.2	7.8	0.01
Lu	0.025	0.196	0.017	3.5	6.2	0.01
Hf	0.0073	0.029	0.013	0.37	–	0.02
Th	1.3E-4	0.005	0.009	3	1.3	–
U	1.9E-5	0.0035	0.010	2.2	0.48	–

*Based on apparent $D^{chromite/glass}$ for Som-4. §Median of range between literature values (~130-190) and apparent $D^{chromite/glass}$ for Som-4 (530). ¶Assumed same as for Ho. References: Bacon & Druitt (1988); Beatty (1993, 1994); Benjamin et al. (1983); Bindemann et al. (1988); Bougalt & Hekinian (1974); Colson et al. (1988); Dostal et al. (1983); Drake & Weill (1975); Duke (1976); Dunn (1987); Dunn & Sen (1994); Ewart & Griffin (1994); Ewart et al. (1973); Frey (1969); Fujimaki & Tatsumoto (1984); Fujimaki (1986); Gaetani & Grove (1997); Green et al. (1971); Green (1994); Irving (1978); Irving & Frey (1984); Jolliff et al. (1993); Jones & Layne (1997); Keleman & Dunn (1992); Kennedy et al. (1993); Klock & Palme (1988); Luhr & Carmichael (1980); Mahood & Stimac (1990); McKay & Weill (1976, 1977); Nielsen et al. (1992); Paster et al. (1974); Schnetzler & Philpotts (1970); Schwandt & McKay (1998); Takahashi (1978); Ulmer (1989); Villemant (1988); Villemant et al. (1981); Watson (1977); Watson & Green (1981); Weill & McKay (1975).

Appendix 4. Apparent mineral/melt partition coefficients based on mineral/glass concentration ratios in Sombrerete. Opx = orthopyroxene, plag = plagioclase.

	opx Som-1* $D^{1opx1/gls}$	opx Som-3 $D^{opx/gls}$	plag Som-1* $D^{plag/gls}$	apatite Som-1* $D^{apat/gls}$	apatite Som-1* $D^{1phos2/gls}$	apatite Som-4 $D^{apat/gls}$	apatite 1&4 avg. $D^{apat/gls}$	merrillite Som-3 $D^{merr/gls}$	yagiite Som-2 $D^{2yag2/2Nagls1}$
Sc	16	20	1.0	–	–	–	–	–	7.0
Ti	1.1	1.3	0.058	–	–	–	–	–	0.79
V	16	10	0.33	–	–	–	–	–	2.9
Cr	38	200	0.31	2.6	2.6	2.8	2.7	–	5.1
Mn	52	110	0.77	0.10	0.10	0.07	0.08	–	7.3
Ni	1.5	6.0	1.0	–	–	–	–	–	1.5
Zn	1.6	2.4	0.08	–	–	–	–	–	1.0
Ga	0.45	0.62	1.0	–	–	–	–	–	4.5
Rb	0.089	2.8	0.25	–	–	–	–	–	21
Sr	0.0089	0.10	5.9	–	–	–	–	–	2.2
Y	0.71	1.3	0.16	25[§]	24[§]	17[§]	21[§]	122[§]	2.3
Zr	0.070	0.19	0.010	–	–	–	–	–	0.62
Nb	0.008	0.039	0.010	–	–	–	–	–	0.27
Ba	0.037	0.83	0.33	–	–	–	–	–	110
La	0.003	–	1.4	30	29	22	26	510	2.2
Ce	0.006	0.05	0.94	31	30	24	27	380	2.5
Pr	0.007	0.10	0.80	28	29	25	27	290	2.3
Nd	0.016	0.28	0.66	32	33	30	31	310	2.6
Sm	0.036	2.5	0.34	31	32	31	31	1200	2.6
Eu	–	0.13	10	17	17	4.4	11	66	3.1
Gd	0.20	0.25	0.53	45	49	33	39	96	2.9
Tb	0.24	0.52	0.22	32	33	26	29	170	2.7
Dy	0.52	0.80	0.19	27	25	21	24	120	2.4
Ho	0.74	1.5	0.14	22	22	19	21	140	2.6
Er	1.2	1.6	0.12	25	27	14	19	110	2.5
Tm	1.5	1.8	0.08	21	22	12	17	100	2.9
Yb	1.3	4.0	0.09	18	21	11	15	590	3.4
Lu	3.1	4.7	0.07	18	19	7.2	13	110	2.4
Hf	0.16	0.37	0.022	–	–	–	–	–	1.2
Th	0.01	0.50	0.03	9[†]	10[†]	7[†]	8[†]	--	1.2
U	–	1.9	0.08	9[†]	9[†]	14[†]	11[†]	--	0.42

*The bulk composition of glass in Som-1 was calculated by combining the composition of Na-glass (1Nagls2) and K-glass (1Kgls2) with the modal proportion of each glass found in the inclusion ($X_{Na\text{-}glass}$ = 0.571, $X_{K\text{-}glass}$ = 0.027). [§]Assumes that CI-normalized abundance in phosphate same as for Ho, based on ionic size considerations. [†]Assumes that CI-normalized abundances of Th and U in apatite same as Er and Ho, respectively, based on data for arcs in Som-1.